

ISSN 1451 - 9372 (Print)
ISSN 2217 - 7434 (Online)
JULY-SEPTEMBER 2025
Vol.31, Number 3, 173-248

Chemical Industry & Chemical Engineering Quarterly



The AChE Journal for Chemical Engineering,
Biochemical Engineering, Chemical Technology,
New Materials, Renewable Energy and Chemistry
www.ache.org.rs/ciceq



Journal of the
Association of Chemical Engineers of
Serbia, Belgrade, Serbia

**Chemical Industry &
Chemical Engineering
CI&CE Quarterly**

EDITOR-IN-CHIEF

Vlada B. Veljković

*Faculty of Technology, University of Niš, Leskovac, Serbia
E-mail: veljkovicvb@yahoo.com*

ASSOCIATE EDITORS

Srđan Pejanović

*Department of Chemical
Engineering, Faculty of Technology
and Metallurgy, University of
Belgrade, Belgrade, Serbia*

Dunja Sokolović

*Faculty of Technical Sciences,
University of Novi Sad, Serbia*

Ivona Radović

*Faculty of Technology and
Metallurgy, University of Belgrade,
Serbia*

EDITORIAL BOARD (Serbia)

Đorđe Janačković, Ivanka Popović, Viktor Nedović, Goran Nikolić, Sanja Podunavac-Kuzmanović, Siniša Dodić, Zoran Todorović, Olivera Stamenković, Marija Tasić, Jelena Avramović, Jasna Canadanovic-Brunet, Ivana Karabegović

ADVISORY BOARD (International)

Dragomir Bukur

*Texas A&M University,
College Station, TX,
USA*

Milorad Dudukovic

*Washington University,
St. Luis, MO, USA*

Jiri Hanika

*Institute of Chemical Process Fundamentals, Academy of Sciences
of the Czech Republic, Prague, Czech Republic*

Maria Jose Cocero

*University of Valladolid,
Valladolid, Spain*

Tajalli Keshavarz

*University of Westminster,
London, UK*

Zeljko Knez

*University of Maribor,
Maribor, Slovenia*

Igor Lacik

*Polymer Institute of the Slovak Academy of Sciences,
Bratislava, Slovakia*

Denis Poncelet

ENITIAA, Nantes, France

Ljubisa Radovic

*Pen State University,
PA, USA*

Peter Raspor

*University of Ljubljana,
Ljubljana, Slovenia*

Constantinos Vayenas

*University of Patras,
Patras, Greece*

Xenophon Vergyios

*University of Patras,
Patras, Greece*

Ronnie Willaert

*Vrije Universiteit,
Brussel, Belgium*

Gordana Vunjak Novakovic

*Columbia University,
New York, USA*

Dimitrios P. Tassios

*National Technical University of Athens,
Athens, Greece*

Hui Liu

China University of Geosciences, Wuhan, China

FORMER EDITOR (2005-2007)

Professor Dejan Skala

University of Belgrade, Faculty of Technology and Metallurgy, Belgrade, Serbia

FORMER ASSOCIATE EDITORS

Milan Jakšić, ICEHT/FORTH, University of Patras, Patras, Greece

Jonjaua Ranogajec, Faculty of Technology, University of Novi Sad, Novi Sad, Serbia



Journal of the
Association of Chemical Engineers of
Serbia, Belgrade, Serbia

**Chemical Industry &
Chemical Engineering
CI&CE Quarterly**

Vol. 31

Belgrade, July-September 2025

No. 3

Chemical Industry & Chemical Engineering
Quarterly (ISSN 1451-9372) is published
quarterly by the Association of Chemical
Engineers of Serbia, Kneza Miloša 9/1,
11000 Belgrade, Serbia

Editor:

Vlada B. Veljković
veljkovic@yahoo.com

Editorial Office:

Kneza Miloša 9/1, 11000 Belgrade, Serbia
Phone/Fax: +381 (0)11 3240 018
E-mail: shi@ache.org.rs
www.ache.org.rs

For publisher:

Ivana T. Drvenica

Secretary of the Editorial Office:

Slavica Desnica

Marketing and advertising:

AChE Marketing Office
Kneza Miloša 9/1, 11000 Belgrade, Serbia
Phone/Fax: +381 (0)11 3240 018

Publication of this Journal is supported by the
Ministry of Education, Science and
Technological Development of the Republic of
Serbia

Subscription and advertisements make payable
to the account of the Association of Chemical
Engineers of Serbia, Belgrade, No. 205-2172-
71, Komercijalna banka a.d., Beograd

Technical Editor:

Marija B. Tasić

Journal manager:

Aleksandar B. Dekanski

Printed by:

Faculty of Technology and Metallurgy,
Research and Development Centre of Printing
Technology, Karnegijeva 4, P.O. Box 3503,
11120 Belgrade, Serbia

Abstracting/Indexing:

Articles published in this Journal are indexed in
Thompson Reuters products: *Science Citation
Index - Expanded*TM - access via *Web of
Science*[®], part of *ISI Web of Knowledge*SM

CONTENTS

- Karthikeyan Subramanian, Sathiyagnanam Amudhavalli
Paramasivam, Damodharan Dillikannan, **Machine learning
predictions on the output parameters of common rail direct
injection engines fueled with ternary blend** 173
- Mahboubeh Asal, Abolfazl Davodiroknabadi, Mohammad Mirjalili,
Ali Nazari, **Influence of texture and nanomaterials on the
produced natural fiber characteristics** 185
- Masanori Yoshida, Toshiki Kosaka, Yoshiki Mukai, Koichi
Nakahara, Reno Kiyota, **Gas-liquid dispersion agitated by
closed turbine type impeller** 193
- Marko Pavlović, Marina Dojčinović, Jasmina Nikolić, Anja Terzić,
Vladimir Pavićević, Saša Drmanić, Enita Kurtanović,
**Application of waste raw materials as a reinforcement for
protective coatings based on pyrophyllite** 199
- Nebojša Vasiljević, Vladan Mičić, Mitar Perušić, Marija Mitrović,
Duško Kostić, **Optimization of ultrasound-assisted extraction
of (poly)phenolic compounds from blueberry (*Vaccinium
myrtillus*) leaves** 207
- Piyanun Ruangurai, Nattabut Tanasansurapong, Sirakupt
Prasitsanha, Rewat Bunchan, Wiput Tuvayanond, Thana
Chotchuangchutchaval, Chaiyaporn Silawatchananai,
**Utilizing machine vision and artificial neural networks for
dried grape sorting during production** 219
- Junhee Han, Hyojung Kim, Dohyung Lee, **Suppressing pre-
hydrolysis in TiO₂ manufacturing: Design optimization of an
indirect heating hydrolysis system** 229
- Dario Balaban, Jelena Lubura, Predrag Kojić, **Integrated neural
network and Aspen plus model for entrained flow gasification
kinetics investigation** 239

**The activities of the Association of Chemical Engineers of Serbia
are supported by:**



**MINISTRY OF SCIENCE,
TECHNOLOGICAL DEVELOPMENT
AND INNOVATION
OF REPUBLIC OF SERBIA**



Faculty of Technology and
Metallurgy, University of Belgrade



Faculty of Science, University of Novi Sad



Institute for Technology of Nuclear
and Other Mineral Raw Materials,
Belgrade



Faculty of Technology,
University of Novi Sad



Institute of Chemistry, Technology and Metallurgy,
University of Belgrade



Faculty of Technical Sciences
University of Novi Sad



Faculty of Technology,
University of Niš, Leskovac



Faculty of Technical Sciences,
University of Priština, Kosovska Mitrovica



IMS Institute, Belgrade



DCP HEMIGAL
Leskovac



Elixir Prahovo

KARTHIKEYAN
SUBRAMANIAN¹
SATHIYAGNANAM
AMUDHAVALLI
PARAMASIVAM²
DAMODHARAN
DILLIKANNAN³

¹Department of Mechanical
Engineering, Annamalai
University, Chidambaram, Tamil
Nadu, India

²Department of Mechanical
Engineering, Govt. College of
Engineering (Deputed from
Annamalai University), Salem,
Tamil Nadu, India

³Department of Mechanical
Engineering, Jeppiaar
Engineering College, Chennai,
Tamil Nadu, India

SCIENTIFIC PAPER

UDC 662.756.3:621.4:519.7

MACHINE LEARNING PREDICTIONS ON THE OUTPUT PARAMETERS OF COMMON RAIL DIRECT INJECTION ENGINES FUELED WITH TERNARY BLEND

Article Highlights

- CRDI engine performance with a methyl acetate antioxidant/Non-edible oil/diesel ternary blend
- Examine the impacts of fuel injection strategies (FIT and EGR) on the engine characteristics
- Innovation of machine learning algorithms and prediction models LR, NN, K-NN, SVM, and LSTM.
- The LSTM model yields the highest R^2 value range of 0.92 to 0.96, for each engine response

Abstract

This study aims to employ a machine learning algorithm (MLA) to predict Common Rail Direct Injection (CRDI) engine emissions and performance using alternative feedstock. This study started with a diesel-SCOME- Methyl Acetate ternary mix. The engine was tested with fuel injection time (FIT) of 23°, 21°, and 19° bTDC with exhaust gas recirculation (EGR) levels of 10%, 15%, and 20% at estimated power productivity. Retard injection time and increasing EGR rates reduced in-cylinder peak pressure. Operating conditions with the maximum BTE were 21° bTDC and 10% EGR. Adjusting injection time and EGR reduced nitrogen oxide relative to the baseline. Smoke opacity was 1% lower at 21° bTDC and 10% exhaust gas recirculation than in conventional diesel operation. Retard injection time and exhaust gas recirculation increased HC and CO emissions. However, MLAs predict CI engine operation and discharge properties. The long short-term memory (LSTM) Model predicts engine output characteristics with a squared correlation (R^2) of 0.92 to 0.96. At the same time, mean relative error (MRE) values ranged from 1.74 to 4.68%. These results show that the LSTM models provide superior predictive capabilities in this investigation, particularly when considering numerous variables to analyze engine responses.

Keywords: biodiesel; methyl acetate; CRDI engine; EGR; Machine Learning Algorithms.

Fossil fuel-based energy use in industrialized and developing nations is predicted to grow by 5–7% and 1–2% yearly. In response to this increasing use,

researchers are considering alternative resources [1]. Because of their contributions to significant sectors, diesel engines are vital to the world market consequently [2]. Because they are more effective at transforming fuel than gasoline engines, compression ignition (CI) engines are often used in mobility. Nevertheless, because of their harmful impacts that affect the ecology and individual wellness, the greater levels of pollutants are a cause for worry. Prolonged exposure to pollutants has been found to elevate the likelihood of developing lung cancer, increasing the susceptibility to cardiorespiratory ailments [3]. It is feasible to use several types of oils to power CI engines

Correspondence: K. Subramanian, Department of Mechanical Engineering, Annamalai University, Chidambaram, Tamil Nadu, India.

E-mail: karthikeyanphd2022@gmail.com

Paper received: 30 March, 2024

Paper revised: 24 June, 2024

Paper accepted: 2 July, 2024

<https://doi.org/10.2298/CICEQ240303025S>

by using numerous methods and making adjustments [4]. The study reported that biomass fuel for industrial use is derived from agricultural byproducts. Thus, environmental impacts are mitigated. The effects of varying the ratio of alcohols added to milk scum oil are analyzed [5].

Overview of *Simmondsia chinensis* feedstocks

It is reported that the *Simmondsia chinensis* oil (SCO) extract from the seeds of the Jojoba tree plant, a shrub can reach a height of between 1 and 5 m and has a long, healthy life span (100–200 years). This plant, which is common in the United States, has many other names. Its seedlings have oil and wax content ranging from 44 to 56 percent. The jojoba oil had a yellow hue, was without scent, and contained only trace amounts of triglyceride esters in addition to 97% monoesters of long-chain lipids. This chemical component is responsible for jojoba's self-stability and tolerance to elevated temperatures when compared to other non-edible oils [6]. When SCO is treated with the transesterification procedure, the result is biodiesel, which has improved properties than plain diesel, such as greater intrinsic oxygen content, improved cetane, and less sulfur [7].

Biodiesel as an alternative fuel in CI Engine

Researchers evaluated CI engine efficiency and conducted ignition experiments using biodiesel derived from palm oil. It was discovered that using warmed oil resulted in decreased hydrocarbon (HC) and carbon monoxide (CO) pollutants but greater exhaust temperatures and nitrogen oxide (NO_x) levels. Hydrous ethanol significantly reduces nitrogen oxide emissions, according to a critical analysis of numerous approaches to employing it in engines [8]. Results from the experiments demonstrated a drastic cut in various discharges compared to the diesel engine running on a single injection. In addition, growth in brake thermal efficiency (BTE) was 4.46%. Propane-inducing diesel engines using waste seed biodiesel (WSBD) have been investigated [9]. Additionally, this revolutionary combustion method is being heavily tested in internal combustion engines. Minimizing pollutants and increasing burning effectiveness are the objectives [10]. Another study examined the effects of using sapota methyl ester on the parameters of combustion and EGR and their impact. The outcomes suggested that shorter delays occurred at higher CR values. Lowered levels of nitrogen oxides were also detected [11]. The trial was conducted using cottonseed biodiesel in a common rail direct injection (CRDI) engine using exhaust gas recirculation. It follows from these experimental probes that an EGR rate of 25% results in a nearly 33% reduction in No_x [12]. Recently,

the binary combination concept was investigated as a result of superior blend stability, reduced expenditure, along minor changes in engine hardware settings. The research outlined in this paper attempts to use gasoline along with methyl acetate. The studies on methyl acetate additives in engine applications are very limited. They have achieved prominence because of their soot minimization capability [13]. This study looks at what happens when diesel and n-Pentanol/Karanja oil biodiesel are mixed. By including n-Pentanol, the properties of the biodiesel-diesel blend will be better at low temperatures. Pentanol's reduced fluidity and great instability will also significantly lower pollutants [14]. They discovered that a higher concentration of additives significantly decreased brake-specific fuel consumption (BSFC) and contributed to a steeper percentage decline in emissions [15].

Studies on variable FIT and EGRs with Ternary fuel

The experiment was carried out with a ternary combination of diesel and JME+ n-butanol additive. It can be shown that jojoba oil with a high fraction of DBJ15 has the potential to achieve reduced pollutants in the short term while maintaining a high thermal efficiency [16]. Alcohol is made from a vast range of environmentally friendly ingredients. Alcohols, which include methanol, ethanol, and propanol, have a lower number of carbon atoms. Higher alcohols, on the other hand, have more carbon atoms than lower alcohols. These include pentanol, hexanol, heptanol, and decanol [17]. Researchers investigated the effects of combining diesel with 1-hexanol at different injection times and EGR percentages. Integrating 1-hexanol with an improved pre-combined burning phase prolonged the ignition impediment's length. At 23 BTDC and 10% EGR, there was a systematic reduction in both NO_x and smoke [18]. The usage of EGR technology is one common strategy for decreasing exhaust-borne nitrogen oxides in IC engines [19]. Increase the ratio of 1-C₆H₁₄O in diesel/WPO blends. Based on the data, it was found that an increased 1-C₆H₁₄O fraction in the mixture somewhat reduced engine performance. Smoke, CO, and NO_x were reduced at the same duration, although there was a small increase in hydrocarbons [20]. Investigators conducted an empirical analysis of 2 greater alcohols, decanol and 1-hexanol, combined with various blends of diesel and biodiesel. In this case, the tertiary mixes were almost identical to pure diesel and had superior BTE than biodiesel. Because of the greater alcohol content, the tertiary mix has the minimum emission characteristics, such as the least amount of smoke emission [21]. It stipulates that a CRDI diesel engine running on a ternary mix fuel has its burning and exhaust properties carefully examined during reduced passive

configurations. As a result, there is a decrease in smoke and Nox discharges. In addition to being very unpredictable, ethanol has an elevated level of O₂ and an elevated latent heat of evaporation. Any of these actions might aid in lowering smoke and NO_x pollutants [22]. Because ABE-diesel blends have a bigger O₂ level and latent heat of vaporization than plain diesel, the ABE-diesel operating attributes in a CO engine considerably reduce the production of soot particles and increase ultimate particle degradation. Additionally, a greater amount of air may be drawn into the spray from upstream due to the prolonged flame lift-off duration and ignition latency period [23].

Overview of machine learning prediction

In recent years, the field of machine learning has made a lot of progress, and techniques like artificial neural networks (ANN), support vector machine (SVM), random forest (RF), extreme gradient (XG) Boost, and deep neural networks (DNN) have emerged rapidly [24]. Integrating engine research with machine learning modeling methodologies can enhance the calibration of the engine and the identification of the effective zone and minimize the trials and 3D simulations [25]. Machine learning (ML) is one of the cutting-edge developments in the field of artificial intelligence (AI). Machine learning algorithms (MLAs) are plentiful; they all involve the same repetitive application of mathematical formulas [26]. MLAs are classified into four distinct categories, which are very significant [27]. In MLAs, the unsupervised learning technique is used to identify the hidden pattern of data when a training dataset is not available for investigation. The supervised learning method is used to anticipate data patterns when a designated training dataset is available. When some pieces of information are missing from the training dataset, supervised learning can be transformed into semi-supervised learning. When analyzing a data pattern and receiving input from an outside source, MLAs use the reinforcement learning technique [28]. The use of AI in bioenergy processes is extremely limited. In addition, there is a shortage of research that addresses the potential of machine learning techniques for making predictions and enhancing efficiency. Researchers have found that ML shows considerable promise for overcoming obstacles to expanding bioenergy production [29]. There is also a lack of data on the effectiveness of methyl acetate and biodiesel in CI engines. Therefore, this article uses ternary fuel to address these gaps in the literature. The ternary fuel has been compared on several important metrics. These performance parameters are predicted using cutting-edge ML methods.

Significance of the present work

Contrary to the existing literature, this study ventures into unexplored territory by examining the potential of methyl acetate additives as a viable substitute in CI engines. It goes beyond the limited studies on the impact of methyl acetate inclusion in diesel and *Simmondsia Chinensis* oil methyl ester (SCOME) combinations and explores the influence of EGR and injection time with variable projection using various ML systems. The objective is to employ these algorithms in analyzing the emission and performance attributes of a diesel engine operating on blends of methyl acetate-diesel fuel fortified with antioxidants. This research conducts a comprehensive analysis to evaluate the predictive performance of neural networks, k-NN, support vector machines, linear regression (LR), and Long Short-Term Memory (LSTM) methods in comparison to commonly employed techniques. The evaluation is based on the R^2 metrics. This paper proposes the utilization of a deep learning algorithm, namely an LSTM model, as a novel approach for predicting engine emissions and performance.

MATERIAL AND METHODS

Evaluation of test samples

Table 1 lists the key features of biofuel derived from *Simmondsiaceae* shrub seedlings, as well as the assessment variants. Because of the elevated fluidity and content of the SCO, its simple usage may result in injection problems. As a result, the transesterification process was modified in the conversion of SCO to reduce its consistency and concentration. Merck Millipore supplied C₃H₆O₂. A ternary mixture of C₃H₆O₂, diesel, and biodiesel was created. By combining diesel with biodiesel, binary variation was created. The diesel content in the two combinations was 70% and 50%, accordingly. The ternary blends were referred to as D50SCOME30MA20 (Diesel 50% + SCOME30% + Methyl Acetate 20% by volume) is the MA20 blend. D70SCOME30 (Diesel 70% + Biodiesel 30% by volume) is the binary combination.

Experimentation equipment and configuration

Figure 2 depicts the experimental configuration. The Kirloskar TV1 CI engine was used for evaluation, which was a mono-cylinder, 4S, VCR-CI engine coupled to a dynamometer. In compliance with Nira i7r rules, it was restructured with the requisite receptors, sensors, and an accessible ECU to provide electronic injection. An AVL DIGAS 444N tester was used for determining NO_x, while an AVL 437C smoke meter was used to detect smoke (SO). To achieve the injection

Table 1. Characteristics of test fuels.

Property	Standard	Diesel	SCOME	D70 SCOME30	D50 SCOME30 MA20
Density (kg/m ³)	ASTM	832	877	846	873
Kinematic viscosity @40°C (cst)	ASTM D 445	2.89	5.12	3.85	3.51
Flash Point (°C)	ASTM D 92	69	152	96.9	98.7
Cetane Index (CI)	ASTM D 976	47	51	-	-
Calorific Value (MJ/kg)	ASTM D 240	42.5	38.21	41.28	39.12

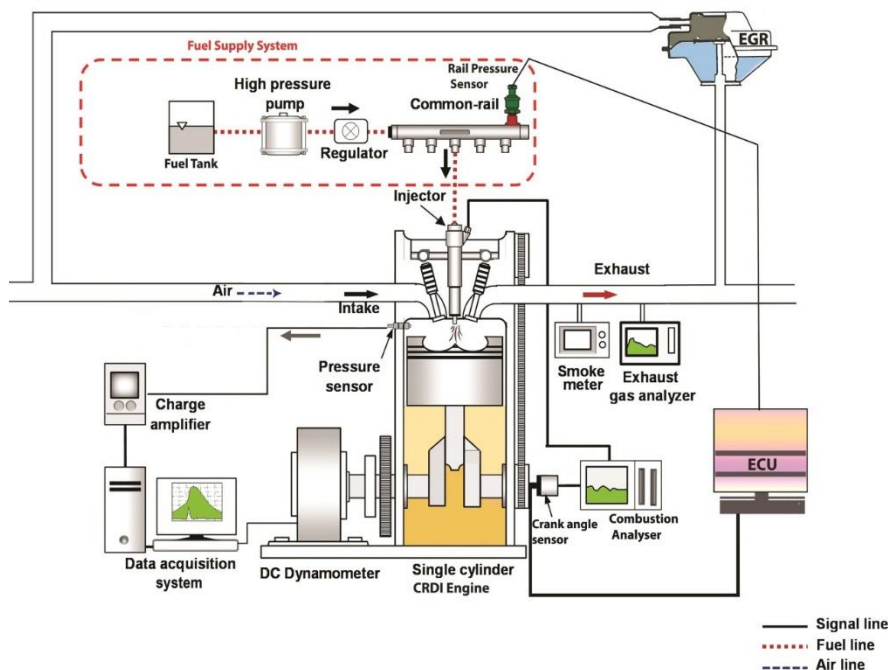


Figure 1. Schematic layout of experimental setup.

parameters needed for the assessment, a CRDI was required. The diesel delivery line was changed to link to the CRDI framework, and a high-pressure pumping was added to the fuel filtration. This serves as both a diesel holding reservoir and a pressure controller for the injection equipment. To regulate pressure, a rail pressure sensor is connected to the Nira i7r ECU. Although the original injector was unable to manage the much-increased injection pressures used by CRDI, a 6-hole solenoid-regulated nozzle was chosen to complete the job. The ECU was used to alter the first sensors and actuators to guarantee that every part worked properly. If the engine runs properly, it is termed diagnostically competent. Table 2 summarises the experiment engine settings.

Table 2. Technical specification.

Make and Model	Kirloskar, TV1
Cylinders & Stroke	1 & 4
Bore	87.5 mm
Stroke length	110 mm
Swept volume	661 cc
Speed	1500 rpm
Rated output	3.5 kW at 1500 rpm
CR	1:17.5
Cooling method	Water-cooled
IT, CA bTDC	23°
FIP	600 bar

EGR Setup

The EGR method is used to lower the in-cylinder and total temperatures of the charge, which in turn diminishes the emissions of NO_x. This also makes EGR denser, which means its overall volume increases. A portion of the outlet gas is routed via the exhaust gas recirculation cooler and then into the air inlet. As the H₂O in the exhaust gas recirculation cooler stays at the same temperature, it functions as a thermal replacer, taking in the heat from the outlet gases that are being held back. Here, the discharge was subjected to a temperature reduction of 36 °C. The EGR valve regulates the amount of air that is recycled through the engine. The orifice size determines the exhaust gas flow rate. The best way to start the operation was to send the recycled exhaust gas to the input port. Eq. (1) was used to calculate the amount of EGR rate.

$$EGR\% = \left[\frac{(CO_2)_{intake}}{(CO_2)_{exhaust}} \right] \times 100 \quad (1)$$

The AVL 444 N gas equipment, renowned for its precision, was implemented to determine the amount of CO₂ being released. This was achieved by adjusting the outlet discharge until the amount of incoming

carbon dioxide met a certain value, ensuring accurate measurements. [30].

Experimental procedure

The baseline emissions and performance characteristics from the perspective of replacing 50% of the diesel volume with biodiesel. Tests were conducted on a binary blend that contained 70% diesel and 30% biodiesel. Compared to baseline diesel, smoke emissions were greater, and performance was worse. Therefore, we employed a well-established additive-blending approach to reduce tailpipe smoke below diesel operation levels. The methyl acetate was chosen for this study because of its similar properties to diesel. The study aims to replace 50% of the volume of diesel with an alternative fuel. We kept the diesel volume constant, lowered the biodiesel by 20% vol., and balanced it with methyl acetate. The ternary mix included 50% diesel, 30% SCOME, and 20% methyl acetate. Compared to the binary option, the ternary mix operation improved combustion and reduced smoke emissions below diesel. But the ternary blend did more tests at full load, changing the fuel injection time (FIT) (23°bTDC, 21°bTDC, and 19°bTDC) and the exhaust gas recirculation (10%, 15%, and 20%) to find the best setting for lowering NO_x and smoke emissions, as well as producing better performance. The study used diesel, two binary, and one ternary blend at normal operating conditions of 23° bTDC without EGR. Based on the examination, the ternary blend (D50SCOME30MA20) gave the best performance among the other blends at a normal setting. It is nearly closer to baseline fuel. Consequently, we conducted enhancement tests on the ternary blend of D50SCOME30MA20 (MA20) at compression ratio (CR19), and injection pressure (IP 600 bar) remained constant. Conducted the three trials on the same day and in the same weather conditions to establish consistency.

Machine Learning (ML) algorithms

ML is a recurrently employed form of AI technique. Artificial intelligence (AI) is widely regarded as an appealing and widely embraced technology for its ability to effectively identify and address various application domains, owing to its exceptional capacity for achieving high levels of accuracy [27]. The system is designed to possess the capacity for autonomous observation and subsequent prediction of unknown reactions. Without a doubt, user attributes and the success of their training have a direct impact on the effectiveness of ML algorithms [29]. The current study delves into a comprehensive analysis of 4 distinct ML algorithms. The four machine learning models

discussed in this context are LR, neural networks (NN), SVM, and LSTM. All algorithms are executed with Rapidminer Studio Version 9.6. The grid investigation methodology is employed in this research to predict the model parameters. The algorithms employed in this study are utilized to forecast engine responses, namely BSEC and BTE, as well as NO_x, CO, HC, and smoke. During the training process, three specific inputs are utilized, namely engine test fuels, FIT, and EGR rates. The study utilized a dataset including nearly 288 data points. The dataset was partitioned randomly using the shuffled sample technique in the methods. The training phase of the algorithms utilized 80% of the available data points, while the remaining 20% was allocated for the testing phase.

ANALYSIS OF ENGINE OUTPUT PARAMETERS

Combustion investigation

In-cylinder pressure analysis

Figure 2 illustrates the in-cylinder pressure (ICP) discrepancies observed at various crank angle (CA) sites for the examined variations. Under the same circumstances, Diesel, D70SCOME30, D50SCOME50, and D50SCOME30MA20 were 69.96, 69.82, 69.29, and 69.80 bars. The extended ignition delay of the MA20 variation, where more fuel ignites impulsively, led to a higher ICP compared to the binary combination. At 23°, the PCPs for 10%, 15%, and 20% exhaust gas recirculation were 69.29, 68.99, and 67.55 bar. At FITs of 21° and 19°, the ICPs for exhaust gas recirculation levels of 10%, 15%, and 20% were 66.04 bar, 66.95 bar, 65.19 bar, 62.99 bar, 61.69 bar, and 60.46 bar. Retarding FIT from 23° to 19° at any exhaust gas recirculation rate results in a drop in the ICP. At 10% EGR, the ICP decreased by 9%. Delayed ignition reduces fuel burning due to the bTDC drop, resulting in less uniform volume ignition and a lower ICP [31]. The EGR levels are enhanced from 10% to 20%, and PCP is reduced further at any given injection timing. For instance, at FIT of 23°bTDC, the PCP dropped by 2.5%. This is because the discharge emissions increased the specific heat, leading to a decrease in PCP [17].

Heat release rate analysis (HRR)

Figure 2b reveals HRR disparities at different crank inclinations for the evaluation fuels. The HRR for Diesel, D70SCOME30, D50SCOME50, and D50SCOME30MA20 were 45.63 J/°, 43.08 J/°, 40.43 J/°, and 48.13 J/°, correspondingly. Here, the MA20 blend portrayed higher HRR, which is resultant of the collective effect of lengthier ignition duration and better-oxygenated circumstances that increase the flame speed in the course of combustion, resulting in elevated HRR values [32]. When Increasing EGR

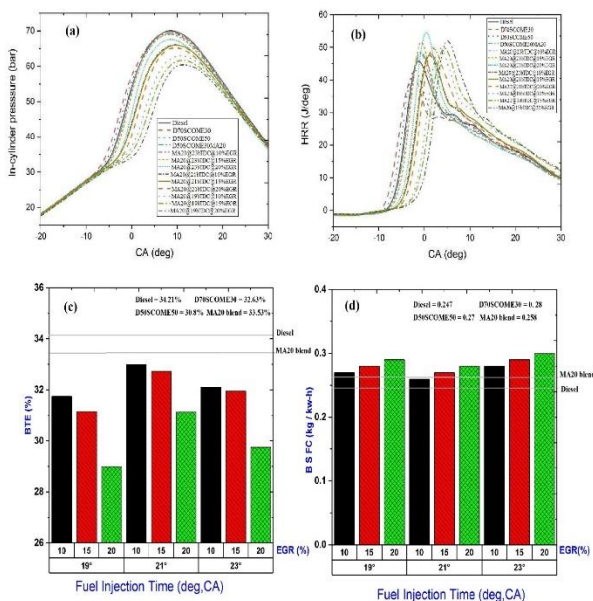


Figure 2. (a) ICP, (b) HRR, (c) BTE, and (d) BSFC for MA20 variant at various FIT and EGR rates.

levels and decreasing injection time cause the HRR graph to shift from left to right. EGR levels of 10%, 15%, and 20% at 23° have heat release rates of 48.51 J/°, 51.21 J/°, and 53.84 J/°. Similarly, for FIT values of 21° and 19°, HRRs are 47.56 J/°, 47.73 J/°, 49.93 J/°, 49.42 J/°, 49.45 J/°, and 52.07 J/° at EGR rates of 10%, 15%, and 20%. When changing the injection time from 23° to 21°, the HRR's peak point decreased. The HRR decreased from 48.51 to 47.56 J/° at 10% EGR. The decrease in injection time from 21° to 19° increased HRR. Due to a decrease in injection time, the FIT retards from 23° to 21°, reducing premixed combustion fuel usage. This reduces fuel consumption and increases heat release.[33]. A longer ignition delay due to retarded FIT increased the early mixed-period burning percentage and HRR excesses. HRR optimization occurred when EGR rose from 10% to 20%. HRR improves by 10% at 23°, but EGR rises from 0% to 20%. The EGR's impact prolongs ignition lag. The increase is due to the preliminary mixed-burning step using supplemental fuel. Similar findings were reported. [20].

Performance investigation

Brake thermal efficiency

Figure 2c shows the D50SCOME30MA20 blend's brake thermal efficiency at various FIT and exhaust gas recirculation settings. Diesel, D70SCOME30, D50SCOME50, and D50SCOME30MA20 had BTEs of 34.21%, 32.63%, 30.80%, and 33.53% at optimal output and engine standard specifications. The D50SCOME30MA20 mix had 2.3% greater BTE than the D50SCOME50 blend due to improved low heating value, atomization, and inborn O₂, which accelerated

combustion. Biodiesel ignites faster, especially during flame expansion, due to its higher thermal potential and oxygen content. [34]. The value of BTE is 32.12%, 31.96%, and 29.75% at 23° with EGR settings of 10%, 15%, and 20%. The BTE is 33%, 32.73%, 31.14%, 31.75%, 31.16%, and 28.99% at 21° and 19° FITs. According to Figure 2c, the tertiary mix delivered at 21° had the highest BTE, 2.5% more than that provided at 23° at the same EGR level. HRR studies support this. The ternary mix at 21° bTDC recovers more outputs and dissipates thermally faster, increasing BTE. Extended exhaust gas recirculation lowers the thermal efficiency of the ternary mix brake system. Because exhaust gases hinder combustion, BTE is lower [30].

Brake-specific fuel consumption

Brake-specific fuel consumption (BSFC) is a crucial measure of fuel efficiency for engines that generate rotational power. It quantifies how effectively the engine converts fuel into work, making it a key metric in our study. The BSFC measure's calorific value (CV), a significant biodiesel property, plays a vital role in this process. Reduced calorific values increase fuel consumption to provide the same power output; therefore, higher CVs reduce BSFC, indicating better fuel efficiency [35]. It's important to note that although BTE and BSFC have an adverse connection, diesel with a reduced BTE has a higher BSFC. As a consequence, the rationale for the changes in BTE among biodiesel, biodiesel-alcohol combinations, and diesel applies to BSFC as well. This reaffirms the scientific rigor and validity of our research. [21]. Figure 2d provides a practical perspective, showcasing the D50SCOME30MA20 variant's BSFC at different FIT and exhaust gas recirculation levels. Diesel, D70SCOME30, D50SCOME50 combination, and D50SCOME30MA20 mixture had BSFCs of 0.247, 0.28, 0.27, and 0.258 kg/kW-hr at stated capacity and engine standard characteristics. D50SCOME30MA20 has a lower BSFC than D50SCOME50. Due to its higher O₂ and CV, the ternary type uses less fuel to create similar energy. At 23° bTDC, the engine's BSFC was 0.28, 0.29, and 0.31 kg/kW-hr for 10%, 15%, and 20% EGR. At 10%, 15%, and 20% EGR, the engine's BSFC was 0.264, 0.272, 0.282, 0.273, 0.28, and 0.291 kg/kW-hr at FITs of 21° and 19°. Initially, the tertiary mixture BSFC dropped. We found that delaying the FIT from 23° to 21° and then to 19° increased it. Since the FIT was adjusted from 23° to 21°, this happened. This improvement allowed full burning by locating the combustion process at TDC. Thus, the engine needed less power to reach the speed. Lowering FIT from 21° to 19° caused heat dissipation lowered output and increased BSFC during the expansion stroke. For the ternary mix, higher EGR was

due to deterioration, which changed the air-fuel proportion and reduced burning, increasing BSFC. [19].

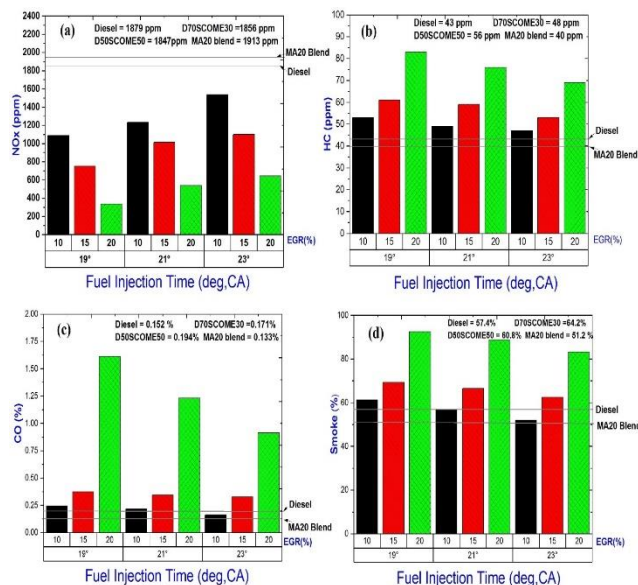


Figure 3. (a) NO_x, (b) HC (c) CO, and (d) Smoke for MA20 at different FIT and EGR levels.

Exhaust analysis

NO_x emission

Figure 3a shows nitrogen oxide differences for the D50SCOME30MA20 mix at different FIT and EGR levels. Diesel, D70SCOME30, D50SCOME50 mix, and D50SCOME30MA20 blend emitted 1859, 1856, 1847, and 1913 ppm of NO_x under specified power circumstances and engine stock settings. The ternary mix emitted more NO_x than the binary form because methyl acetate stimulates burning, raising gas temperatures and NO_x. Biodiesel burns more thoroughly due to its high oxygen content, raising peak temperatures and NO_x emissions [36]. Concerning EGR values of 10%, 15%, and 20%, at 23° bTDC, the NO_x emission was 1536, 1100, and 642 ppm, correspondingly. Similarly, at a FIT of 21° bTDC and 19° bTDC, the nitrogen oxide values were 1231 ppm, 1012 ppm, 540 ppm, 1088 ppm, 753 ppm, and 335 ppm, respectively, at EGR rates of 10%, 15%, and 20%. Delaying injection until 19° bTDC instead of 23° bTDC significantly reduced NO_x emissions. The exhaust gas recirculation rate was set at 10%, and the injection time was reduced from 23° to 21° bTDC, reducing NO_x emissions by 17%. Delaying the FIT reduced NO_x by 30%. The original analysis found that a ternary mix at 21° bTDC increased centralized burning. A shorter ID time and lower fuel consumption helped keep nitrogen oxides low [35]. The retardation of the explosive process by 21° to 19° bTDC displaced the combustion mechanism, changing the TDC point. This improvement allowed LTC mode adoption,

reducing nitrogen oxide emissions significantly [22]. The charge mixture's oxygen concentration disproportionately affected NO_x formation, which accelerated chemical processes and boosted combustible temperatures. The charge mixture's oxygen content affected NO_x production. Raising the EGR rate from 10% to 20% for a certain injection period reduced NO_x output by more than twice. The dilutive impact of increased thermally sensitive exhaust gases reduced exhaust temperatures [37]. In addition, the chemical reaction speed was impacted by the restricted supply of O₂.

Hydrocarbon

Figure 3b shows the D50SCOME30MA20 variant's HC at different FITs and EGRs. HC emissions at specified power output and engine settings for Diesel, D70SCOME30, D50SCOME50 mix, and D50SCOME30MA20 blend had HC emissions of 42, 48, 56, and 40 ppm, respectively. This shows that ternary variants reduce HC. In the diesel/SCOME combination, methyl acetate increased O₂ levels. This sped up the oxidation reaction even in areas with a lot of fuel, breaking down HCs that were not fully depleted and lowering HC emissions. At 23° bTDC, HC emission was 47, 53, and 69 ppm for 10%, 15%, and 20% EGR. In the same way, HC emission was 49 ppm at FITs of 21° bTDC and 19° bTDC, 59 ppm at 76° bTDC, and 53, 61, and 83 ppm at 10%, 15%, and 20% EGR rates. Increasing exhaust gas recirculation (EGR) to 10% and fuel injection time (FIT) from 23° to 19° bTDC increases hydrocarbon (HC) emissions by 11%. Because of the delayed injection, the membrane was more likely to get wet, and fuel was held in poor combustion zones. This produced unburned or partially burned HC [30]. Increasing EGR intensity from 10% to 20% resulted in increased HC emissions. This tendency to release HC is caused by exhaust gases lowering the gas temperature. This makes it difficult for hydrocarbons to split into carbon particles, releasing more HC [31].

Carbon monoxide

Figure 3c shows CO emission differences in the D50SCOME30MA20 blend at different FIT and EGR settings. Diesel, D70SCOME30, D50SCOME50 mix, and D50SCOME30MA20 blend had volume-based CO emissions of 0.152, 0.171, 0.194, and 0.133%. In the diesel/SSCOME blend, methyl acetate decreased CO emissions more than in the D50/SCOME50 blend. Methyl acetate aids CO-to-CO₂ conversion because it transports extra O₂ during combustion [38]. It's found that the CO emission at 23° bTDC was 0.161% vol., 0.326% vol., and 0.912% vol., respectively, when considering the EGR percentages of 10%, 15%, and 20%. Similarly, at FITs of 21° bTDC and 19° bTDC, the

CO was 0.217% vol., 0.343% vol., 1.231% vol., 0.244% vol., 0.374% vol., and 1.613% vol., respectively, at EGR rates of 10%, 15%, and 20%. With delayed FIT, CO levels increased but decreased with higher EGR rates. CO climbed 3.5% when the FIT was shortened from 23°bTDC to 19°bTDC at 10% EGR. Due to a shorter delay period, the A/F combination had less duration, potentially boosting CO emissions. However, increasing EGR frequency greatly lowered CO generation [39]. In a specific scenario of FIT 23°bTDC, increasing the EGR from 10% to 20% resulted in a 60% increase in CO. EGR's reduced air input may have generated an oxygen-deficient combustion zone, limiting CO oxidation. Lower gas temperatures reduced the OH-reactive concentration. However, increasing EGR frequency greatly lowered CO generation [40].

Smoke opacity

Figure 3d shows the D50SCOME30MA20 mix SO at different FITs and EGRs. Diesel, D70SCOME30, D50SCOME50 mix, and D50SCOME30MA20 blend had SO at specified power levels of 57.4%, 64.2%, 60.8%, and 51.2%, respectively. The ternary mix has far lower smoke opacity than the binary form. Alcohol has inherent O₂ molecules that provide O₂ for combustion, reducing smoke [34]. At 23° bTDC SO, EGR levels of 10%, 15%, and 20% were 52%, 62.5%, and 83.2%, respectively. For FITs of 21° and 19° bTDC, the smoke opacity was 56.9%, 66.5%, 88.7%, 61.2%, 69.2%, and 92.5% at EGR rates of 10%, 15%, 20%, respectively. The ternary variant's changes increased smoke production compared to the default. At 10% EGR, decreasing FIT by 23° to 19° bTDC increased SO by 15%. Due to reduced in-cylinder gas pressures during delayed intake latency, the A/F proportion changes. This increases smoke from carbon oxidation [5]. Even more than the FIT delay, rising EGR levels raised SO. Increasing EGR from 10% to 20% at 23° bTDC increased SO by 62.5%. Increased exhaust gas recirculation due to decreasing O₂ levels hinders combustion [36].

MLAs prediction analysis

In this study, the application of deep learning, namely the LSTM model, is utilized as the optimization framework. LSTM was used to predict BTE, BSFC, CO, HC, smoke, and NO_x using FIT and EGR variables. First, we train the LSTM model with 288 experimental observations. The network's performance was evaluated using a training dataset of 80% of the experimental data, a validation dataset of 10%, and a testing dataset of 10%. These may be assessed using training and testing of *MRE* and *R*²-values. After that, the stored network generates output values for the 25 randomly picked input values. Eq. (2) illustrates the

correlation coefficient (*R*²), while Eq. (3) illustrates the *MRE*. Where 'ti' is the target value and 'oi' is the theoretical output value,

$$R^2 = 1 - \left(\frac{\sum_{i=1}^n (t_i - \sigma_i)^2}{\sum_{i=1}^n (\sigma_i)^2} \right) \quad (2)$$

$$MRE = \frac{1}{n} \sum_{i=1}^n \left| 100 \cdot \frac{(t_i - \sigma_i)}{t_i} \right| \quad (3)$$

Let *t_i* and *o_i* represent the predicted and measured values, respectively. *t* denotes the mean of the measured values, while *n* represents the observations. This method contains knowledge of a particular model's anticipating power regarding a certain dataset. The coefficient of determination, denoted as *R*², has a range of values from 0 to 1. An *R*² number nearing 1 signifies a higher level of performance [41].

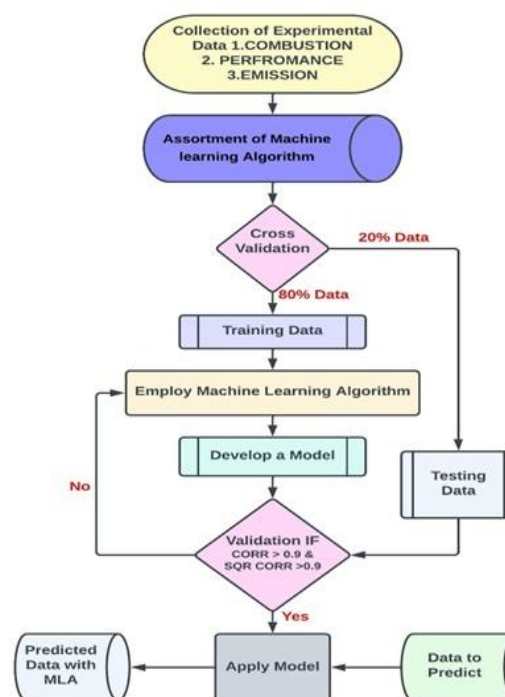


Figure 4. Machine learning algorithm models flow chart.

Evaluation of prediction models

*R*² levels are calculated by altering the quantities of training and evaluating information. The *R*² for various training and assessment information proportions demonstrates that the model is consistent beyond 80:20 ratios. The score approaching 100% indicates that the model can reflect all variance in output information. The hypothesized approach is contrasted to the *R*² values of models developed with

linear regression, support vector machine, neural networks, K -nearest neighbors (K-NN), and Deep Learning (LSTM) approaches. Figure 5a depicts model evaluations according to the R^2 value. The suggested model surpasses the previous approaches and yields excellent outcomes. The LR, NN, SVM, and LSTM models best fit the narrative or hypothesis of the current examination. At the same time, Figure 5a includes a broad comparison to provide a comprehensive overview of machine learning models. Four distinct ML models predicted values are close to unity. K-NN, PR, GP, and RVM models predicted values are very low compared to the unity. Therefore, this model is not suitable for the current investigation. The R^2 values were determined to be 0.92 and 0.96, respectively. The results of the LSTM replication demonstrate its capacity to anticipate crucial features accurately. The MRE values for the stated features range from 1.74% to 4.68%, Figure 5b shows that FIT, EGR, BTE, BSFC, and NOx strongly correlate with the target column. Even little changes in these variables affect the target column. CO, HC, and smoke are weaker but favorably connected to the target column. Thus, changes in these columns may not impact the target column. FIT, EGR, BTE, BSFC, and NOx predict the target column well, while CO, HC, and smoke do not. In future modeling and analysis, knowing how qualities relate to the target variable is vital.

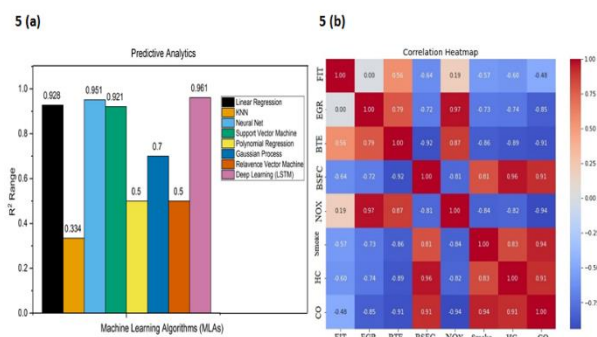


Figure 5. (a) Comparison of R^2 value and 5 (b) Heatmap representing correlation for Machine Learning Algorithms.

Validation of the LSTM model

The methodology's practicality must be validated before deployment. The Long Short-Term Memory (LSTM) model improved engine operating settings for experimental studies. The program generated expected significance levels from replications during failure periods. Figure 4 illustrates the training process through a flow chart, and Table 3 was used to verify these results. Eq. (4) calculates the value error percentage.

$$\text{Percentage of error (\%E)} = \frac{\text{Observed value} - \text{Predicted value}}{\text{Observed value}} \cdot 100 \quad (4)$$

The best results can only be obtained through appropriate verification. To account for LSTM fuel injection time (FIT) and EGR, the largest input variable maintained from testing was the mean. Equation error rates range from 0.2 to 5.7%. The analysis found fewer than 6% inaccuracies in emissions and efficiency projections. LSTM makes it easier to understand how elements interact. Thus, the Long Short-Term Memory (LSTM) model may predict diesel engine characteristics. Machine learning algorithms may predict pollutants and operational factors. Other quantitative and computational methods may struggle with the problem's complexity and diversity.

CONCLUSION

The research work outlines the methyl acetate, FIT, and EGR settings affect CI engine parameters in diesel and SCOME variations, as found below.

MA20 injected at 21°bTDC, and 10% EGR had the highest BTE (33%), correlating with the remaining operating conditions. However, the BTE was somewhat lower than that of the MA20 blend at default settings. In MA20 fuel, 21°bTDC and 10% exhaust gas recirculation reduce nitrogen oxides in comparison to other fuels. The MA20 mix decreases the SO by 11% at 21°bTDC and 10% exhaust gas recirculation. However, it was 1% less than baseline diesel. Later, FIT and higher EGR resulted in increased hydrocarbon and CO outflow. The LSTM methods estimate engine output characteristics that are close to unity. LSTM showed the highest R2 and MRE values, which are 0.961 and 1.74%, respectively. All measurements combined show that the other algorithms predict engine responses the least. When considering various injection timings and EGR rates with the MA20 mix, 21° bTDC and 10% EGR are generally the best operating conditions. The results suggest that a Simmondsia Chinensis seed biodiesel mix with MA20 volume can reduce pollutants in CRDI CI engine applications.

Choosing the best fuel injection time and EGR rate to reduce NOx and smoke emissions depends on many parameters, including engine type, fuel properties, and engine performance. According to the provided facts, decreasing emissions may begin with delayed fuel injection from 23° to 19° bTDC. In contrast, brake thermal efficiency, fuel consumption, and engine power output should be considered when selecting optimal operating conditions. Balancing emissions reduction and engine performance is essential. The delayed injection resulted in a decrease in NOx, which in turn led to a reduction in engine performance. Therefore, to evaluate emissions and performance, we

suggest conducting a series of tests or simulations under 21° bTDC at 10% EGR [42,43].

NOMENCLATURE

<i>ASTM</i>	American Society for Testing and Materials
<i>bTDC</i>	Before Top Dead Centre, CA
<i>BSFC</i>	Brake Specific Fuel Consumption (kg/kW-hr)
<i>BTE</i>	Brake Thermal Efficiency, %
<i>CA</i>	Crank Angle, deg
<i>CI</i>	Cetane Index
<i>CR</i>	Compression Ratio
<i>CRDI</i>	Common Rail Direct Injection
<i>CV</i>	Calorific value
<i>SCOME</i>	Simmondsia Chinensis Oil Methyl Ester
<i>MA</i>	Methyl Acetate
<i>D70SCOME30</i>	Diesel-70%, SCOME-30%
<i>D50SCOME50</i>	Diesel-50%, SCOME -50%
<i>D50SCOME30MA20</i>	Diesel-50%, SCOME - 30%, Methyl Acetate - 20%
<i>ECU</i>	Electronic Control Unit
<i>VCR</i>	Variable Compression Ratio
<i>HC</i>	Hydrocarbons, ppm
<i>CO</i>	Carbon monoxide, % vol.
<i>HRR</i>	Heat Release Rate, J/deg
<i>ICP</i>	In-cylinder pressure, bar
<i>NOx</i>	Nitrogen oxides, ppm
<i>PPM</i>	Parts Per Million
<i>MLAs</i>	Machine Learning Algorithms
<i>LSTM</i>	Long Short-Term Memory
<i>NO</i>	Neural Network
<i>LR</i>	Linear Regression
<i>SVM</i>	Support Vector Machine
<i>KNN</i>	K-Neural Network
<i>PR</i>	Polynomial Regression
<i>GP</i>	Gaussian Process
<i>RVM</i>	Relative Vector Machine
<i>R²</i>	Squared Correlation
<i>MORE</i>	Mean Relative Error
<i>RMSE</i>	Root Mean Square Error

REFERENCES

- [1] B. Ashok, K. Nanthagopal, B. Saravanan, K. Azad, D. Patel, B. Sudarshan, R.Aaditya Ramasamy, *Fuel* 235 (2019) 984–994. <https://doi.org/10.1016/j.fuel.2018.08.087>.
- [2] M.M. Khan, R.P. Sharma, A.K. Kadian, S.M.M. Hasnain, *Mater. Sci. Energy Technol.* 5 (2022) 81–98. <https://doi.org/10.1016/j.mset.2021.12.004>.
- [3] M. Jayapal, K.G. Radhakrishnan, *Energy Environ.* 33 (2022) 85–106. <https://doi.org/10.1177/0958305X20985618>.
- [4] D. Damodharan, A.P. Sathiyagnanam, B. Rajesh Kumar, K.C. Ganesh, *Environ. Sci. Pollut. Res.* 25 (2018) 13611–13625. <https://doi.org/10.1007/s11356-018-1558-5>.
- [5] M.V. De Pours, K. Gopal, A.P. Sathiyagnanam, B. Rajesh Kumar, D. Rana, S. Saravanan, D. Damodharan, *Energy Sources, Part A.* 42 (2020) 1772–1784. <https://doi.org/10.1080/15567036.2019.1604888>.
- [6] M. Arulprakasajothi, N. Beemkumar, J. Parthipan, N. Raju Battu, *Arab. J. Sci. Eng.* 45 (2020) 563–574. <https://doi.org/10.1007/s13369-019-04294-8>.
- [7] C. Ramakrishnan, P.K. Devan, R. Karthikeyan, *Environ. Prog. Sustain. Energy* 36 (2017) 248–258. <https://doi.org/10.1002/ep.12484>.
- [8] K. Viswanathan, A. Paulraj, *Energy Sources, Part A* 45 (2023) 3216–3230. <https://doi.org/10.1080/15567036.2020.1849451>.
- [9] A.I. EL-Seesy, Z. He, H. Hassan, D. Balasubramanian, *Fuel* 279 (2020) 118433. <https://doi.org/10.1016/j.fuel.2020.118433>.
- [10] J. Preuß, K. Munch, I. Denbratt, *Fuel* 216 (2018) 890–897. <https://doi.org/10.1016/j.fuel.2017.11.122>.
- [11] S. Raja. K.S, S.K. Srinivasan, K. Yoganandam, M. Ravi, *Energy Sources, Part A* (2021) 1–11. <https://doi.org/10.1080/15567036.2021.1877372>.
- [12] Y.S.M. Altarazi, A.R. Abu Talib, J. Yu, E. Gires, M.F. Abdul Ghafir, J. Lucas, T. Yusaf, *Energy* 238 (2022) 121910. <https://doi.org/10.1016/j.energy.2021.121910>.
- [13] R. Jayabal, S. Subramani, D. Dillikannan, Y. Devarajan, L. Thangavelu, M. Nedunchezhiyan, G. Kaliyaperumal, M.V. De Pours, *Energy* 250 (2022) 123709. <https://doi.org/10.1016/j.energy.2022.123709>.
- [14] M. Miya, K. Venkateswarlu, *Int. J. Ambient Energy* 43 (2022) 4870–4877. <https://doi.org/10.1080/01430750.2021.1923570>.
- [15] A. Cakmak, M. Kapusuz, O. Ganiyev, H. Ozcan, *Environ. Clim. Technol.* 22 (2018) 55–68. <https://intapi.sciendo.com/pdf/10.2478/rtuct-2018-0004>.
- [16] V. Praveena, U. Akshaykumar, T. Nishad, *J. Phys. Conf. Ser.* 2054 (2021) 012050. <https://iopscience.iop.org/article/10.1088/1742-6596/2054/1/012050>.
- [17] M.V. De Pours, A.P. Sathiyagnanam, D. Rana, B. Rajesh Kumar, S. Saravanan, *Appl. Therm. Eng.* 113 (2017) 1505–1513. <https://doi.org/10.1016/j.applthermaleng.2016.11.164>.
- [18] R. Shanmugam, D. Dillikannan, G. Kaliyaperumal, M.V. De Pours, R.K. Babu, *Energy Sources, Part A* 43 (2021) 3064–3081. <https://doi.org/10.1080/15567036.2020.1833112>.
- [19] D. Dillikannan, D. J., M.V. De Pours, G. Kaliyaperumal, A.P. Sathiyagnanam, R.K. Babu, N. Mukilarasan, *Energy Sources, Part A* 42 (2020) 1375–1390. <https://doi.org/10.1080/15567036.2019.1604853>.
- [20] B. Rajesh Kumar, S. Saravanan, *Fuel* 170 (2016) 49–59. <https://doi.org/10.1016/j.fuel.2015.12.029>.
- [21] J.C. Ge, G. Wu, B.-O. Yoo, N.J. Choi, *Energy* 253 (2022) 124150. <https://doi.org/10.1016/j.energy.2022.124150>.
- [22] X. Duan, Z. Xu, X. Sun, B. Deng, J. Liu, *Energy* 231 (2021) 121069. <https://doi.org/10.1016/j.energy.2021.121069>.
- [23] D. Kulandaivel, I.G. Rahamathullah, A.P. Sathiyagnanam, K. Gopal, D. Damodharan, D.P. Melvin Victor, *Fuel* 278 (2020) 118304. <https://doi.org/10.1016/j.fuel.2020.118304>.
- [24] Y. Yu, Y. Wang, J. Li, M. Fu, A.N. Shah, C. He, *IEEE Access* 9 (2021) 11002–11013. <https://doi.org/10.1109/ACCESS.2021.3050165>.
- [25] R. Yang, T. Xie, Z. Liu, *Energies* 15 (2022) 3242. <https://doi.org/10.3390/en15093242>.
- [26] Ü. Ağbulut, M. Ayyıldız, S. Sandemir, *Energy* 197 (2020) 117257. <https://doi.org/10.1016/j.energy.2020.117257>.
- [27] I. Portugal, P. Alencar, D. Cowan, *Expert Syst. Appl.* 97 (2018) 205–227. <https://doi.org/10.1016/j.eswa.2017.12.020>.
- [28] M. Aliramezani, C.R. Koch, M. Shahbakhti, *Prog. Energy*

- Combust. Sci. 88 (2022) 100967.
<https://doi.org/10.1016/j.pecs.2021.100967>.
- [29] W.R. Liao, J.H. Shi, G.X. Li, J. Appl. Fluid Mech. 16 (2023) 2041–2053.
<https://doi.org/10.47176/jafm.16.10.1801>.
- [30] M. Vijayaragavan, B. Subramanian, S. Sudhakar, L. Natrayan, Int. J. Hydrogen Energy 47 (2022) 37635–37647. <https://doi.org/10.1016/j.ijhydene.2021.11.201>.
- [31] B. Ashok, K. Nanthagopal, M. Senthil Kumar, A. Ramasamy, D. Patel, S. Balasubramanian, S. Balakrishnan, Int. J. Green Energy 16 (2019) 834–846. <https://doi.org/10.1080/15435075.2019.1641107>.
- [32] H. Xiao, X. Yang, R. Wang, S. Li, J. Ruan, H. J, Therm. Sci. 24 (2020) 215–229.
<https://doi.org/10.2298/TSCI190112304X>.
- [33] M. Chandran, R. Chinnappan, C. Kit Ang, Energy Sources, Part A (2020) 1–13.
<https://doi.org/10.1080/15567036.2020.1764671>.
- [34] G.R. Kothiwale, K.M. Akkoli, B.M. Doddamani, S.S. Kattimani, Ü. Ağbulut, A. Afzal, A.R. Kaladgi, Z. Said, Int. J. Environ. Sci. Technol. 20 (2023) 5013–5034.
<https://doi.org/10.1007/s13762-022-04397-0>.
- [35] K. Subramanian, S.A. Paramasivam, D. Dillikannan, M. Muthu, P.R. Yadav Sanjeevi, Int. J. Ambient Energy (2022) 1–14.
<https://doi.org/10.1080/01430750.2022.2103184>.
- [36] B. Rajesh Kumar, S. Saravanan, D. Rana, A. Nagendran, Energy Convers. Manage. 123 (2016) 470–486.
<https://doi.org/10.1016/j.enconman.2016.06.064>.
- [37] B. Ashok, K. Nanthagopal, R.T.K. Raj, J. P. Bhasker, D. Sakthi Vignesh, Fuel Process. Technol. 167 (2017) 18–30. <https://doi.org/10.1016/j.fuproc.2017.06.024>.
- [38] B.R. Kumar, S. Saravanan, Fuel 180 (2016) 396–406.
<https://doi.org/10.1016/j.fuel.2016.04.060>.
- [39] K. Duraisamy, R. Ismailgani, S.A. Paramasivam, G. Kaliyaperumal, D. Dillikannan, Energy Environ. 32 (2021) 481–505. <https://doi.org/10.1177/0958305X20942873>.
- [40] A. Ramesh, B. Ashok, K. Nanthagopal, M. Ramesh Pathy, A. Tambare, P. Mali, P. Phuke, S. Patil, R. Subbarao, Fuel 249 (2019) 472–485.
<https://doi.org/10.1016/j.fuel.2019.03.072>.
- [41] A.E. Gürel, Ü. Ağbulut, Y. Biçen, J. Cleaner Prod. 277 (2020) 122353.
<https://doi.org/10.1016/j.jclepro.2020.122353>.
- [42] M.V. De Pources, D. Dillikannan, G. Kaliyaperumal, S. Thanikodi, Ü. Ağbulut, A.T. Hoang, Z. Mahmoud, S. Shaik, C .A.Saleel, A.Afzal Process Saf. Environ. Prot. (2023), 738–752,
<https://doi.org/10.1016/j.psep.2023.02.054>.
- [43] D. Kulandaivel, I.G. Rahamathullah, A.P, Sathiyagnanam, K. Gopal , D. Damodharan, De Pources Melvin Victor, Fuel, 278, (2020), <https://doi.org/10.1016/j.fuel.2020.118304>.

KARTHIKEYAN
SUBRAMANIAN¹
SATHIYAGNANAM
AMUDHAVALLI
PARAMASIVAM²
DAMODHARAN
DILLIKANNAN³

¹Department of Mechanical
Engineering, Annamalai
University, Chidambaram, Tamil
Nadu, India

²Department of Mechanical
Engineering, Govt. College of
Engineering (Deputed from
Annamalai University), Salem,
Tamil Nadu, India

³Department of Mechanical
Engineering, Jeppiaar
Engineering College, Chennai,
Tamil Nadu, India

NAUČNI RAD

PREDVIĐANJA MAŠINSKOG UČENJA O IZLAZNIM PARAMETRIMA MOTORA SA COMMON RAIL DIREKTNIM UBRIZGAVANJEM GORIVA TERNARNE MEŠAVINE

Cilj ovog rada je da algoritmom mašinskog učenja (MLA) predvidi emisije CRDI (common rail direktno injektor) motora i performansi koristeći alternativnu sirovinu. Istraživanja su započeta trokomponentnom mešavinom dizel-SCOME-metil acetat. Motor je testiran sa vremenom ubrizgavanja goriva (FIT) od 23°, 21° i 19° bTDC sa nivoima recirkulacije izduvnih gasova (EGR) od 10%, 15% i 20% pri procenjenoj produktivnosti snage. Usporavanje vremena ubrizgavanja i povećanje EGR-a smanjuju vršni pritisak u cilindru. Radni uslovi sa maksimalnim BTE su bili 21° bTDC i 10% EGR. Podešavanje vremena ubrizgavanja i EGR smanjilo je azot oksid u odnosu na osnovnu liniju. Prozirnost dima bila je 1% niža na 21° bTDC i 10% recirkulacije izduvnih gasova nego u konvencionalnom dizel pogonu. Usporeno vreme ubrizgavanja i recirkulacija izduvnih gasova povećavaju emisije HC i CO. Međutim, MLA predviđa rad motora CI i svojstva pražnjenja. Model dugotrajne kratkoročne memorije (LSTM) predviđa izlazne karakteristike motora sa korelacijom na kvadrat (R^2) od 0,92 do 0,96. Istovremeno, vrednosti srednje relativne greške (MRE) kretale su se od 1,7 do 4,7%. Ovi rezultati pokazuju da LSTM modeli pružaju superiorne prediktivne mogućnosti, posebno kada se razmatraju brojne promenljive za analizu reakcija motora.

Ključne reči: gusta membrana; prozirna membrana; stepen apsorpcije; propustljivost biodizel; metil acetat; CRDI motor; EGR; algoritmi mašinskog učenja.

MAHBOUBEH ASAL¹
ABOLFAZL
DAVODIROKNABADI²
MOHAMMAD MIRJALILI¹
ALI NAZARI³

¹Department of Textile
Engineering, Yazd Branch,
Islamic Azad University, Yazd,
Iran

²Department of Design and
Clothing, Yazd Branch, Islamic
Azad University, Yazd, Iran

³Department of Art &
Architecture, Yazd Branch,
Islamic Azad University, Yazd,
Iran

SCIENTIFIC PAPER

UDC 677.1/3:620.3:66

INFLUENCE OF TEXTURE AND NANOMATERIALS ON THE PRODUCED NATURAL FIBER CHARACTERISTICS

Article Highlights

- Influence of nano strontium titanate and zinc titanate on composite properties
- Enhancing anti-inflammatory of composite by doping nanoparticles
- Innovation of machine learning algorithms and prediction models LR, NN, K-NN
- SVM, and LS Increasing bactericidal properties and durability by nanomaterials TM
- Enhancing strength and abrasion resistance of the composite

Abstract

This research investigated the type of texture and nano-materials and evaluated the effect of these two parameters on the final properties of the fabric. The 100% warp-weft cotton fabric and electrospun cellulosic nano fabric, which are treated with strontium titanate and zinc titanate, are produced using a specific method. Scanning electron microscopy and elemental mapping proved the existence of nanoparticles and helped to analyze the morphology of produced samples. The result of bactericidal property and its durability during washing cycles against Escherichia coli and Bacillus cereus (two common negative gram-negative/positive bacteria) was excellent. The strength and abrasion resistance of the treated specimens is higher than the untreated specimens due to the presence of nanoparticles and their special structural characteristics and the bond formation of these nanoparticles with fiber. On the other hand, the anti-inflammatory property of samples enhanced in comparison with raw samples due to the reduction of the production of inflammatory cytokines by nanomaterials.

Keywords: strontium titanate; zinc titanate; anti-inflammatory; electrospinning, texture.

In the ever-evolving world of textile manufacturing, researchers are constantly exploring innovative methods to enhance the strength and durability of fabrics. Two nanomaterials that have recently gained attention are strontium titanate and zinc titanate. These nanopowders have shown great potential in improving the strength and abrasion resistance of textiles and have remarkable properties such as bactericidal, self-cleaning, UV blocking, etc.

These properties are crucial in various industries where maintaining hygiene and preventing the spread of bacteria is of utmost importance [1–4].

Strontium titanate (SrTiO₃) and zinc titanate (ZnTiO₃) are both perovskite-type compounds that possess excellent electrical and mechanical properties. When incorporated into fabric finishes, these nanopowders can enhance the properties of textiles. The small size and high surface area of the nanoparticles allow for better penetration and adhesion to the fabric fibers, resulting in improved performance [5,6].

Strontium titanate is known for its high dielectric constant and piezoelectric properties. When applied as a fabric finish, it forms a thin, uniform layer on the fabric surface, which helps to strengthen the fabric structure. Additionally, strontium titanate nanoparticles can

Correspondence: A. Davodiroknabadi, Department of Design and Clothing, Yazd Branch, Islamic Azad University, Yazd, Iran.
E-mail: davodi@iauyazd.ac.ir
Paper received: 1 February, 2024
Paper revised: 1 June, 2024
Paper accepted: 2 July, 2024

<https://doi.org/10.2298/CICEQ240201026A>

impart anti-static properties to the fabric, reducing the accumulation of static charges and preventing discomfort or damage caused by electrostatic discharge [7].

Zinc titanate, on the other hand, possesses excellent photocatalytic properties and can absorb ultraviolet (UV) radiation. By incorporating zinc titanate nanopowders into fabric finishes, textiles can become more resistant to UV degradation, thus prolonging their lifespan. This makes them suitable for outdoor applications where exposure to sunlight is common [8].

A study published in the *Journal of Natural Fibers* [9] examined the impact of nano strontium titanate-treated cork web on UV-blocking and strength of cork webs. The results showed a significant increment in UV-blocking property and improvement in tensile strength. This was attributed to the enhanced adhesion between the web and the nanoparticles, which resulted in a more robust fabric structure.

Another study conducted by Zohoori *et al.* [10,11] investigated the effects of incorporating strontium titanate and titanium dioxide nanopowders into cotton fabrics. The researchers found that the treated fabrics exhibited higher self-cleaning properties.

In the field of oncology, research studies have explored the potential of fabric treated with zinc titanate nanoparticles in inhibiting the growth of cancer cells. A study published in the *International Journal of Nanomedicine* [12] examined the cytotoxicity of zinc titanate-treated fabric on cancer cell lines. The results demonstrated selective cytotoxicity, with cancer cells experiencing apoptosis while healthy cells remained unaffected. This targeted approach holds promise for the development of garments that provide comfort and potential therapeutic benefits for cancer patients.

Moreover, studies have been conducted to evaluate the durability of the zinc titanate treatment on fabric. The fabric samples were subjected to washing and rubbing tests to assess the longevity of the antimicrobial and cytotoxicity properties. The results indicated that the treatment remained effective even after multiple wash cycles and abrasion highlighting the practicality and durability of fabric treated with zinc titanate [13–15].

Further studies have explored the durability of the nanomaterial finishing on fabric. The fabric samples were subjected to washing, strength, and abrasion tests to evaluate the longevity of the anti-inflammatory properties. Results showed that the treatment remained effective even after multiple wash cycles, demonstrating the durability and practicality of incorporating nanoparticles into fabric treatments [16–19].

These research studies provide valuable insights into the potential of zinc titanate and strontium titanate as a fabric finish for enhancing the strength and abrasion resistance of textiles. By incorporating zinc titanate and strontium titanate nanopowders into fabric finishes, manufacturers can produce high-performance textiles that can withstand the rigors of everyday use. Producing nanofibers containing nano zinc titanate and strontium titanate has shown great potential in various applications such as catalysis, sensor technology, and energy storage. However, certain limitations need to be addressed for further advancements in this field. One major limitation is the difficulty in achieving a homogeneous distribution of the nano Zn/Ti particles within the nanofiber matrix. This can lead to variations in the properties and performance of the resulting nanofibers. Another limitation is the lack of understanding regarding the mechanism of nanoparticle incorporation and its effect on the overall structure and properties of the nanofiber. There are several potential applications for producing nanofibers that contain nano Zn/Sr. One possible application is in the field of medicine. These nanofibers could be used to develop advanced wound dressings that promote faster healing and reduce the risk of infection. Overall, the production of nanofibers containing nano Zn/Sr opens up possibilities for various applications in medicine and environmental protection.

MATERIAL AND METHODS

Materials and devices

Nano strontium titanate powder (CAS No.12060-59-2) with a molecular weight of 183.49 particle size of <100 nm and density of 4.81g/mL was prepared from Sigma Aldrich. Also zinc titanate nano powder with a molecular weight of 161.26 and particle size of <100nm was prepared from Sigma Aldrich too. The 100% bleached cotton fabric with a warp density of 22 yarn/cm, weft density of 18 yarn/cm, and fabric weight of 119.4 g/m² was prepared from Yazd-Baff Company. Bio-renewable succinic acid (CAS No.110-15-6) as a cross-link factor, Sodium hypophosphite, and Schweizer's reagent was prepared from Merck. Euronda ultra-sonic bath model Eurosonic 4D, 350 W, 50/60Hz (Italy) was used. The tensile strength was examined by a tabletop uniaxial testing apparatus (INSTRON 3345). A double-head rotary platform method was used to study the abrasion resistance through ASTM D-3884-09. The specimen's morphology was investigated by scanning electron microscopy (SEM-MIRA3-TESCAN), and the samples were covered by gold film.

Method

As shown in Table 1, two kinds of texture with different percentages of nanomaterials were used. In samples A and B, warp/weft fabric was finished one with nano strontium titanate and the other with nano zinc titanate. In samples C and D, the electrospinning fabric (nonwoven) was finished with these two nanomaterials. The finishing method of samples A and B was as follows: in the first step, the cotton fabric was washed with distilled water at 85 °C for 60 min. Then the washed fabric was floated in sodium hypophosphite/succinic acid as a catalyst/cross-link agent (respectively) for 60 min. The ratio of sodium hypophosphite/succinic acid was 4/6 (wt). In the next step, the fabric was dried at 80 °C for 4 min and immediately at 180 °C for 2 min. During the above steps, a beaker of nano strontium titanate and a beaker of nano zinc titanate suspension were prepared and sonicated for half an hour in an ultrasonic bath. Then the cured and dried fabric was immersed in these suspensions and sonicated for 30 min at 80 °C. Then the samples were kept in an oven for 3 min at 100 °C to fix nanoparticles and finally finished samples were washed in an ultrasonic bath for 10 min to remove unbonding nanoparticles. So, samples A and B were prepared by this method. The electrospinning method was used to produce samples C and D. In this method, 100% cellulose was dissolved in Schweizer's reagent ($[\text{Cu}(\text{NH}_3)_4(\text{H}_2\text{O})_2](\text{OH})_2$) and sonicated with 1.5% nanomaterials and loaded in a syringe on the electrospinning apparatus. The distance between the collector and nozzle was 15 cm, the drum speed was 135 rpm, the feeding rate was 0.5 mL/h, the voltage was 20 kV, and the traverse speed was 0.4 m/min. So, nonwoven fabric is prepared during this method.

Table 1. Specification of samples.

Sample Code	Texture Type	SrTiO ₃ (%)	ZnTiO ₃ (%)
A	Warp/Weft	1.5	0
B	Warp/Weft	0	1.5
C	Nonwoven	1.5	0
D	Nonwoven	0	1.5

The technique and condition of the bactericidal feature were done through the AATCC 100-2004 standard versus both *Bacillus cereus* (a gram-positive bacteria) and *Escherichia coli* (a gram-negative bacteria). The bactericidal feature was investigated through Eq. (1) as below, where *A* is the quantity of bacteria recovered from the inoculated treated test specimen incubated over a day while *B* is the quantity of bacteria recovered from the inoculated treated test specimen immediately after inoculation.

$$\text{The reduction of bacteria}(\%) = \frac{A-B}{A} \cdot 100 \quad (1)$$

To investigate the tensile property, the samples were cut into 5 cm × 3 cm sheets and loaded into the apparatus. The experiment was done at a rate of 5 mm/min.

Twenty-one male Wistar rats were chosen and protected in the same conditions for one day. All tests and experiments were done according to animal rights laws. Then the back skin of the rats was shaved and coated with produced samples (five rats for each sample and one for the control sample, whose back was coated with Indomethacin cream as reference sample) and tied firmly.

RESULTS AND DISCUSSION

Morphological analysis

Scanning electron microscopy images of samples is illustrated in Figure 1. Figure 1 (A–B) shows that the nanoparticles are distributed in fibers. Also, their elemental mapping analysis proves the existence of Zn and Sr particles and their good distribution on the surface of fibers (it must be mentioned that aggregation of nanoparticles causes their low effectiveness while their good distribution increases their effectiveness). Also, as shown in Figure (C–D), the nanofibers are formed through electrospinning, which contains nanoparticles. By close look, it demonstrates that the thickness of nanofibers is about 40 nm, which is very good. On the other hand, elemental mapping of these nanofibers proves the existence and good distribution without aggregation or agglomeration. (The elemental mapping of Sr particles is shown with green dots and the elemental mapping of Zn particles is shown with red dots).

Bactericidal properties and durability

Escherichia coli and *Bacillus cereus* are two common negative/positive bacteria, respectively. *Bacillus cereus* is a rod-shaped bacteria found in abundance in food and soil and can cause nausea, diarrhea, and vomiting syndrome [20]. On the other hand, the gram-negative bacteria *E.coli* can cause gastroenteritis, urinary tract infections, neonatal meningitis, hemorrhagic colitis, and Crohn's disease [21]. Nano ZnO is biocompatible for pharmaceutical textile usages [22]. Furthermore, nanoparticles of ZnO have unparalleled specifications such as photocatalytic properties and bacteriostatic effect [23]. As demonstrated in Figure 2, the bactericidal properties of all samples against *Escherichia coli* are higher than those of *Bacillus cereus*. This phenomenon is due to the various stoutness and thicknesses of the cell walls of bacteria. In contrast, the cell wall thickness of *Escherichia coli* is

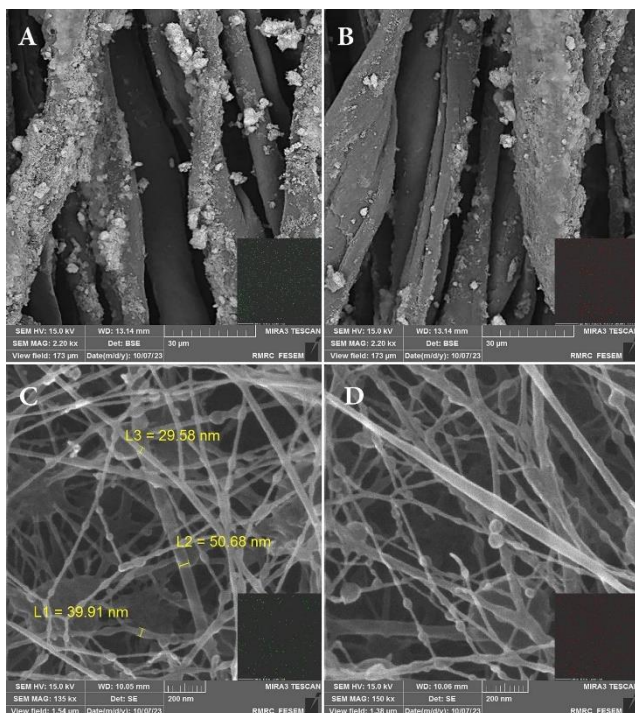


Figure 1. SEM of samples and elemental mapping of Sr and Zn.

lower than *Bacillus cereus* (10–20 nm and 20–40 nm, respectively). The bactericidal properties of strontium titanate and zinc titanate nanopowders can be attributed to their unique composition and structure. These powders are composed of tiny particles, typically less than 50 nanometers in size, which allows for more significant surface area contact with bacteria. When these nano powders come into contact with bacteria, their structure disrupts the cell walls of the microorganisms, preventing their growth and spread. Furthermore, these nano powders' high surface area-to-volume ratio enhances their bactericidal effectiveness. The increased surface area provides more opportunities for the nano powders to interact with bacteria, maximizing their antibacterial action. Additionally, the nano-sized particles can penetrate the bacteria more effectively, ensuring a higher degree of eradication. While the bactericidal properties of

strontium titanate and zinc titanate nanopowders are impressive, their durability is equally essential in ensuring long-term effectiveness. In applications where these nanopowders are subjected to repeated washing cycles, their antibacterial effect must remain intact. Durability in antimicrobial materials refers to their ability to withstand wear and tear, including exposure to harsh conditions such as washing, without compromising their antimicrobial properties. For strontium and zinc titanate nanopowders, durability is key in maintaining their bactericidal effectiveness over an extended period. As it was shown, bactericidal durability after 15 washing cycles was excellent and is more than 93% for both gram-negative/positive bacteria. The exceptional durability of strontium titanate and zinc titanate nanopowders can be attributed to their inherent properties and structural characteristics. These materials possess high chemical stability, allowing them to withstand exposure to various detergents, chemicals, and environmental factors without degradation. Additionally, their unique structure ensures that the antibacterial effect remains intact, even under challenging conditions. Comparing the bactericidal properties of samples demonstrates that warp/weft samples have a little higher antibacterial properties in comparison to nonwoven samples, but this is not significant and is negligible. On the other hand, the bactericidal property of samples that contain Sr is higher than the samples that have Zn. Strontium titanate and zinc titanate nanopowders share similar properties and demonstrate exceptional bactericidal effectiveness. However, strontium titanate nanopowder exhibits excellent photocatalytic properties, which can further enhance its bactericidal action. When exposed to light, strontium titanate nanopowder generates reactive oxygen species (ROS) that contribute to the destruction of bacteria. This photocatalytic property makes it particularly effective in environments with ample light exposure, such as hospitals or outdoor applications.

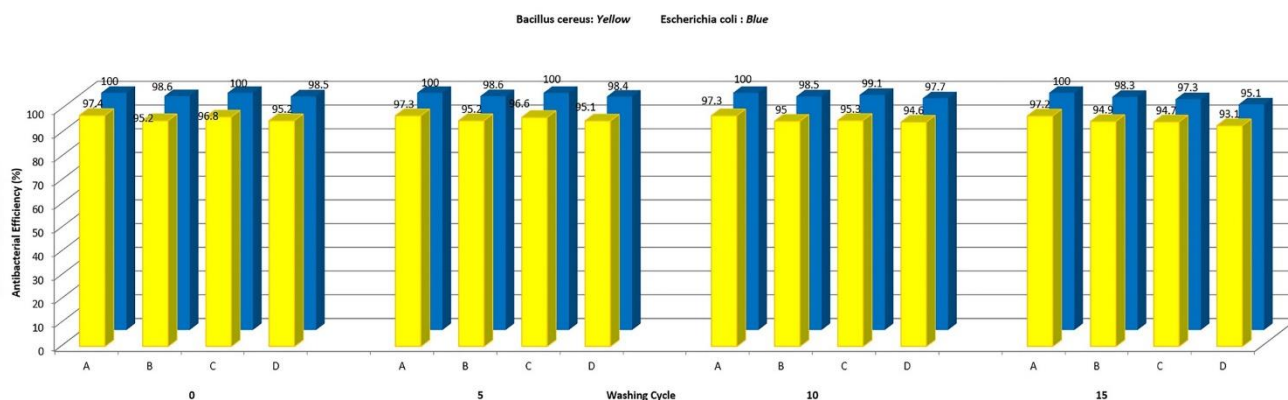


Figure 2. Bactericidal properties of samples and their washing durability.

Strength and abrasion properties

Fabrics are subjected to various stressors and forces during their lifespan, including stretching, bending, and abrasion. The strength and abrasion resistance of a fabric determine its durability and ability to withstand wear and tear. Traditionally, fabric finishes like coatings or treatments have been used to enhance these properties. However, the introduction of nanotechnology has opened up new possibilities for fabric finishing.

This comprehensive research study delves into the detailed analysis of the durability and strength of textile materials, with a specific focus on abrasion resistance and tensile strength of treated and untreated fabric samples. This section aims to discover how different conditions can enhance the performance of fabrics when subjected to stress and wear. To simulate regular wear, both sets of fabric samples were subjected to abrasion tests. These tests are designed to mimic the friction and stress that fabrics endure during their lifespan. The durability of a fabric is often gauged by its ability to retain integrity and functionality after repeated abrasive wear, which reflects on the quality of the material for potential uses such as clothing, furniture upholstery, or industrial applications. The abrasion resistance analysis was done by a double-head rotary platform technique through ASTM D-3884-09. For each specimen, a rubbing test of 50 cycles was done and the discrepancy in specimen mass before and after abrasion was studied. Once the abrasion tests were completed, the weight of the fabric samples was recorded. These measurements were crucial in quantifying the percentage of abrasion resistance. By comparing pre-test and post-test

weights, we calculated the mass lost due to the abrasion, indicating how much of the material was worn away. A lower percentage of weight loss signifies increased resistance to abrasion, a desirable trait in many textile applications. As shown in Table 2, the abrasion resistance of the treated specimens is higher than the untreated specimens. From the analysis of the data obtained, treated samples indicated as A, B, C, and D, showcased a significant enhancement in both abrasion resistance and tensile strength when contrasted with their raw counterparts. This improvement is a testament to the effectiveness of the nanomaterial treatments employed, contributing to the overall performance and lifespan of the fabrics. Within the treated samples, a compelling insight was that Sample A led the treated warp/weft group with an impressive abrasion resistance of 91.68% and a 30.11% increase in tensile strength. Similarly, in the nonwoven category, Sample C outperformed others with an exceptional 86.51% abrasion resistance and a marked 34.54% improvement in tensile strength. This is due to the presence of strontium titanate and its special structural characteristics and the bond formation of this nanoparticle with fiber. The findings of the study illuminate the positive impact that fabric treatments can impart on the functional attributes of textile materials. The evidence indicates that through scientific processing and treatment, even fabrics that are inherently less resistant to wear and tension can be significantly fortified, thus extending their potential applications and service life. The implications of such developments hold substantial value for the textile industry, which constantly seeks to innovate and improve material performance to meet the demands of various consumer and industrial markets.

Table 2. Abrasion resistance and tensile strength of samples.

Sample	Fabric weight before abrasion (g)	Fabric weight after abrasion (g)	Abrasion resistance (%)	Tensile strength(MPa)	Improved tensile strength (%)
Raw (warp/weft)	5.896	4.993	84.68	0.694	
A	6.744	6.183	91.68	0.993	30.11
B	6.193	5.507	88.92	0.862	19.48
Raw (nonwoven)	4.075	3.188	78.23	0.451	
C	4.842	4.189	86.51	0.689	34.54
D	4.905	4.173	85.07	0.617	26.90

Anti-inflammatory analysis

Anti-inflammatory properties in fabric play a crucial role in providing relief to individuals with sensitive skin or skin conditions. Redness, irritation, and itching are common issues that many people face, and these can be exacerbated by wearing certain fabrics. However, fabric treated with nano strontium titanate and zinc titanate contains nanoparticles that possess anti-inflammatory properties. These nanoparticles help to reduce inflammation and soothe the skin, providing a much-needed respite for those with skin sensitivities. Based on the Winter method [24], before and after

carrageenan injection, the diameter of the hind paw was calculated by a caliper, and every one-hour measuring was repeated. The results are shown in Figure 3 as an edema diagram. The control sample quickly reduced the edema, but samples (A–D) demonstrated the anti-inflammatory properties after 2 h, and after 5–6 h the effect of samples A and C were close to each other, while samples B and D had anti-inflammatory properties but not as well as samples A and C. Nano strontium titanate, a compound composed of strontium, titanium, and oxygen, is known for its unique properties that make it a valuable addition to

fabric treatments. When incorporated into the fabric, nano strontium titanate enhances the anti-inflammatory properties, providing a soothing effect to the wearer. Nano strontium titanate reduces the production of inflammatory cytokines, which are responsible for triggering inflammation in the body. The nanoparticles in the fabric interact with the skin, releasing ions that modulate the inflammatory response, thereby reducing redness, irritation, and itching. This is particularly beneficial for individuals with sensitive skin or skin conditions such as eczema or dermatitis. Furthermore, nano strontium titanate has been found to have antioxidant properties, which contribute to its anti-inflammatory effects. Oxidative stress is a common factor in many inflammatory conditions, and the presence of antioxidants helps neutralize harmful free radicals, reducing inflammation and promoting skin health. The incorporation of nano strontium titanate into fabric treatments harnesses these beneficial properties, offering a unique solution for individuals seeking comfortable and skin-friendly clothing options.

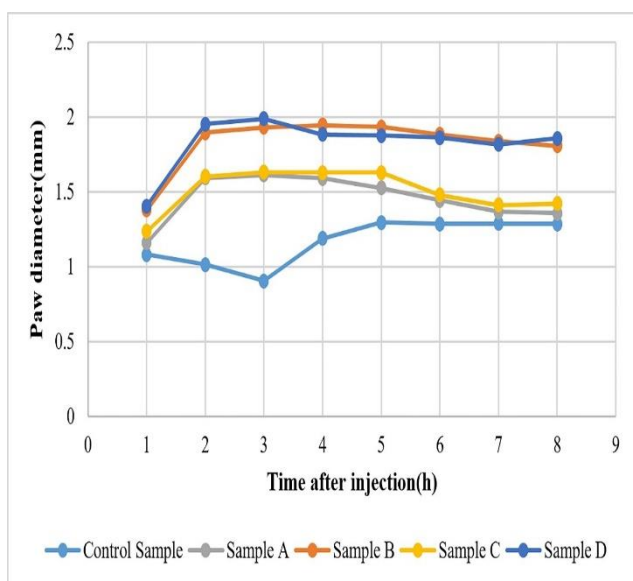


Figure 3. Inflammatory diagram of samples.

CONCLUSION

The results gained in this paper demonstrate that the kind of texture affects final product properties. Also, using nanomaterials (strontium titanate and zinc titanate) besides the method of composite fabrication can improve the chemical and physical properties. The anti-inflammatory properties of produced samples increased due to nanoparticle interaction with the skin cells and releasing ions which modulate the inflammatory response. The strength and abrasion resistance of the produced samples enhanced and the results indicate that strontium titanate has a better

effect in this experiment. On the other hand, the antibacterial properties of the samples were very good for both texture and materials, against both negative and positive bacteria, which makes this product a suitable option for mass production. Accordingly, the research not only contributes valuable data and insights to the fabric production sector but also propels forward the understanding of how different treatments can fundamentally alter the characteristics of both traditionally woven and nonwoven textiles. Moreover, future work can focus on characterizing the structural and functional properties of nanofibers containing nano strontium titanate and zinc titanate. Additionally, efforts can be made to explore new applications for these nanofibers, such as antimicrobial coatings or water purification membranes. By addressing the current limitations and conducting comprehensive research on nanofibers containing nano strontium titanate and zinc titanate, we can unlock their full potential and contribute to advancements in various technological fields.

ACKNOWLEDGMENT

This work was supported by Islamic Azad University-Yazd Branch.

REFERENCES

- [1] L. Karimi, S. Zohoori, J. Nanostruct. Chem. 3 (2013) 32. <https://doi.org/10.1186/2193-8865-3-32>.
- [2] H. Khouni, N. Bouzit, Polym. Polym. Compos. 28 (2019) 451–461. <https://doi.org/10.1177/0967391119887573>.
- [3] T.G. Arul, V. Perumal, R. Thanigaivelan, Chem. Ind. Chem. Eng. Q. 28 (2022) 247–253. <https://doi.org/10.2298/ciceq210501036a>.
- [4] J.I. Humadi, M.A. Shihab, G.S. Ahmed, M.A. Ahmed, Z.A. Abdullah, S. Sehgal, Chem. Ind. Chem. Eng. Q. 30 (2023) 151–159. <https://doi.org/10.2298/ciceq230208020h>.
- [5] Q. Li, J. Zhou, L. Fu, C. Chen, S. Mao, Z. Pu, J. Yang, J.-W. Shi, K. Wu, J. Alloys Compd. 925 (2022) 166747. <https://doi.org/10.1016/j.jallcom.2022.166747>.
- [6] S. Singh, S. Perween, A. Ranjan, J. Phys. Chem. Solids 158 (2021) 110221. <https://doi.org/10.1016/j.jpcs.2021.110221>.
- [7] A. Kumar, M. Sharma, A. Amari, R. Vaish, Environ. Res. 240 (2024) 117541. <https://doi.org/10.1016/j.envres.2023.117541>.
- [8] Z. Cai, J. Li, Y. Wang, J. Alloys Compd. 489 (2010) 167–169. <https://doi.org/10.1016/j.jallcom.2009.09.044>.
- [9] R. Mohammadisaghand, S. Zohoori, A. Shahbeighassanabadi, F. Mohammadisaghand, F. Mousavi, V. Shorabi, J. Nat. Fibers 20 (2023) 2152150. <https://doi.org/10.1080/15440478.2022.2152150>.
- [10] S. Zohoori, L. Karimi, A. Nazari, Fibres Text. East. Eur. 22 (2014) 91-95.

- https://www.researchgate.net/publication/263235187_Phocatalytic_Self-cleaning_Synergism_Optimization_of_Cotton_Fabric_using_Nano_SrTiO3_and_Nano_TiO2.
- [11] S. Zohoori, L. Karimi, *Fibers Polym.* 14 (2013) 996–1000. <https://doi.org/10.1007/s12221-013-0996-4>.
- [12] T. Zhang, E. Du, Y. Liu, J. Cheng, Z. Zhang, Y. Xu, S. Qi, Y. Chen, *Int. J. Nanomed.* 15 (2020) 1457–1468. <https://doi.org/10.2147/ijn.s228839>.
- [13] U. Gunpath, H.R. Le, A. Besinis, C. Tredwin, R. Handy, *Int. J. Nanomed.* 14 (2019) 3583–3600. <https://doi.org/10.2147/ijn.s199219>.
- [14] G. Baysal, *Int. J. Biol. Macromol.* 254 (2024) 127678. <https://doi.org/10.1016/j.ijbiomac.2023.127678>.
- [15] T. Bayisa, G.D. Edossa, N.K. Gupta, L.G. Inki, *Sci. Afr.* 22 (2023) 01977. <https://doi.org/10.1016/j.sciaf.2023.e01977>.
- [16] F. Yamin, F. Naddafiun, S. Zohoori, *J. Nat. Fibers.* 19 (2022) 6770–6779. <https://doi.org/10.1080/15440478.2021.1932675>.
- [17] M. Monavari, S. Zohoori, A. Davodiroknabadi, *Micro Nano Lett.* 17 (2022) 210–215. <https://doi.org/10.1049/mna2.12125>.
- [18] S. Zohoori, S. Shahsavari, M. Sabzali, S.A. Hosseini, R. Talebikatieklahijany, Z. Morshedzadeh, *J. Nat. Fibers.* 19 (2022) 8937–8945. <https://doi.org/10.1080/15440478.2021.1975600>.
- [19] N. Kooshamoghadam, S. Zohoori, M. Bekrani, S. Shahsavari, R. Talebikatieklahijany, *J. Nat. Fibers.* 19 (2022) 4846–4853. <https://doi.org/10.1080/15440478.2020.1870631>.
- [20] M.S. Al-Khatib, H. Khyami-Horani, E. Badran, A.A. Shehabi, *Diagn. Microbiol. Infect. Dis.* 59 (2007) 383–387. <https://doi.org/10.1016/j.diagmicrobio.2007.06.014>.
- [21] M.J. Ormsby, S.A. Johnson, N. Carpena, L.M. Meikle, R.J. Goldstone, A. McIntosh, H.M. Wessel, H.E. Hulme, C.C. McConnachie, J.P.R. Connolly, A.J. Roe, C. Hasson, J. Boyd, E. Fitzgerald, K. Gerasimidis, D. Morrison, G.L. Hold, R. Hansen, D. Walker, D.G.E. Smith, D.M. Wall, *Cell Rep.* 30 (2020) 2297–2305. doi:10.1016/j.celrep.2020.01.078. <https://pubmed.ncbi.nlm.nih.gov/32075765/>.
- [22] K.M. Rao, M. Suneetha, G.T. Park, A.G. Babu, S.S. Han, *Int. J. Biol. Macromol.* 155 (2020) 71–80. <https://doi.org/10.1016/j.ijbiomac.2020.03.170>.
- [23] M. Wang, M. Zhang, M. Zhang, M. Aizezi, Y. Zhang, J. Hu, G. Wu, *Carbohydr. Polym.* 217 (2019) 15–25. <https://doi.org/10.1016/j.carbpol.2019.04.042>.
- [24] C.A. Winter, E.A. Risley, G.W. Nuss, *Exp. Biol. Med.* 111 (1962) 544–547. <https://doi.org/10.3181/00379727-111-27849>.

MAHBOUBEH ASAL¹
 ABOLFAZL
 DAVODIROKNABADI²
 MOHAMMAD MIRJALILI¹
 ALI NAZARI³

¹Department of Textile
 Engineering, Yazd Branch,
 Islamic Azad University, Yazd,
 Iran

²Department of Design and
 Clothing, Yazd Branch, Islamic
 Azad University, Yazd, Iran

³Department of Art &
 Architecture, Yazd Branch,
 Islamic Azad University, Yazd,
 Iran

UTICAJ TEKSTURE I NANOMATERIJALA NA KARAKTERISTIKE PROIZVEDENIH PRIRODNIH VLAKANA

*Ovo istraživanje procenjuje uticaj vrste teksture i nanomaterijala na konačna svojstva tkanine. Pamučna tkanina od 100% osnove i elektrosprenovana celulozna nano tkanina, koje su tretirane stroncijum-i cink-titanatom, proizvedene su posebnom metodom. Skenirajuća elektronska mikroskopija i mapiranje elemenata dokazali su postojanje nanočestica i pomogli u analizi morfologije proizvedenih uzoraka. Rezultat bakterioidnog svojstva i njegove trajnosti tokom ciklusa pranja protiv *Escherichia coli* i *Bacillus cereus* (dve uobičajene gram-negativne/pozitivne bakterije) je bio odličan. Čvrstoća i otpornost na abraziju tretiranih uzoraka je veća od neobrađenih uzoraka zbog prisustva nanočestica i njihovih posebnih strukturnih karakteristika i formiranja veze ovih nanočestica sa vlaknima. Takođe, antiinflamatorna svojstva uzoraka su poboljšana u poređenju sa kontrolnim uzorcima usled smanjenja proizvodnje inflamatornih citokina nanomaterijalima.*

Ključne reči: stroncijum titanat, cink titanat, antiinflamatorno, elektrospinovanje, tekstura.

MASANORI YOSHIDA
TOSHIKI KOSAKA
YOSHIKI MUKAI
KOICHI NAKAHARA
RENO KIYOTA

Department of Applied
Sciences, Muroran Institute of
Technology, Muroran, Japan

SCIENTIFIC PAPER

UDC 66.021.4:66:544

GAS-LIQUID DISPERSION AGITATED BY CLOSED TURBINE-TYPE IMPELLER

Article Highlights

- A turbine-type impeller having shrouds (closed impeller, CI) is applied to gas-liquid agitation
- Formation of the gas cavities and dispersion as the gas bubbles through the CI are characterized
- The power consumption of CI in operation handling gas-liquid dispersion is assessed

Abstract

Gas-liquid agitation by a turbine-type impeller having shrouds structurally (closed disk turbine impeller, CDT) was studied by examination of the flow behavior of the gas-liquid mixture in the impeller region, with energy consideration based on the impeller power characteristics in the gassed liquid. The way in formation of the gas cavities and dispersion as the gas bubbles using the CDT differed from that using a conventional disk turbine impeller (open impeller, ODT). The difference in relative power consumption, i.e., the ratio of gassed to ungassed power consumption, between the CDT and ODT was related to the configurations of the gas cavities.

Keywords: gas-liquid agitation; closed turbine type impeller; gas cavity; impeller region; power characteristics.

A vessel agitated by a mechanically rotating impeller is a typical apparatus to perform chemical processes involving the operation of dispersions such as gas-liquid mixtures. The impeller improves the gas-liquid contact, dispersing sparged gas as gas bubbles, thereby enhancing phenomena of reaction and mass transfer between the gas and liquid phase. A shearing deformation action is desired for the impeller to generate the gas bubbles in the liquid in a turbulent flow. Preferably, a disk turbine impeller with six flat blades has been employed because of its relatively strong action. However, flat-bladed turbine-type impellers have an important weakness when used for gas-liquid agitation [1]. Studies [2–8] have emphasized the variable configurations of gas cavities forming behind the impeller blades. That variation affects the

capacity of the impeller to handle the gas or the power input by the impeller. Information about impellers improved in use for gas-liquid agitation is available in the literature [9–12]. One proposal is a disk turbine impeller with six hollow (concave) blades [13,14]. The concave bladed turbine impeller had an enhanced gas-handling capacity. Additionally, the power fall under gassing was alleviated, compared with that for the flat-bladed turbine impeller. These improved performances were attributed to reduced formation of the gas cavities [15–18]. Because the gas cavities play a role in generating the gas bubbles, their formation should be evaluated for effectiveness rather than the result of reduction.

Previously, we proposed a design of an agitation impeller with the alteration of a conventional turbine-type impeller [19]. A concept of the alternative design was for the impeller blades to transmit energy fully. This impeller, which has shrouds structurally, was named a “closed disk turbine impeller (CDT)” in contrast with a conventional “open disk turbine impeller (ODT)”. In a baffled vessel agitated by the CDT, the internal liquid flow in the impeller rotation region was examined to be analyzed for energy consideration [19]. A comparison of the power characteristics between the CDT and ODT

Correspondence: M. Yoshida, Department of Applied Sciences, Muroran Institute of Technology, 27-1, Mizumotocho, Muroran 050-8585, Japan.

E-mail: myoshida@mmm.muroran-it.ac.jp

Paper received: 11 April, 2024

Paper revised: 20 June, 2024

Paper accepted: 16 July, 2024

<https://doi.org/10.2298/CICEQ240411027Y>

demonstrated an increased transmission of energy and its possibly uniformized dissipation. The CDT has a higher efficiency of energy transmission. Additionally, the centrifugal action with the CDT is advantageous to produce the radial flow with a high level of turbulence. Accordingly, a successful performance is expected for the CDT agitating mixtures in dispersion systems.

In the present work, the closed disk turbine impeller (CDT) was applied to gas-liquid agitation. Visual observation using a video camera was made for the region of impeller rotation with gas sparging into liquid. The flow behavior of the gas-liquid mixture for the CDT was investigated and characterized with emphasis on the formation of the gas cavities and dispersion as the gas bubbles, by contrast with that for the open disk turbine impeller (ODT). The power characteristics of CDT in the gassed liquid were evaluated in relation to the operation of the gas-liquid dispersion.

EXPERIMENTAL

An experimental setup was constituted with a standard agitation vessel and a gassing system. A fully baffled cylindrical vessel with a flat base made of transparent acrylic resin (300 mm inner diameter, D_i) was used. Four vertical baffles with a width of $D_i/10$ were fitted along the internal wall of the vessel, spaced equally around the circumference. The un-gassed liquid depth was maintained at D_i , i.e., 300 mm. Figure 1 shows the closed impeller designs [19]. Its diameter, D_i ,

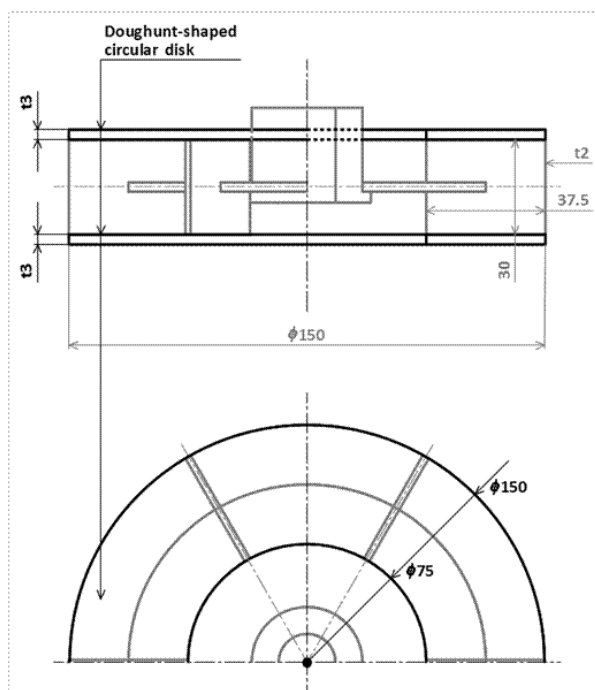


Figure 1. Schematic drawing of a closed impeller (dimensions in mm).

was 150 mm ($=D_i/2$). An open impeller of equal size in D_i was used for comparison. The respective impellers

were set at a height of $D_i/3$ from the vessel bottom. The impeller rotation rate, N_i , was varied from 50 to 200 rpm. A single-hole nozzle of 5.0 mm inner diameter was used for air sparging. The volumetric gas flow rate, Q , was varied from 5 to 70 L min^{-1} for the superficial gas velocity, V_s , of 0.12–1.65 cm s^{-1} .

Visualization of the gas behavior as it is sparged into the liquid within the vessel was done based on views from the bottom and the front. In the bottom view, the conditions were observed for the impeller to capture the gas and generate gas bubbles. In the front view, the conditions of the bubble dispersion were observed in the bulk liquid. The gas behaviors were recorded as continuous images using a video camera with a 1000 fps frame rate. For the liquid flows produced by the respective impellers, the results measured with PTV, which were presented in the earlier reports [19,20], were used as references. The impeller power consumption was determined by measuring the torque with strain gauges fitted onto the shaft [19,20].

RESULTS AND DISCUSSION

Flow behavior of gas-liquid mixture

Figure 2 depicts the region where the impeller rotates at the rate, N_i , of 140 rpm under the condition of gassing in the superficial gas velocity, V_s , of 0.12 cm s^{-1} (the open impeller (ODT) - Fig. 2(a) and the closed impeller (CDT) - Fig. 2(b). The aeration number is defined as follows:

$$N_a = \frac{Q}{N_i D_i^3} \quad (1)$$

For its value of 0.011, the agitation level is evaluated as relatively larger than the aeration level [21]. In the ODT operated under this aeration-agitation rate condition, the vortex cavities [22] remained stable, forming on the rear sides near the upper and lower edges of the impeller blades. The sparged gas was captured steadily by the cavities. The gas bubbles were generated continuously from the end of the cavities into the bulk liquid [23]. The upper and lower edges of the CDT blades are shrouded with doughnut-shaped disks. Therefore, no vortex cavity was observed in a form similar to that forming behind the ODT blades. With the use of the CDT, the sparged gas was aggregated as cavities on the rear sides of the impeller blades. Each cavity grew circumferentially long. Generation of the gas bubbles occurred radially around the exit of the impeller rotation region.

For the ODT in such an operational condition, it has been known that the path-line of sparged gas is

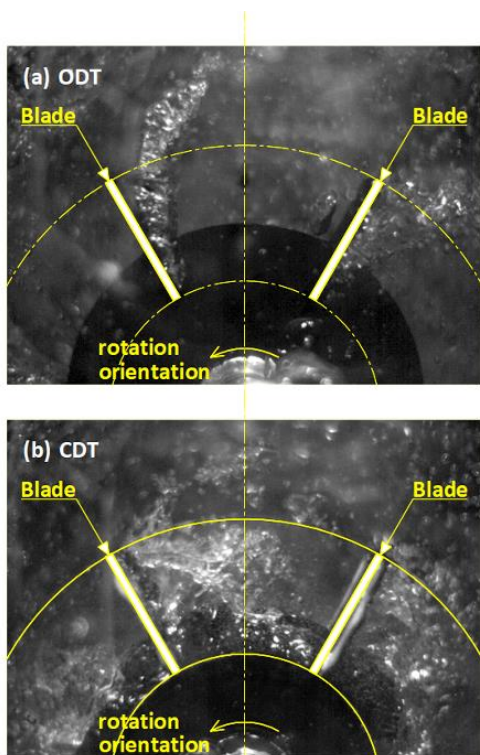


Figure 2. Bottom view of impellers of (a) open and (b) closed type rotating with gassing under lower aeration rate condition.

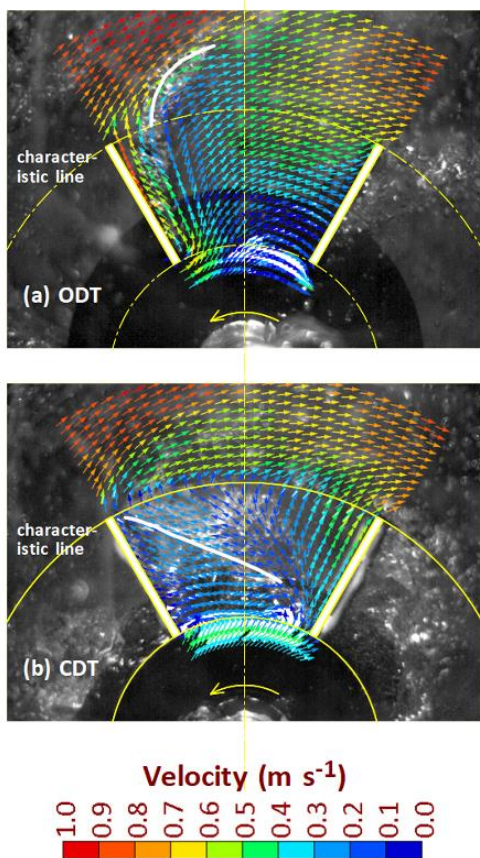


Figure 3. Gas behavior and liquid flow in regions of (a) open and (b) closed impellers.

almost the same as that of liquid in single-phase flow [23]. Figure 3 illustrates a profile of the velocity in single-phase liquid flow [19] superimposed on the image of the impeller handling the gas-liquid mixture. The velocity profiles were determined on the different heights of horizontal planes. The figure (a) is for the open impeller (ODT). The profile at the height of 6 mm above the lower blade edge was picked up. The figure shows the vectors for the flow velocity relative to the impeller rotation. As expected for the ODT, the path line of the sparged gas coincides with that of the liquid flow. In the impeller inside the region, the gas behavior and the liquid flow were in common characterized as an intensified stream with radial discharge behind the blade. Outside the impeller, an elongated zone with a larger velocity gradient in the liquid flow was detected, possibly because of a rotation flow in the trailing vortex. A line to characterize such a zone overlapped the trajectory of the gas cavity. The figure (b) is for the closed impeller (CDT). The profile at the height of 2 mm above the lower blade edge was picked up. The CDT had the path-line common to the gas and liquid. For the internal region, the liquid flow was found to be distributed into the front and rear sides between the impeller blades. A line to characterize the distributary was detected. On the line, the gas cavity is formed by handling the gas-liquid mixture. Such a flow field appears to be attributable to the flow produced secondarily as a consequence of the shrouding disk fitted to the blade edges.

To observe the efficacy of the shrouding disk, the profile of the circumferential flow velocity was investigated for the single-phase liquid between the blades. Figure 4 shows the circumferential velocities of the inflow (40.0 mm radial position) and outflow (72.5 mm radial position) in the developed view of the faces of the circular cylinders forming in the respective positions, where the flow velocity is relative to the impeller rotation. Plates (a) and (b) in the figure are related respectively to the open impeller (ODT) and the closed impeller (CDT). For the ODT, the flows toward the front surface of the blade were observed in most parts of the region. In the CDT, the flows were induced, as caused by the pressure gradient [24,25]. They trended from the front of higher pressure to the back of lower pressure. Such a secondary flow, which was detected in the layer near the inner surface of the shrouding disk, extended axially and covered the entire blade surface. The gas cavity in the gas-liquid system is believed to form in the orientation from higher to lower pressure according to the pressure gradient.

Figure 5 depicts the gassed regions of the ODT (a) and the CDT (b) under the conditions of the impeller

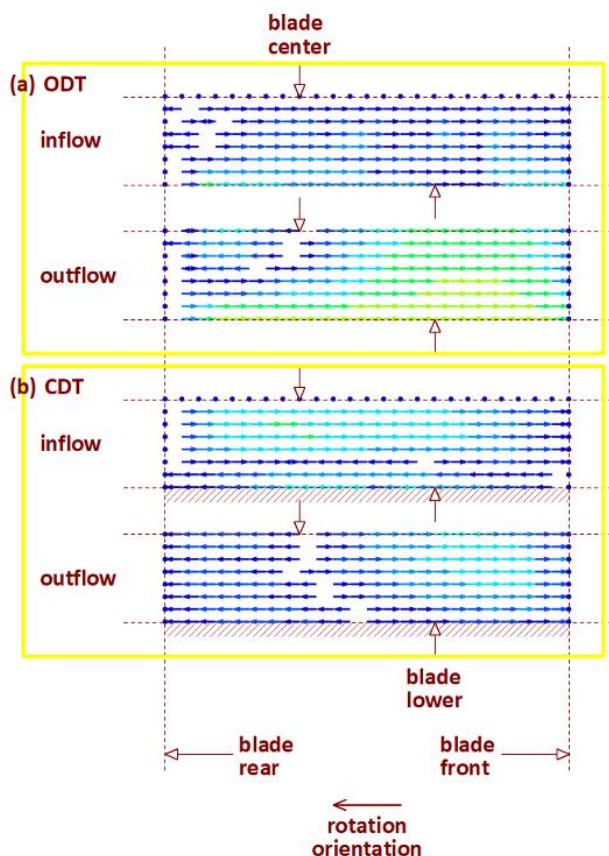


Figure 4. Circumferential liquid flows between blades of (a) open and (b) closed impellers. The scale of the velocity vector is the same as that in Fig. 3.

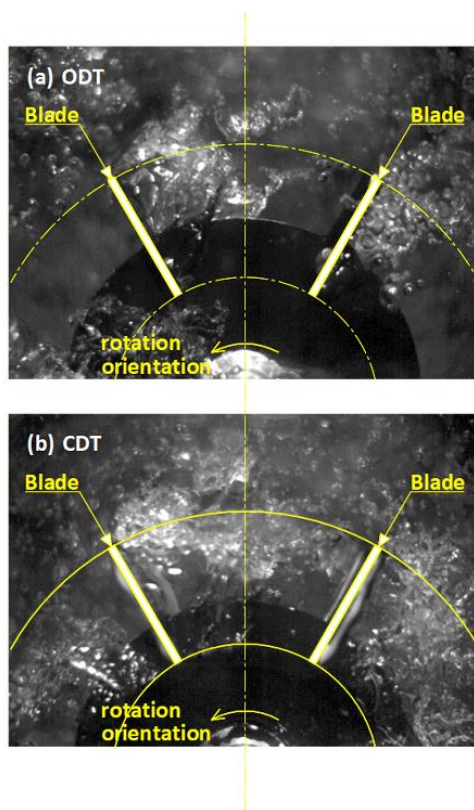


Figure 5. Bottom view of impellers of (a) open and (b) closed type rotating with gassing under higher aeration rate condition.

rotation rate, N_r , of 140 rpm and the superficial gas velocity, V_s , of 0.47 cm s^{-1} . Then, the aeration number, N_a , of 0.042 indicates a relatively increased aeration level [21]. In the ODT, vortex-like cavities clinging to the blades and larger cavities blanketing the blades formed alternately [22]. As compared the image (a) between Figs 2 and 5, generation of the gas bubbles through the large cavities tended to deviate from the radial direction to the circumferential direction. Reduction in gas dispersion was suggested due to the formation of the large cavities hindering a part of the radially outward liquid flow [23]. Comparison of image (b) between Figs 2 and 5 demonstrated with the CDT that the aeration-agitation rate condition exerted a slight effect on the formation of the cavities and generation of the gas bubbles: the circumferentially long cavities generated effectively the gas bubbles in a radially outward direction. The dependence of gas dispersion on the operational condition was found to differ between the ODT and CDT. This suggests a difference in centrifugal effect in the gas cavities forming in the respective impellers. As shown in Fig. 4, the circumferential outflow velocity relative to the impeller rotation was smaller overall with the CDT than with the ODT. That is, the CDT produces a flow field rotating with larger absolute velocities, which can lead to a favorable centrifugal effect.

Relation between power consumption and cavity formation

The formation of gas cavities behind the impeller blades and dispersion as gas bubbles within the vessel can affect energy transmission through the impeller [22]. This effect has been assessed in terms of the ratio of gassed power consumption to ungassed one of the impellers, P_{mg}/P_{m0} . Changes in the power consumption are observed with variation of the impeller rotation rate, N_r , under a constant condition of the superficial gas velocity, V_s , or with the variation of V_s under a constant condition of N_r . Here, the latter approach was employed. The results were coordinated in terms of the aeration number, N_a . Figure 6 shows the relationships between P_{mg}/P_{m0} and N_a for the ODT and CDT, respectively. When the ODT was operated at a lower rotation rate such as 50 rpm, the impeller had ineffectual dispersions according to the flow regime map [21]. Then, the P_{mg}/P_{m0} values close to 1, which indicate a power characteristic unaffected by gassing, can reflect unsatisfactory dispersions. For the CDT operated at the rotation rate of 50 rpm, decreases in P_{mg}/P_{m0} were observed, suggesting some level of successful working of the impeller. With the increase of the impeller rotation rate, on the whole, P_{mg}/P_{m0} tended to decrease commonly for the ODT and CDT. The ODT, being operated at a higher rotation rate such as

200 rpm, had larger decreases in P_{mg}/P_{m0} under higher aeration rate conditions, probably because of the formation of the large cavities [21]. For the CDT, decreases in P_{mg}/P_{m0} were smaller than those for the ODT, which supports the smaller effect of the aeration-agitation rate condition on the formation of the cavities. Additionally, as predicted from the images presented in Fig. 7, the impeller region shrouded by the hollow disk can function to capture the sparged gas. Increased gas hold-up in the impeller region is regarded as potentially contributing to the power reduction.

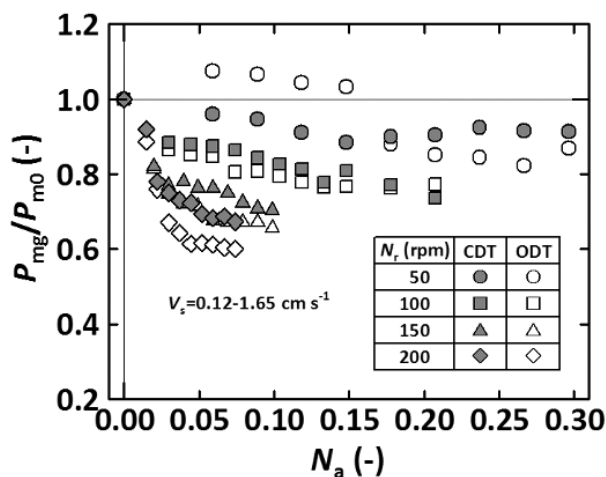


Figure 6. Relationships between relative power consumption and aeration number for open and closed impellers.

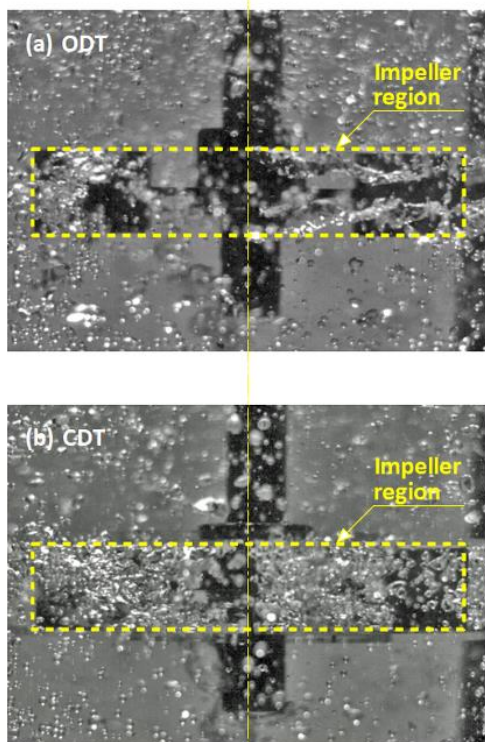


Figure 7. Front view of impellers of (a) open and (b) closed type rotating with gassing under lower aeration rate condition.

Overall, the power characteristics of CDT were perceived as stable with variations in the operational conditions. This demonstrates for the CDT the higher efficiency of energy transmission through the impeller and the effective gas-liquid agitation by the impeller for widely various aeration-agitation rates.

Moreover, to confirm the effective gas-liquid agitation by the CDT, more quantitative examinations are desired for mass transfer enhancement in terms of the volumetric coefficient, including the gas hold-up and gas bubble diameter.

CONCLUSION

The flow behavior of the gas-liquid mixture agitated by the closed disk turbine impeller (CDT) was examined through flow visualization and measurement, in comparison with that agitated by the open disk turbine impeller (ODT). In the CDT, the path-line for the motion was common to the sparged gas and single liquid, as is the case with that for the vortex motion characteristic in the ODT. The cavities forming in the CDT generated gas bubbles, nearly independent of the aeration-agitation rate condition. The ratio of gassed-to-ungassed power consumption of the impeller was assessed as a reflection of the formation of the gas cavities and dispersion of the gas bubbles. For widely various aeration-agitation rates, energy transmission through the CDT was revealed to be better than that through the ODT forming the large cavities.

NOMENCLATURE

D_i	impeller diameter, mm
D_t	vessel diameter, mm
N_a	aeration number
N_r	impeller rotation rate, rpm
P_{m0}	ungassed impeller power consumption, W
P_{mg}	gassed impeller power consumption, W
Q	volumetric gas flow rate, L min ⁻¹
V_s	superficial gas velocity, cm s ⁻¹

REFERENCES

- [1] G.M. Mule, A.A. Kulkarni, Chem. Ind. Dig. July (2015) 58–64. <https://www.researchgate.net/publication/358901096>.
- [2] H.R. Lee, Y.J. Huh, C.S. Choi, W.H. Lee, Kor. J. Chem. Eng. 9 (1992) 164–168. <https://doi.org/10.1007/BF02705134>.
- [3] V.V. Ranade, V.R. Deshpande, Chem. Eng. Sci. 54 (1999) 2305–2315. [https://doi.org/10.1016/S0009-2509\(98\)00301-7](https://doi.org/10.1016/S0009-2509(98)00301-7).
V.V. Ranade, M. Perrard, C. Xuereb, N. Le Sauze, J. Bertrand, Chem. Eng. Res. Des. 79 (2001) 957–964. <https://doi.org/10.1205/02638760152721190>.
- [4] M. Mochizuki, H. Sato, Y. Doida, Y. Saita, T. Amanuma, T.

- Takahashi, Kagaku Kogaku Ronbunshu 34 (2008) 557–561. <https://doi.org/10.1252/kakoronbunshu.34.557>.
- [5] F. Maluta, A. Paglianti, G. Montante, Chem. Eng. Sci. 241 (2021) 116677. <https://doi.org/10.1016/j.ces.2021.116677>.
- [6] C. Yang, H. Lu, B. Wang, Z. Xu, B. Liu, Chem. Eng. Sci. 280 (2023) 119058. <https://doi.org/10.1016/j.ces.2023.119058>.
- [7] F. Maluta, F. Alberini, A. Paglianti, G. Montante, Chem. Eng. Res. Des. 194 (2023) 582–596. <https://doi.org/10.1016/j.cherd.2023.05.006>.
- [8] R. Sardeing, J. Aubin, C. Xuereb, Chem. Eng. Res. Des. 82 (2004) 1589–1596. <https://doi.org/10.1205/cerd.82.12.1589.58030>.
- [9] Z. Zheng, D. Sun, J. Li, X. Zhan, M. Gao, Chem. Eng. Res. Des. 130 (2018) 199–207. <https://doi.org/10.1016/j.cherd.2017.12.021>.
- [10] D. Gu, Y. Mei, L. Wen, X. Wang, Z. Liu, J. Taiwan Inst. Chem. Eng. 121 (2021) 20–28. <https://doi.org/10.1016/j.jtice.2021.03.038>.
- [11] D. Li, W. Chen, Process Saf. Environ. Prot. 158 (2022) 360–373. <https://doi.org/10.1016/j.psep.2021.12.019>.
- [12] F. Saito, A.W. Nienow, S. Chatwin, I.P.T. Moore, J. Chem. Eng. Jpn. 25 (1992) 281–287. <https://doi.org/10.1252/jcej.25.281>.
- [13] J. Zhao, Z. Gao, Y. Bao, Chin. J. Chem. Eng. 19 (2011) 232–242. [https://doi.org/10.1016/S1004-9541\(11\)60160-2](https://doi.org/10.1016/S1004-9541(11)60160-2).
- [14] B.H. Junker, M. Stanik, C. Barna, P. Salmon, E. Paul, B.C. Buckland, Bioprocess Eng. 18 (1998) 401–412. <https://doi.org/10.1007/s004490050463>.
- [15] M. Cooke, P.J. Heggs, Chem. Eng. Sci. 60 (2005) 5529–5543. <https://doi.org/10.1016/j.ces.2005.05.018>.
- [16] G. Montante, A. Paglianti, Chem. Eng. J. 279 (2015) 648–658. <http://dx.doi.org/10.1016/j.cej.2015.05.058>.
- [17] D. Gu, L. Wen, H. Xu, M. Ye, J. Taiwan Inst. Chem. Eng. 143 (2023) 104688. <https://doi.org/10.1016/j.jtice.2023.104688>.
- [18] M. Yoshida, H. Ebina, K. Ishioka, K. Oiso, H. Shirotsuki, R. Tateshita, Int. J. Chem. React. Eng. 15 (2017) 20160198. <https://doi.org/10.1515/ijcre-2016-0198>.
- [19] M. Yoshida, H. Ebina, H. Shirotsuki, K. Ishioka, K. Oiso, Braz. J. Chem. Eng. 32 (2015) 865–873. <https://doi.org/10.1590/0104-6632.20150324s00003682>.
- [20] J.C. Middleton, in Mixing in the process industries, N. Harnby, M.F. Edwards, A.W. Nienow Eds., Butterworth-Heinemann, Oxford (1992), pp. 322–363. ISBN-13: 978-0750637602.
- [21] W. Bruijn, K. van't Riet, J.M. Smith, Trans. Inst. Chem. Eng. 52 (1974) 88–104. ISSN: 0046-9858.
- [22] K. van't Riet, J.M. Smith, Chem. Eng. Sci. 28 (1973) 1031–1037. [https://doi.org/10.1016/0009-2509\(73\)80005-3](https://doi.org/10.1016/0009-2509(73)80005-3).
- [23] K. Brun, R. Kurz, Int. J. Rotating Mach. 1 (2005) 45–52. <https://doi.org/10.1155/IJRM.2005.45>.
- [24] C. Wu, K. Pu, C. Li, P. Wu, B. Huang, D. Wu, Energy 246 (2022) 123394. <https://doi.org/10.1016/j.energy.2022.123394>.

MASANORI YOSHIDA
TOSHIKI KOSAKA
YOSHIKI MUKAI
KOICHI NAKAHARA
RENO KIYOTA

Department of Applied
Sciences, Muroran Institute of
Technology, Muroran, Japan

NAUČNI RAD

MEŠANJE DISPERZIJE GAS-TEČNOST TURBINSKOM MEŠALICOM ZATVORENOG TIPA

Mešanje gas-tečnost turbinskom mešalicom sa strukturnim omotačem (turbinska mešalica sa diskom zatvorenog tipa, CDT) proučavano je ispitivanjem ponašanja smeše gas-tečnost u regionu mešalice, uz razmatranje energije na osnovu karakteristika snage mešanja u sistemu gas-tečnost. Način formiranja gasnih šupljina i dispergovnje gasnih mehura pomoću CDT-a razlikuje se od onog pomoću konvencionalne turbinske mešalice sa diskom (otvoreno radno kolo, ODT). Razlika u relativnoj potrošnji energije, tj. u odnosu snage mešanja disperzije gas-tečnost i čiste tečnosti, između CDT i ODT, povezana je sa konfiguracijom gasnih šupljina.

Ključne reči: mešanje sistema gas-tečnost; turbinska mešalica sa diskom zatvorenog tipa; gasna šupljina; oblast mešalice; snaga mešanja.

MARKO PAVLOVIĆ¹
MARINA DOJČINOVIĆ²
JASMINA NIKOLIĆ²
ANJA TERZIĆ³
VLADIMIR PAVIĆEVIĆ²
SAŠA DRMANIĆ²
ENITA KURTANOVIĆ⁴

¹Innovation Center of Faculty
of Mechanical Engineering,
University of Belgrade, Belgrade,
Serbia

²Faculty of Technology and
Metallurgy, University of
Belgrade, Belgrade, Serbia

³Institute for Testing of
Materials, Belgrade, Serbia

⁴AD HARBI, Tvornička 3,
71210 Ilidža/Sarajevo, B&H

SCIENTIFIC PAPER

UDC 699.812:691:66.017

APPLICATION OF WASTE RAW MATERIALS AS A REINFORCEMENT FOR PROTECTIVE COATINGS BASED ON PYROPHYLLITE

Article Highlights

- Pyrophyllite was used as an 80% filler in protective coatings, with 15% silicone resin acting as a binder
- 20% of secondary raw material additions based on mullite and corundum increased the protective coating's durability
- PM20 and PC20 coatings had cavitation rates of 0.22 mg/min and 0.14 mg/min, respectively, indicating cavitation erosion resistance

Abstract

In this study, pyrophyllite was used for the first time in the composition of protective refractory coatings together with supplementary waste resources. The proposed refractory coatings are applicable for metallic and non-metallic structures, with the option of using them to protect machinery components in the chemical industry, metallurgy, and mining. Given that pyrophyllite has a low hardness, the goal was to improve the coating's resistance to cavitation erosion by adding 20 wt.% of hard refractory materials, i.e., crushed and micronized waste bricks based on mullite and corundum, respectively. Previous studies have demonstrated that protective coatings using a pyrophyllite filler have refractory qualities but insufficient resistance to cavitation erosion. As a result, the composition of refractory coatings, the preparation techniques, and the coating manufacturing process were altered. This study presents a simple method for combining conventional coatings made of refractory fillers (primary resource: pyrophyllite) with waste materials (mullite brick and corundum brick) used as reinforcement in protective refractory coatings for metal and non-metal structural elements that are highly resistant to cavitation erosion.

Keywords: construction materials; waste resources; metal substrate; microstructure; cavitation erosion.

Chemical, mechanical, and construction industry professionals are looking for innovative building materials that have the potential to reduce energy consumption, increase thermal insulation, and minimize CO₂ emissions. The world is today facing major energy issues and concerns as a result of rising

living standards and rapid population expansion. Industry (chemical, machine, building, etc.) is one of the primary sectors recognized for having a large impact on atmospheric carbon dioxide emissions, which contribute to global warming [1,2]. The primary goal is to identify new solutions to reduce CO₂ emissions in the industry sector through innovative use of alternative raw materials [3–5]. The industry aims to use raw materials from waste streams, which are resources that correspond to the Green Agenda principles [6,7]. In this experiment, discarded mullite and corundum bricks were used as an alternative raw material for reinforcement in refractory coatings.

Pyrophyllite was used in this work as the base material for producing the refractory coatings. The main

Correspondence: S. Drmanić, Faculty of Technology and Metallurgy, University of Belgrade, Karnegijeva 4, 11000 Belgrade, Serbia.

E-mail: drmana@tmf.bg.ac.rs

Paper received: 10 April, 2024

Paper revised: 18 June, 2024

Paper accepted: 17 July, 2024

<https://doi.org/10.2298/CICEQ240410029P>

characteristic of this mineral is that it is composed of two tetrahedral Si sheets placed between an Al octahedral sheet to form a layered hydroxy-aluminosilicate [8]. In octahedral form, every Al atom of pyrophyllite has four O atoms connected to Si tetrahedra. Two structural OH groups are also bound to Al atoms [9]. Pyrophyllite is characterized by its unique crystalline structure and softness of talc [10]. Due to the specific structure and the O atoms' placement between the layer surfaces, pyrophyllite is extremely resistant to acids, which is important when this mineral is employed in the design of coatings [11,12]. The typical impurities found in pyrophyllite usually include mica, bauxite, diasporite, and quartz. When heated, pyrophyllite loses the structural OH groups linked to its octahedral sheet (550 °C) and creates mullite and cristobalite (1200 °C), which are refractory mineral phases [13–15].

Pyrophyllite's main uses are in the refractory and ceramic industries, which are established by its excellent heat resistance, stable crystal structure during heating, and consistent chemical composition [16].

The resistance of substrate to different types of erosion (such as carbonation, chloride ion erosion, and cavitation erosion via water) can be greatly increased by the application of the organic-based coatings to metal or non-metal (e.g., concrete) surfaces [17–20]. Several studies have demonstrated that the most crucial elements for establishing a protective layer on the surface of a material are the organic film-forming coatings of high density and stable chemical composition [21,22]. This layer keeps metal or non-metal components inside a structure safe from corrosive environmental media (heat, moisture, and acids) [23]. Protective coatings have become more and more important as an auxiliary technology to ensure the long-term service performance of metal, concrete, and/or composite structures in residential and commercial settings [24,25].

The basic idea is to produce a relatively non-toxic, extremely erosion-resistant, and easily clean protective coating using water as the dispersing medium, a low organic content, and an inorganic raw material (filler) with a high hardness value and good grain size and shape distribution.

This study presents an easy approach to transform traditional coatings formed of refractory filler (primary resource: pyrophyllite) with waste materials (pulverized mullite brick and corundum brick) used as reinforcement in protective refractory coatings for metal and concrete structural elements that are resistant to cavitation erosion.

EXPERIMENTAL

Materials and mix-design of the coatings

Pyrophyllite (mineral formula: $\text{Al}_2\text{Si}_4\text{O}_{10}(\text{OH})_4$) was used as a base material in the mix design of experimental coatings. Since the pyrophyllite mineral belongs to the talc group, the performance and characteristics of pyrophyllite are similar to those of talc. Namely, pyrophyllite has a hardness of 1–2 on the Moh's scale of hardness, which is very low. Therefore, the addition of certain 'reinforcing' raw materials is necessary to improve the coatings' hardness and mechanical characteristics.

Pyrophyllite ore was extracted from the Parsovići deposit, located in Bosnia and Herzegovina. The usual ore sampling campaign was carried out to prepare a representative 300 kilogram sample [26]. The original pyrophyllite ore was quartered and roughly crushed using cone and jaw crushers to break the ore crude mass up into 10 kg sub-samples. After rough crushing, the subsamples (10 kg) were further milled and finally pulverized in an ultra-centrifugal mill. Pyrophyllite sub-samples were subjected to wet sieving on a series of W.S. Tyler test sieves to analyze the particle sizes (Figure 1). The average grain size of the pyrophyllite grain mixture was $d_{50}=20\mu\text{m}$. The mean grain shape factor was 0.67 (semi-round) [27,28]. The pyrophyllite mineral was found to be the dominant phase, accounting for up to 50% of all current crystalline phases, according to an X-ray diffraction examination of the pyrophyllite sample (Figure 2). In the analyzed sample, the amounts of quartz, calcite, and dolomite were less abundant, accounting for up to 30%, 10%, and 5%, respectively. Kaolinite was detected in very small amounts [29].

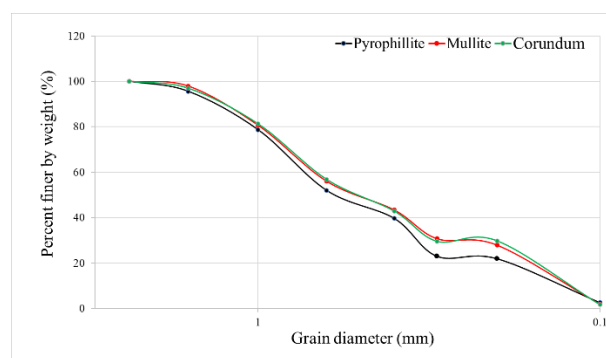


Figure 1. Grain size distribution of mineral raw materials used for filler preparation.

Mullite-based material (mullite mineral formula: $3\text{Al}_2\text{O}_3 \cdot 2\text{SiO}_2$) was used as a reinforcement in the mix design of the coating. To achieve low-cost coatings, mullite was not synthesized; instead, recycled mullite refractory bricks were employed (acquired from a local refractory construction firm). According to the

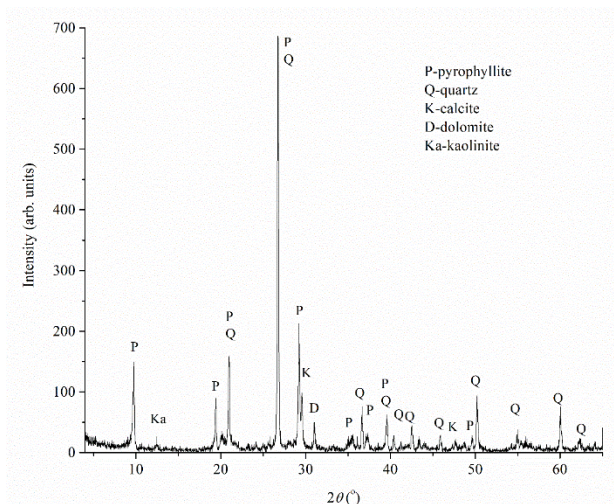


Figure 2. X-ray diffractogram of pyrophyllite sample.

Rongsheng Kiln Refractory Bricks Manufacturer, mullite is used as the primary raw material for the production of mullite bricks, which are then manufactured *via* molding and high-temperature sintering. The refractoriness of this material is as high as 1600 °C. Bulk density is 1.5 g/cm³. The cold-crushing strength is 9 MPa. The apparent initial softening temperature is 1600 °C (conditions: 0.1 MPa, 0.6%). The thermal conductivity is 0.6 W/(m·K). The maximum service temperature is 1550 °C. The samples were crushed and milled to the average d₅₀=15µm. The mean grain shape factor was 0.57 (semi-angular).

Similarly, corundum bricks (corundum mineral formula: Al₂O₃) from the same manufacturer and local distributor were used as refractory reinforcement in the coatings mix design. The refractoriness of this material is approximately 1800 °C. Bulk density is 2.5 g/cm³. The cold-crushing strength is 25 MPa. The apparent initial softening temperature is 1700 °C (conditions: 0.1 MPa, 0.6%). The thermal conductivity is 0.5 W/(m·K). The maximum service temperature is 1700–1750 °C. The samples were also crushed and milled to the average d₅₀=15µm. The mean grain shape factor was 0.53 (semi-angular).

Cordierite and mullite were also submitted to the sieve analysis to detect the grain-size distribution of these two employed raw materials (Figure 1). Based on data on grain shape [28,30,31], i.e., pyrophyllite being

semi-round while mullite and corundum being semi-angular, this mix composition is suitable for achieving a good alignment of the grains with each other during coating application, which will contribute to its hardness and adhesion and ultimately better surface protection.

The chemical composition of the raw materials was determined using atomic absorption spectrometry on a Perkin Elmer Analyst 300 instrument. Characteristics of the device: wavelength range: 185–900 nm; optical dual beam; monochromator with 1800 lines/mm; photo multiplier detector; carrier with 6 lamps with automatic positioning; flame technique; titanium burners of 10 cm and 5 cm; automatic gas flow adjustment. The chemical composition is provided in Table 1.

Table 1. Quantification of the major oxides in mineral raw materials used for filler preparation.

Oxide, %	SiO ₂	Al ₂ O ₃	Fe ₂ O ₃	CaO	MgO	K ₂ O	Na ₂ O	TiO ₂	SO ₃	LoI*
Pyrophyllite	68.30	16.20	1.49	6.27	1.14	0.61	0.38	0.15	0.01	5.45
Mullite	13.81	83.14	0.32	-	-	-	-	-	-	2.73
Corundum	2.59	95.80	0.10	-	-	-	-	-	-	1.51

* Loss on ignition at 1000 °C.

Two coatings were prepared for the experiment. The samples were labeled as PM20 and PC20. Both coatings contained pyrophyllite at 80 wt.% in the mix design of filler for coating. The recycled mullite brick was added to PM20 in 20 wt.% (of the total filler mixture mass). Similarly, the recycled corundum brick was added (20 wt.%) to PC20. Dry powders were additionally homogenized in a laboratory mixer (at ambient temperature: 20 °C) before adding liquid compounds. Siloxane resin with epoxy modification, in liquid form (purchased from manufacturer Evonik Operations GmbH), was added in 15 wt.%. According to the data sheet, SILIKOPON® EF treats successfully at ambient temperature in combination with aminosilanes. Dynasylan® AMEO is an aminosilane-based coupling agent (3.5 wt.%). The ratio between epoxy resin and coupling agent was 4.5:1. Titanium dioxide (TiO₂) (Fisher Chemicals, UK) was used as an additive in the amount of 1.5 wt.% in accordance with the recommendations by the SILIKOPON manufacturer. The mix-design of the experimentally prepared coatings is provided in Table 2.

Table 2. Mix-design of the coatings.

Sample	Mullite (%)	Corundum (%)	Pyrophyllite (%)	Siloxane resin (%)	Coupling agent (%)	Titanium dioxide (%)
PM20	20	-	80	15*	3.5*	1.5*
PC20	-	20	80	15*	3.5*	1.5*

* Of the total mass.

The powder was initially dissolved in alcohol (ethanol). Then the mixture was added to the siloxane-epoxy resin and mixed for 5 minutes. After adding the coupling agent and additive, the mixture was stirred for an additional 15 minutes. The coatings were spread on

the specimens (round steel tin plates of 2 cm diameter) via a film applicator. After the coating process, the specimens were kept at room temperature (20 °C) for 24 hours.

Instrumental methods

The experimentally produced PM20 and PC20 refractory coatings were subjected to the standard test procedure for cavitation erosion as per ASTM G32-16 [30,31]. The PM20 and PC20 samples (steel tin coated with experimentally developed coatings) were used in the experiment. The starting masses of the PM20 and PC20 samples were 25 g and 27 g, respectively. The ultrasonic vibratory cavitation method was employed with a stationary sample due to the brittle nature of the examined material. The sample holder was secured to the bottom of the water bath. The mechanical vibratory concentrator was immersed in a water bath. The water temperature remained constant at $25 \pm 1^\circ\text{C}$. The sample and the front surface of the vibratory concentrator were separated by a 0.5 mm gap. Mechanical vibrations at a frequency of 20 ± 0.2 kHz were employed. Mechanical vibrations at the concentrator top had an amplitude of 50 ± 2 μm . The distance between the test sample and the concentrator was 0.5 mm. A significant cavitation zone developed beneath the concentrator's front surface and the stationary-tested sample. The water bath was cooling the sample to keep it at a constant temperature. A constant water flow formed a pressure field, causing cavitation bubbles to implode on the surface of a sample. The water flow rate was 5–10 ml/s, and the bathroom temperature was $25 \pm 1^\circ\text{C}$. The cavitation intervals used were 0, 15, 30, 45, and 60 minutes. During testing, the materials were dried, and mass loss was recorded with an analytic accuracy of ± 0.1 mg. The test results indicate the average of at least three tests per sample.

Microstructural investigation of PM20 and PC20 samples was performed using a scanning electron microscope (SEM) (JEOL JSM-6610LV). For the recording, the carbon coating was applied using the table-top sputter coater LEICA SCD005. The magnification of the equipment ranges from 5 to 300,000 times. The electron source is a W wire (LaB 6). The voltage ranges from 0.3 to 30 kV. The instrument operates on a vacuum system.

An open-source software, JMicroVision v1.3.1.38 [32], was used as an image analysis tool. This software can measure, identify, characterize, and quantify various picture components. It supports extremely large photos and boasts a robust feature set with an easy-to-use interface. Similar to a microscope, it enables dynamic specimen observation with the option to combine several lighting or focus modes (fluorescent, polarized light, etc.). Additionally, images can be viewed simultaneously using the magnifying lens and multi-view tool. Each image has its zoom coefficient and is maintained in the same center location. Main Features: read images in TIFF, BMP, GIF, JPEG, PNG,

and PNM formats; Quantification of components—objects or background; object analysis (size, shape, orientation, texture); image processing (binary and morphology operations, filtering, segmentation); image rectification (geometric corrections by control points); digital point counting; tools for data collection in one or two dimensions; image annotation (variation of granulometry, density, objects, or background).

RESULTS AND DISCUSSION

The mass loss diagram (Fig. 3a) depicts the damage outcomes by plotting the mass loss values on the ordinate and the time of material exposure to the cavitation erosion on the abscissa. Mass loss was measured after each cavitation erosion sequence (i.e., 0, 15, 30, 45, and 60 min). Similarly, the surface degradation level of samples (Fig. 3b) is a correlation between the measured damaged surface and the surface without damage. The development of superficial pits (Fig. 3c) is presented as an interrelation between the estimated number of pits per sample and exposure time (from 15 to 60 min). The mean area of formed pits (Fig. 3b) was estimated from the number of pits using image analysis [32], and the number was correlated to the cavitation exposure duration.

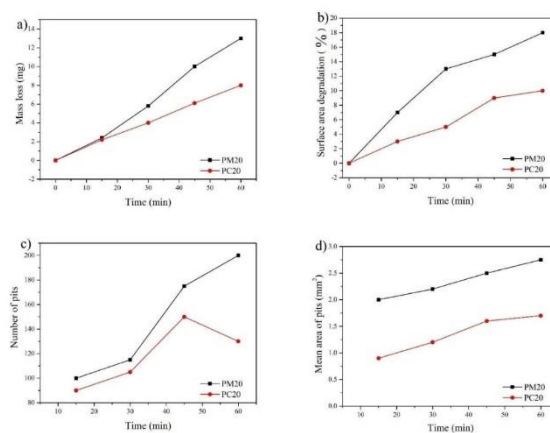


Figure 3. Test results of the refractory coatings PM20 and PC20 during cavitation erosion: (a) Mass loss; (b) Level of surface area degradation of samples; (c) Number of formed pits; (d) Mean area of formed pits.

After 15 minutes of erosion, the sample PM20 lost 2 mg, while the sample PC20 lost 1.9 mg of its starting mass. The values for both coating samples are comparable. During the following iteration of the cavitation procedure, the measured mass losses were 5.5 mg for the PM20 coating and 3.9 mg for the PC20 coating. After 45 minutes, the following values were obtained: 9.9 mg and 4.5 mg for PM20 and PC20, respectively. The final values of mass loss (60 minutes of water exposure) were 13 mg and 6.9 mg for mullite and corundum-based coatings, respectively. It can be

concluded that the mullite-based coating (PM20) was losing mass due to cavitation erosion more rapidly than the PM20 coating.

The level of surface area degradation was estimated for the PM20 and PC20 samples, whose initial surface area was 1257 mm². Estimated degraded areas on each sample (PM20 and PC20, respectively) after the cavitation erosion cycle were: 7.2% and 2.9% after 15 minutes of exposure; 12.8% and 4.3% after 30 minutes of exposure; 14.7% and 8.1% after 45 minutes of exposure; and 17.7% and 8.5% after 60 minutes of exposure. Even though the percentage of degraded areas is small, it can be noted that the degraded surface progression is more rapid for the mullite-based sample.

The estimated number of pits followed the trend of increasing which is characteristic of the PM20 sample: 98 (after 15 minutes of exposure), 109 (after 30 minutes of exposure), 173 (after 45 minutes of exposure), and 197 (after 60 minutes of exposure). The number of pits was comparatively lower for the PC20 sample for each cavitation exposure sequence: 67 (after 15 minutes), 96 (after 30 minutes), 146 (after 45 minutes), and 129 (after 60 minutes). During the last sequence for the PC20 sample, the number of pits started decreasing. By comparing diagrams Fig. 3b and Fig. 3c, it can be assumed that in the case of PC20 coating, the new pits ceased opening after 45 minutes, while the existing pits started widening or merging.

Upon estimating the degraded area, but taking into account only the area under pits, the following results are acquired: 2 mm² after 15 minutes of exposure, 2.25 mm² after 30 minutes of exposure, 2.4 mm² after 45 minutes of exposure, and 2.65 mm² after 60 minutes of exposure for the PM20 sample; and 0.9 mm² after 15 minutes of exposure, 1.1 mm² after 30 minutes of exposure, 1.3 mm² after 45 minutes of exposure, and 1.4 mm² after 60 minutes of exposure for the PC20 sample. The area under the pits was smaller for the corundum-based coating.

The corundum-based coating is more resistant to cavitation erosion than the mullite-based coating, probably due to the difference in the filler's Mohs hardness. Namely, pure mullite mineral is 6–7 on the Mohs hardness scale, while corundum is 9.

The rate of cavitation is calculated from the measured mass loss for each testing period. The points of the diagram are approximated by a straight line using the least squares method. The tangent of the slope depicts the loss of mass during the period of cavitation activity and represents the rate of cavitation erosion. For each set of tested samples, three samples were used, and the findings represent the mean value of

these measurements for each test interval. The cavitation rate given in Fig. 4 is a quantifiable measurement of the intensity of material degradation caused by cavitation.

Based on the determined cavitation velocity values, the resistance to the cavitation effect of the investigated samples can also be assessed. Namely, the cavitation rate for the PM20 sample is $\nu = 0.22$ mg/min, while the obtained value for the PC20 sample is lower: $\nu = 0.14$ mg/min. This means that corundum-based coating is less rapidly deteriorating than mullite-based coating.

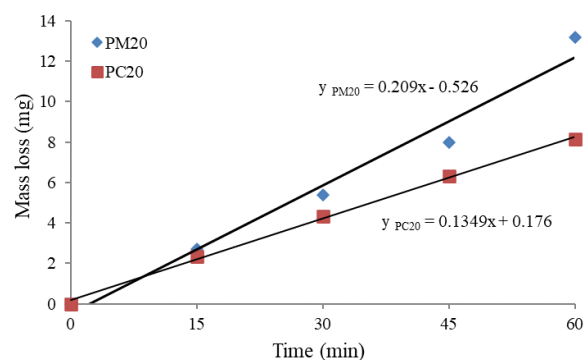


Figure 4. Cavitation erosion rate estimated for refractory coatings PM20 and PC20.

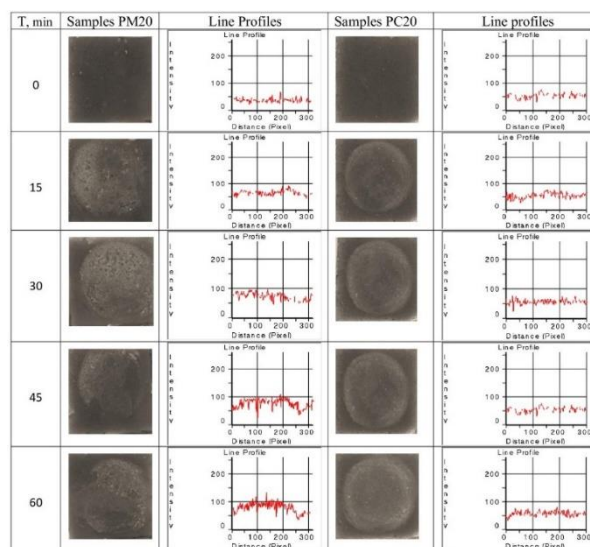


Figure 5. PM20 and PC20 coating samples exposed to a cavitation test with accompanying profile lines.

Figure 5 shows the surfaces of the coating samples during the cavitation erosion test (0–60 minutes) with the corresponding profile lines obtained by image analysis.

The profile lines of the PM20 and PC20 refractory coatings are uniform up to 45 minutes of exposure. Individual peaks, which are present on the profile-line diagram, refer to the presence of singular pits on the

surface of each sample. A certain number of pits were identified on the original PM20 and PC20 samples (before cavitation erosion testing). In the case of the PM20 sample, larger peaks are observed on the profile line for 60 minutes of cavitation in comparison with the corresponding profile line for the PC20 sample. The formation and development of the damage to the surface of the exposed samples took place at a low speed. The results presented in Fig.4 are in agreement with the results provided in Fig.3 a–d.

Figs. 6 and 7 show SEM microphotographs of the characteristic eroded surfaces of the coatings PM20 and PC20 created during testing the effect of cavitation.

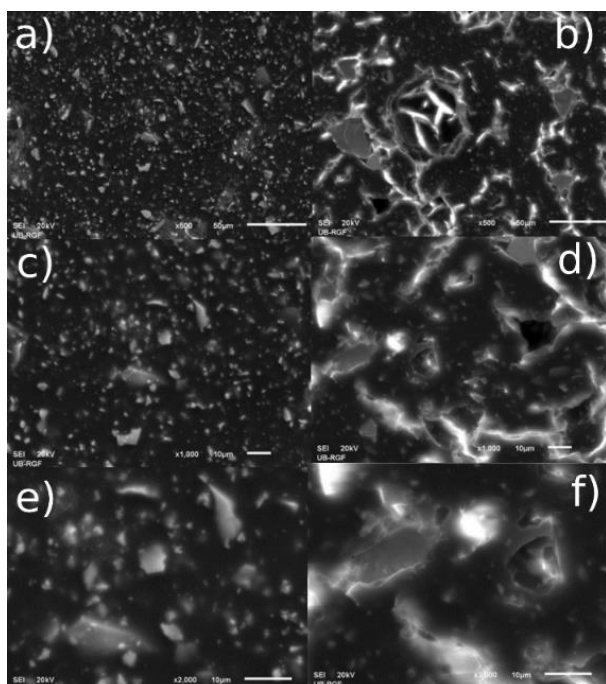


Figure 6. SEM microphotographs of the PM20 coatings: (a), (c), and (e) before cavitation; and (b), (d), and (f) after 60 min of cavitation.

The initial untreated coatings PM20 (Fig. 6) and PC20 (Fig. 7), as seen in the SEM microphotographs on the left side (a, c, and e), show filler particles of various sizes and shapes dispersed uniformly inside the epoxy matrix. The coating applied to the metal substrate is clearly free of defects, bubbles, and delamination. The samples PM20 (Fig. 6) and PC20 (Fig. 7) recorded following the final 60-minute cavitation erosion phase are shown on the right (b, d, and f). The given microphotographs demonstrate that the pits are primarily superficial. There are no void clusters of deeper channels starting from the superficial cavitation pits. The pits appear to be shallow and have smooth surfaces. Thereby, the metal substrate could not be damaged by water stream action due to the presence of the protective coating.

During this research, several potential limitations

occurred. Primarily, there was insufficient sample size for statistical measurements. To make meaningful findings from a study, it is critical to have a large enough sample size. The results are more accurate with a larger sample size. Finding important relationships in the data was challenging because the sample size was too small. To guarantee that the sample is regarded as representative of the community and that the statistical result may be extrapolated to a broader population, statistical tests typically call for a larger sample size. The plan for future research is to repeat the experiment with a larger sample, expand the number of designed coatings, and finally employ a method for analytical modeling (e.g., artificial neural networks) to predict and optimize the behavior and performance of the protective coatings.

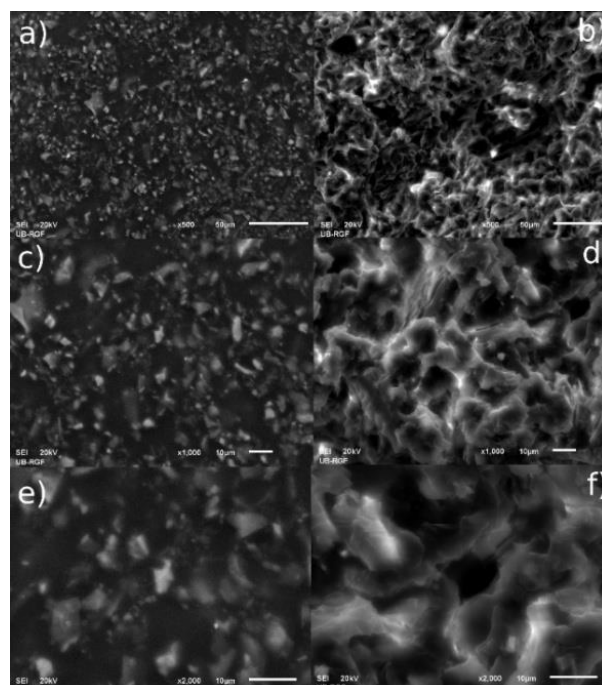


Figure 7. SEM microphotographs of the PC20 coatings: (a), (c), and (e) before cavitation; and (b), (d), and (f) after 60 min of cavitation.

CONCLUSION

In this study, refractory coatings for metal substrates were successfully made and evaluated for cavitation erosion resistance using an inorganic filler of 80 wt.% (pyrophyllite and mullite, i.e., pyrophyllite and corundum) and a siloxane resin of 15% in their mix-design. The key findings are summarized as follows:

The average grain in the filler mixture is sub-rounded to sub-angular, which is suitable for creating homogeneous coatings. The addition of recycled corundum and/or mullite increased the hardness of the

inorganic filler and, thereby, the coating. When applied to a solid surface, the particles of varied grain sizes contribute to the formation of a homogeneous and durable coating layer. The coatings adhered properly to the metal plate, completely covering the surface and leaving no bumps or bubbles. The coating dried quickly in the air and exhibited no delamination or defects.

The monitoring of mass loss during cavitation erosion tests allowed for the assessment of the cavitation rate. The cavitation rates of 0.22 mg/min and 0.14 mg/min for PM20 and PC20 coatings, respectively, suggest that both coatings deteriorated relatively slowly. The corundum-based coating is more resistant to cavitation erosion than the mullite-based coating, probably due to the difference in the filler's Mohs hardness.

The morphology of the PM20 and PC20 coatings during the final 60-minute cavitation erosion phase exhibited mostly superficial pits. There are no vacant clusters of deeper channels starting from the surface cavitation pits. The coating layer protected the metal substrate from damage caused by an intense water stream.

This study demonstrates that the investigated coatings based on pyrophyllite and waste raw materials can be implemented in conditions that involve substantial cavitation loads while still providing adequate protection for the substrate.

ACKNOWLEDGEMENTS

This work was supported by the Ministry of Science, Technological Development and Innovation of the Republic of Serbia (Contracts No.: 451-03-66/2024-03/200213, 451-03-66/2024-03/ 200012 and 451-03-65/2024-03/200135).

REFERENCES

- [1] Global Status Report for Buildings and Construction: <https://www.unep.org/resources/publication/2022-global-status-report-buildings-and-construction> (accessed on 02.02.2024).
- [2] S. Dora, K.M. Mini, J. Energy Storage 72 (2023) 108550. <https://doi.org/10.1016/j.est.2023.108550>.
- [3] A. Liebringshausen, P. Eversmann, A. Göbert, J. Build. Engin. 80 (2023) 107696. <https://doi.org/10.1016/j.jobe.2023.107696>.
- [4] Y. Ettahiri, D. M. Samuel, L. Bouna, A. Khali, A. Aziz, A. Benlhachemi, L. Pérez-Villarejo, W. Kriven, J. Build. Eng. 80 (2023) 108021. <https://doi.org/10.1016/j.jobe.2023.108021>.
- [5] Y. Ettahiri, L.n Bouna, J. Hanna, A. Benlhachemi, H. L. Pilsworth, A. Bouddouch, B. Bakiz, Mater.s Chem. Physics 296 (2023) 127281. <https://doi.org/10.1016/j.matchemphys.2022.127281>.
- [6] A.P. Galvín, S. Sabrina, B. Auxi, A. Peña, A. López-Uceda, J. Environ. Manage. 344 (2023) 118409. <https://doi.org/10.1016/j.jenvman.2023.118409>.
- [7] E. Marsh, J. Orr, T. Ibell, Energy Build. 251 (2021) 111340. <https://doi.org/10.1016/j.enbuild.2021.111340>.
- [8] S. Mohammadnejad, J. Provis, J. van Deventer, Hydrometallurgy 146 (2014) 154–163. <https://doi.org/10.1016/j.hydromet.2014.04.007>.
- [9] R. Wardle, G.W. Brindley, Am. Mineral. 57 (1972) 732–750. (https://ruff.geo.arizona.edu/doclib/am/vol57/AM57_732.pdf, accessed 03.04.2024).
- [10] J. Temuujin, K. Okada, T. Jadambaa, K. MacKenzie, J. Amarsana, J. Eur. Ceram. Soc. 23 (2003) 1277–1282, [https://doi.org/10.1016/S0955-2219\(02\)00297-2](https://doi.org/10.1016/S0955-2219(02)00297-2).
- [11] C. Maqueda, J.L.P. Rodríguez, A. Justo, Analyst 112 (1987) 1085–1086. <https://doi.org/10.1039/AN9871201085>.
- [12] Y. Ettahiri, L. Bouna, A. Brahim, A. Benlhachemi, B. Bakiz, P. Sánchez-Soto, D. Eliche-Quesada, L. Pérez-Villarejo, Appl. Mater. Today 36 (2024) 102048. <https://doi.org/10.1016/j.apmt.2023.102048>.
- [13] K. Zhao, W. Yana, X. Wang, B. Hui, G. Gu, H. Wang, Int. J. Miner. Process. 161 (2017) 78–82. <https://doi.org/10.1016/j.minpro.2017.02.015>.
- [14] X. Pan, Z. Shi, C. Shi, T. Ling, N. Li, Constr. Build. Mater. 132 (2017) 578–5910. <https://doi.org/10.1016/j.conbuildmat.2016.12.025>.
- [15] L. Bouna, A. Ait El Fakir, Y. Ettahiri, H. Abara, A. Jada, K. Draoui, A. Benlhachemi, M. Ezahri, Mater. Chem. Physics 314 (2024) 128858. <https://doi.org/10.1016/j.matchemphys.2023.128858>.
- [16] X. Lu, L. Wang, C. Chen, J. Chen, J. Zhou, J. Deng, Constr. Build. Mater. 400 (2023) 132849. <https://doi.org/10.1016/j.conbuildmat.2023.132849>.
- [17] J.B. Aguiar, C. Júnior, Constr. Build. Mater. 49 (2013) 478–483. <https://doi.org/10.1016/j.conbuildmat.2013.08.058>.
- [18] M. Shariatmadar, P. Gholamhosseini, Z. Abdorrezaee, S. Ghorbanzadeh, S. Feizollahi, F.S. Hosseini, F. Azad Shahraki, M. Mahdavian, Surf. Coat. Technol. (2024) 130501. <https://doi.org/10.1016/j.surfcoat.2024.130501>.
- [19] X. Liu, Prog. Org. Coat. 149 (2020) 105892. <https://doi.org/10.1016/j.porgcoat.2020.105892>.
- [20] H. Qu, M. Feng, M. Li, D. Tian, Y. Zhang, X. Chen, G. Li, Mater. Today Commun. 37 (2023) 107284. <https://doi.org/10.1016/j.mtcomm.2023.107284>.
- [21] S. Gu, H. Shi, J. Li, H. Xu, I. I. Udoh, F. Liu, E. Han, Prog. Org. Coat. 183 (2023) 107789. <https://doi.org/10.1016/j.porgcoat.2023.107789>.
- [22] F. Sun, J. Fu, Y. Peng, X. Jiao, H. Liu, F. Du, Y. Zhang, Prog. Org. Coat. 154 (2021) 106187. <https://doi.org/10.1016/j.porgcoat.2021.106187>.
- [23] S.A.T. Nejad, S. Amanian, E. Alibakhshi, M. Hajisoltani, S.A. Haddadi, M. Arjmand, B. Ramezanzadeh, M. Mahdavian, Prog. Org. Coat. 188 (2024) 108195. <https://doi.org/10.1016/j.porgcoat.2023.108195>.

- [24] W. Merks, Clausthal-Zellerfeld, Germany, (1985). <https://search.worldcat.org/title/607758613>, (accessed on 03.04.202421).
- [25] J. Santamarina, G. Cho, Soil Behavior: The Role of Particle Shape. Conference on Advances in Geotechnical Engineering, London, 29-31 (2004) 604–617. [https://doi.org/10.1061/40659\(2003\)2](https://doi.org/10.1061/40659(2003)2).
- [26] Z. Hossain, I.L. Fabricius, H.F. Christensen, Leading Edge 28 (2009) 86–88. <https://doi.org/10.1190/1.3064151>.
- [27] A. Terzić, D. Radulović, M. Pezo, J. Stojanović, L. Pezo, Z. Radojević, Lj. Andrić, Constr. Build. Mater. 258 (2020) 119721. <https://doi.org/10.1016/j.conbuildmat.2020.119721>.
- [28] M. Pavlović, M. Dojčinović, M. Harbinja, A. Hodić, M. Stojanović, Z. Čeganjac, Z. Aćimović, Struct. Integ. Life 23:3 (2023) 257–260. <http://divk.inovacionicentar.rs/ivk/ivk23/OF2303-5s.html>, (accessed on 03.04.2024.)
- [29] M. Pavlović, M. Dojčinović, M. Harbinja, A. Hodić, D. Radulović, M. Stojanović, Z. Aćimović, in Proceedings of the 54th International October Conference on Mining and Metallurgy (2023) 357–360. https://ioc.tfbor.bg.ac.rs/public/2023/Proceedings_IOC_2023.pdf, (accessed on 03.04.2024).
- [30] M. Pavlović, M. Dojčinović: Kavitaciona oštećenja refrakcionih materijala, Akademska misao, Belgrade, (2020), p.165. ISBN 978-86-7466-823-8. <https://akademska-misao.rs/product/kavitaciona-ostecenja-vatrostalnih-materijala/>. (accessed on 01.03.2024).
- [31] ASTM G32-16 Red Standard Test Method for Cavitation Erosion Using Vibratory Apparatus (Standard + Redline PDF Bundle), <https://webstore.ansi.org/standards/astm/astmg3216red>. (accessed 15.03.2024).
- [32] Jmicro Vision program: <https://jmicrovision.github.io/>. (accessed 15.03.2024).

MARKO PAVLOVIĆ¹
MARINA DOJČINOVIĆ²
JASMINA NIKOLIĆ²
ANJA TERZIĆ³
VLADIMIR PAVIĆEVIĆ²
SAŠA DRMANIĆ²
ENITA KURTANOVIĆ⁴

¹Inovacioni centar Mašinskog fakulteta Univerziteta u Beogradu, Beograd, Srbija

²Tehnološko-metalurški fakultet, Univerziteta u Beogradu, Beograd, Srbija

³Institut za ispitivanje materijala, Beograd, Srbija

⁴AD HARBI, Ilidža/Sarajevo, Bosna i Hercegovina

UTICAJ TEKSTURE I NANOMATERIJALA NA KARAKTERISTIKE PROIZVEDENIH PRIRODNIH VLAKANA

U ovoj studiji pirofilit je prvi put korišćen u sastavu zaštitnih premaza zajedno sa dodatnim otpadnim resursima. Predloženi vatrostalni premazi su primenljivi za metalne i nemetalne konstrukcije, sa mogućnošću upotrebe za zaštitu komponenti mašina u hemijskoj industriji, metalurgiji i rudarstvu. S obzirom na to da pirofilit ima malu tvrdoću, cilj je bio da se poboljša otpornost premaza na kavitacionu eroziju dodavanjem 20 tež. % tvrdih vatrostalnih materijala, odnosno drobljene i mikronizovane opeke na bazi mulita i korunda. Predhodne studije su pokazale da zaštitni premazi sa pirofilitnim puniocem imaju zadovoljavajuću vatrostalnost, ali nedovoljnu otpornost na kavitacionu eroziju. Kao rezultat toga, sastav vatrostalnih premaza, tehnike pripreme i proces proizvodnje premaza su izmenjeni. Ova studija predstavlja jednostavnu metodu kombinovanja konvencionalnih premaza od vatrostalnih punioca (primarni resurs: pirofilit) sa otpadnim sirovinama (opeke na bazi mulita i korunda) koji se koriste kao ojačivači u zaštitnim vatrostalnim premazima za metalne i nemetane elemente konstrukcija koji su visoko otporni na kavitacionu eroziju.

Ključne reči: građevinski maaterijali; otpadni resursi; metalna podloga; mikrostruktura; kvaitaciona erozija.

NAUČNI RAD

NEBOJŠA VASILJEVIĆ^{1,2}
 VLADAN MIČIĆ¹
 MITAR PERUŠIĆ¹
 MARIJA MITROVIĆ¹
 DUŠKO KOSTIĆ¹

¹Faculty of Technology,
 University of East Sarajevo,
 Zvornik, Republic of Srpska,
 Bosnia and Hercegovina

²Faculty of Technology,
 University of Novi Sad, Novi Sad,
 Serbia

SCIENTIFIC PAPER

UDC 634.73:66.061:547.56

OPTIMIZATION OF ULTRASOUND-ASSISTED EXTRACTION OF (POLY)PHENOLIC COMPOUNDS FROM BLUEBERRY (*Vaccinium myrtillus*) LEAVES

Article Highlights

- The degree of correlation (R^2) for all Responses is extremely high
- High temperatures are most effective in extracting anthocyanins
- The extraction of flavonoids is better at medium solid-to-solvent ratios
- The extraction is most effective with a medium amount of ethanol in the solvent

Abstract

The present paper aims to discover the optimal conditions for ultrasound-assisted extraction (UAE) of (poly)phenolic chemicals from blueberry (*Vaccinium myrtillus*) leaves. UAE was performed under the following process conditions: temperature: 25–65 °C, ethanol concentration in the extraction solvent: 30–90 vol.%, and solid-to-solvent ratio: 1:15–1:45 w/v. Statistical analysis was performed using Design-Expert software, using the Box-Behnken design. The study's responses were the content of total (poly)phenols, flavonoids, and anthocyanins in the derived extracts. The results indicated that the corresponding response surface models were highly statistically significant ($p < 0.0001$) and sufficient to describe and predict the content of total (poly)phenols, the content of flavonoids, and the content of anthocyanins with R^2 of 0.965, 0.980 and 0.972, respectively. The optimal conditions for the extraction are for total (poly)phenols 48.4 °C, 51.3 vol.% ethanol, and 1:43.8 w/v solid-to-solvent ratio; flavonoids 58.5 °C, 48.0 vol.% ethanol, and 1:29.8 w/v ratio; and anthocyanins 64.2 °C, 73.5 vol.% ethanol, and 1:44.7 w/v ratio. The use of UAE enhances extraction yields by increasing the release of bioactive compounds, while the application of the Box-Behnken design allows for precise determination of optimal extraction parameters, thereby achieving maximum yields and efficiency.

Keywords: anthocyanins; blueberry; extraction; flavonoids; optimization; (poly)phenols.

Blueberries (*Vaccinium* spp.) are well-known for their excellent taste and nutritious value around the world [1]. Furthermore, research has shown that

blueberry fruits have a variety of bioactive qualities, including antioxidant activity [2], anticancer [3], anti-inflammatory [4], and cardioprotective properties [5]. Anthocyanins, phenolics, and other antioxidants are found in various blueberry species, including *Vaccinium angustifolium*, *Vaccinium ashei* Reade, *Vaccinium corymbosum* L., and *Vaccinium myrtillus* L. [6]. The presence of bioactive substances such as anthocyanins, flavonoids, and phenolic acids may be connected to the above-described pharmacological characteristics [7,8]. Anthocyanins, one type of flavonoid, are antioxidants that are crucial in lowering the risk of certain degenerative illnesses in humans

Correspondence: N. Vasiljevic, Faculty of Technology, University of East Sarajevo, Karakaj 34A, 75400 Zvornik, Republic of Srpska, B&H.

E-mail: nebojsa.vasiljevic@tfzv.ues.rs.ba

Paper received: 7 February, 2024

Paper revised: 1 July, 2024

Paper accepted: 18 July, 2024

<https://doi.org/10.2298/CICEQ240207028V>

[9,10]. Additionally, they can prevent cardiovascular disease and improve vision due to their antioxidant and anti-inflammatory properties [11]. The delicious fruit and abundance of anthocyanins have led to a continual increase in blueberry cultivation worldwide. However, in many countries, the leaves are discarded after pruning and represent agrifood waste. Nonetheless, blueberry leaves can be used for preventive effects against anemia, premature aging, and cataracts [8]. Other studies have suggested that blueberry leaf extracts exhibit remarkable biological activities, including hypolipidemic activity [12], anti-leukemic activity [13], suppression of hepatitis C virus [14], antioxidant activity [15], and antimicrobial activity [16]. Some research on the chemical composition of blueberry leaves (*V. angustifolium*) has indicated richness in chlorogenic acids and quercetin glycosides [17]. In leaves of rabbiteye blueberry (*V. ashei*), flavan-3-ols and proanthocyanidins have been identified as major phenolic components alongside chlorogenic acids and flavonol glycosides [18]. Therefore, the application of phenolic compounds from discarded blueberry leaves is environmentally friendly and contributes to the utilization of beneficial health-promoting compounds. Utilizing blueberry leaves not only reduces waste but also supports the circular economy by valorizing agrifood wastes. With increasing interest in maximizing blueberry plant utilization, more scientists are exploring the extraction potential of (poly)phenolic compounds from blueberry leaves.

Supercritical fluid extraction, ultrasonic-assisted extraction (UAE), enzyme-assisted extraction, and solvent extraction are the main techniques that can be used to extract (poly)phenols from plants [6]. Among these, UAE is an effective, economical, and environmentally friendly approach. The mechanism of UAE is as follows. Phases of compression and rarefaction follow one another when the solvent molecules move longitudinally across an elastic media caused by the ultrasonic wave. The solvent molecules will collide with the surrounding molecules during the compression phase. Negative pressure is applied during the rarefaction phase, which causes the molecules to separate and causes cavitation bubbles to form in the liquid. The dissolved gas will enter the bubble and cause the cavitation bubbles to expand. Hotspots would form when the bubbles collapse, and in an ultrasonic bath at normal temperature, the temperature and pressure might reach up to 5000 K and 5.06×10^5 kPa respectively. The plant matrix's cell walls would be destroyed by the hotspots, releasing chemical compounds into the solvent [19]. For numerous reasons, such as simplicity, low acquisition cost, no specific maintenance requirements, and

availability in most laboratories, UAE has been widely applied in the extraction of bioactive compounds, not only from blueberry fruits [20], but also from blueberry byproducts as pomace [21,22], or leaves [12,23].

Response surface methodology (RSM) has been successfully used recently to examine process optimization [24,25]. Finding the optimal conditions for the process is the primary goal of the RSM. Using statistical design techniques can reduce variation, the amount of time needed for adjustment, and total cost by increasing efficiency and bringing output outcomes closer to nominal values (goals) [26]. The Box-Behnken design (BBD) is a type of rotatory design that focuses on the midpoints of the edges and center points within a cubic region. This strategy helps to avoid extreme experimental conditions and reduces the likelihood of obtaining inaccurate results [27]. BBD is often used for the UAE process due to its efficiency, especially when dealing with three or more variables. It allows for the evaluation of the independent effects or interactions of these variables on the response variable [28].

This study will investigate the influence of various process parameters (temperature, ethanol concentration in the extraction solvent, and the solid-to-solvent ratio) on the ultrasound-assisted extraction (UAE) of (poly)phenols from blueberry leaves (*V. myrtillus*). Using the BBD with the MINITAB 21 software, the paper aims to determine the efficiency of the extraction process based on these parameters.

EXPERIMENTAL

Plant materials and reagents

Dried blueberry leaves, obtained from a local market, were used for extraction (Figure 1). They are known for their darker green to brownish color, with a more brittle texture. Ethanol was used for sample extraction, while extract characterization was performed using the following reagents: Folin-Ciocalteu reagent (Carlo Erba, Germany), sodium carbonate (Lach:ner, Czech Republic), gallic acid (Sigma Aldrich, USA), aluminum chloride (Lach:ner, Czech Republic), sodium hydroxide (Lach:ner, Czech Republic), sodium nitrite (Zorka Šabac, Serbia), catechin hydrate (Sigma Aldrich, USA), acetate buffer pH=4.5 (Lach:ner, Czech Republic) and potassium chloride buffer pH=1.0 (Lach:ner, Czech Republic).

Methods

Determination of total (poly) phenol content is based on oxidation-reduction reactions involving hydroxyl groups of phenol and the Folin-Ciocalteu reagent, as well as polymer complex ions of molybdenum and tungsten. The reaction requires



Figure 1. Dried leaves used of *V. myrtillus*.

a basic environment, which is created by adding sodium carbonate to the reaction mixture. In a test tube, 1.5 ml of working Folin-Ciocalteu solution, 0.2 ml of the sample being tested, and 1.5 ml of sodium carbonate were added. The mixture was left to stand for 30 minutes in the dark at room temperature, and then the absorbance was measured in a 10 mm cuvette at 765 nm, with gallic acid utilized as the standard [29]. A Shimadzu 1800 spectrophotometer (Cole-Parmer, USA) was utilized for spectrophotometric determination, with the calibration curve ranging from 50 to 500 mg/l of gallic acid. The results are given in milligrams of gallic acid equivalent per gram of plant material (mg GAE/g).

The flavonoid content of the sample is determined using the colorimetric technique with aluminum chloride. In an acidic solution, aluminum chloride forms stable complexes with the C-4 keto group or the C-3 and C-5 hydroxyl groups of the present flavones and flavonols, and unstable complexes with ortho-dihydroxyl groups in the A or B ring of flavonoids. In a test tube, 1 ml of the sample being tested and 0.5 ml of 5% sodium nitrite solution were added and left to stand for 5 minutes. Then, 0.5 ml of 10% aluminum chloride was added, and after 6 minutes, 2 ml of 1M NaOH solution was added. The absorbance was measured at 450 nm. The results were expressed as mg of catechin equivalent per milliliter of extract solution. This modified method is described in [30]. For the determination of flavonoids, the calibration curve was in the range of 20 to 200 mg/l of catechin hydrate. The results are given in milligrams of catechin hydrate equivalents per gram of plant material (mg CTH/g).

The quantitative determination of total anthocyanins (non-degraded monomers and products of their degradation) is based on the property of anthocyanins to reversibly change their structure when

the pH of the environment changes, which also changes the absorption spectrum. The content of total anthocyanins is determined by the 'pH differential' method, as described in reference [31]. The procedure for determining anthocyanins is as follows: two test tubes are prepared for each sample. In each test tube, 0.5 ml of the prepared sample is pipetted. Then, 3.5 ml of pH 1.0 buffer is added to one test tube, and 3.5 ml of pH 4.5 buffer is added to the other. After 20 minutes, the absorbance of the reaction solutions is measured at 520 nm and 700 nm. The total anthocyanins concentration in the sample is determined as cyanidin-3-glucoside equivalent (mg Cy3G/g) using the formula [32]:

$$C_{tot} = (A \cdot M \cdot F \cdot 10^3) / \varepsilon \cdot l \cdot R \quad (1)$$

where are: C_{tot} - total anthocyanins content; A - $(A_{520nm} - A_{700nm})_{pH=1.0} - (A_{520nm} - A_{700nm})_{pH=4.5}$; M - molar mass (for Cy3G it is 449,2 g/mol); F - dilution factor; 10^3 - factor for converting grams to milligrams; ε - molar absorption extinction coefficient (for Cy3G it is 26900 Lmol⁻¹ cm⁻¹); l - cuvette thickness (1 cm), and R - factor for recalculating the value of anthocyanins per gram of drug.

A Shimadzu 1800 spectrophotometer was used to determine anthocyanins, the same as it was for total (poly)phenols and flavonoids.

Experimental design and statistical analysis

Experimental design and statistical analysis were performed in Design-Expert 13 software (Stat-Ease Inc, USA) using the RSM.

A BBD, as a form of the RSM, was performed to determine the effect of three experimental factors (temperature, solid-to-solvent ratio, and ethanol concentration in solvent) on the output variables (responses) (Table 1). The extraction time was 30 min and an ultrasonic bath was used for mixing.

Table 1. Coded and actual levels of independent variables used in the RSM design for the process of ultrasonic extraction of blueberry leaves.

Symbol	Independent variables	Levels		
		-1	0	1
A	Temperature [°C]	25	45	65
B	Solid-to-solvent ratio [w/v]	1:15	1:30	1:45
C	The ethanol concentration in the solvent [vol. %]	30	60	90

BBD takes mid-level values of experimental factors, avoiding extreme axial points as in central composite design (CCD) [33]. In this paper, considering the existence of three experimental factors that have three levels, there will be 13 points at the middle level. However, two replicates were performed at the

midpoint of the design to allow estimation of pure error and to calculate the repeatability of the method, resulting in a total of 15 extractions to be performed. To achieve objective results, the experiments were randomized.

The Responses in this study were the content of total (poly)phenols, flavonoids, and anthocyanins in the extract.

The experimental data were fitted to a second-order polynomial model to obtain the regression coefficients. The generalized second-order polynomial model used in the RSM is as follows:

$$Y = a_0 + \sum a_i X_i + \sum a_{ii} X_i^2 + \sum a_{ij} X_i X_j \quad (2)$$

where Y represents the experimental response, a_0 is a constant, a_i , a_{ii} , and a_{ij} are coefficients of linear,

quadratic, and interactive regression models, and X_i and X_j are independent variables in coded values.

Lack of fit, coefficient of determination (R^2), and p -value obtained by analysis of variance (ANOVA) were used to assess the adequacy of the developed model. Regression analysis and Surface plots were generated to explain the effects of independent variables on the response.

RESULTS AND DISCUSSION

According to the BBD with three factors, 15 extractions were performed, and the measured and predicted values of response are shown in Table 2. The table also shows the extraction yield, i.e. the measured response value presented as mass percentage (w/w).

Table 2. Yield, measured and predicted values for the response variables.

Std	Run	Process parameters			Responses								
		Temp [°C]	Solid-to-solvent ratio [w/v]	Ethanol concentration in solvent [vol%]	Total (poly) phenol content			Flavonoid content			Anthocyanin content		
					Measured [mg/g]	Predicted [mg/g]	Yield [%; w/w]	Measured [mg/g]	Predicted [mg/g]	Yield [%; w/w]	Measured [mg/g]	Predicted [mg/g]	Yield [%; w/w]
3	1	25	1:45	60	56.42	57.76	5.64	26.04	25.79	2.60	0.21	0.24	0.021
10	2	45	1:45	30	56.79	53.88	53.8	29.27	29.27	2.93	0.24	0.21	0.024
13	3	45	1:30	60	52.20	50.25	5.22	33.57	36.28	3.36	0.29	0.33	0.029
15	4	45	1:30	60	49.50	50.25	4.95	30.13	36.28	3.01	0.42	0.33	0.042
1	5	25	1:15	60	32.52	30.17	3.52	23.85	23.97	2.39	0.20	0.22	0.020
6	6	65	1:30	30	54.70	55.26	5.47	42.16	42.29	4.22	0.32	0.37	0.032
8	7	65	1:30	90	48.84	47.27	4.88	34.24	33.99	3.42	0.54	0.54	0.054
7	8	25	1:30	90	39.38	38.82	3.94	18.29	18.16	1.83	0.31	0.26	0.031
11	9	45	1:15	90	26.68	29.59	2.67	20.97	20.98	2.10	0.19	0.22	0.019
5	10	25	1:30	30	40.34	41.91	4.03	25.78	26.03	2.58	0.06	0.06	0.006
14	11	45	1:30	60	49.04	50.25	4.90	35.87	36.28	3.59	0.34	0.33	0.034
4	12	65	1:45	60	57.47	59.82	5.75	40.34	40.22	4.03	0.70	0.69	0.070
12	13	45	1:45	90	50.66	49.88	5.07	22.27	22.65	2.23	0.45	0.46	0.045
9	14	45	1:15	30	35.87	36.65	3.59	30.91	30.53	3.06	0.11	0.09	0.011
2	15	65	1:15	60	51.24	49.90	5.12	41.38	41.63	4.14	0.39	0.36	0.039

From Table 2, it can be observed that the highest content of total (poly)phenols (57.47 mg/g) was achieved at a higher temperature (65 °C), a higher solid-to-solvent ratio (1:45 w/v), and an ethanol concentration of 60 vol.%, while the lowest content (26.68 mg/g) was achieved at a temperature of 45 °C, a solid-to-solvent ratio of 1:15 w/v, and an ethanol concentration of 90 vol.%. It can be concluded that higher temperatures and higher solid-to-solvent ratios increase the efficiency of (poly)phenol extraction, while lower (poly)phenol content was obtained at medium temperature values and lower solid-to-solvent ratios, suggesting that these conditions are less efficient for the extraction of total (poly)phenols. The highest flavonoid content (42.16 mg/g) was obtained at higher temperatures (65 °C), the lowest ethanol concentration (30 vol.%), and medium solid-to-solvent ratios (1:30 w/v), while lower flavonoid contents (18.29 mg/g) were obtained at lower temperatures (25 °C), higher ethanol concentrations (90%), and a solid-to-solvent ratio of 1:30 w/v. This may indicate that high ethanol

concentrations and low temperatures are not suitable for flavonoid extraction. Similar to flavonoids, the highest anthocyanin content (0.70 mg/g) was achieved at a temperature of 65 °C, and the lowest content (0.06 mg/g) at low temperatures (25 °C) and low ethanol concentration (30 vol.%). UAE has shown efficiency in extracting bioactive compounds due to its ability to enhance solvent penetration and allow better diffusion of compounds from plant cells. However, comparing the effect of UAE from this study and microwave-assisted extraction (MAE) from the study [34], it can be observed that MAE achieved higher yields of (poly)phenols in shorter extraction periods.

For detailed determination of the influence of process parameters on ultrasound-assisted extraction, ANOVA analysis and evaluation of the obtained models are used.

The experimental data of each measured variable were fitted into a complete quadratic model. Polynomial

coefficients for the surface response model were calculated by multiple regressions. An F -value and a p -value were also calculated for each member of the regression model. Choosing a reliability level of 95%, a p -value greater than 0.05 was not considered statistically significant. The adjusted R^2 and predicted R^2 were evaluated, to determine whether the given

model is adequate after eliminating parameters that do not have a significant impact, i.e., whether the model can accurately predict the responses under different process conditions. ANOVA results for the response surface quadratic model of blueberry leaf extraction are shown in Table 3.

Table 3. ANOVA results for the response surface quadratic model of blueberry leaf extraction.

Source	df	Total (poly) phenol content				Flavonoid content				Anthocyanin content						
		Sum of Squares	Mean Square	F-value	p-value	Sum of Squares	Mean Square	F-value	p-value	Sum of Squares	Mean Square	F-value	p-value			
Model	9	1229.64	136.63	15.46	0.0038	857.36	95.26	26.69	0.0011	0.3694	0.0410	19.27	0.0023			
Temperature (A)	1	237.51	237.51	26.88	0.0035	514.56	514.56	144.15	< 0.001	0.1713	0.1713	80.46	0.0003			
Solid-to-solvent ratio (B)	1	703.69	703.69	79.64	0.0003	0.0820	0.0820	0.0230	0.8854	0.0638	0.0638	29.97	0.0028			
Ethanol concentration(C)	1	61.27	61.27	6.93	0.0463	130.82	130.82	36.65	0.0018	0.0710	0.0710	33.35	0.0022			
AB	1	78.06	78.06	8.83	0.0311	2.61	2.61	0.7307	0.4317	0.0228	0.0228	10.73	0.0221			
AC	1	6.00	6.00	0.6793	0.4473	0.0462	0.0462	0.0129	0.9138	0.0003	0.0003	0.1381	0.7254			
BC	1	2.34	2.34	0.2649	0.6287	2.16	2.16	0.6054	0.4717	0.0045	0.0045	2.13	0.2043			
A ²	1	5.68	5.68	0.6430	0.4590	0.7230	0.7230	0.2025	0.6715	0.0112	0.0112	5.24	0.0707			
B ²	1	15.89	15.89	1.80	0.2376	53.88	53.88	15.09	0.0116	0.0003	0.0003	0.1188	0.7443			
C ²	1	118.79	118.79	13.44	0.0145	161.08	161.08	45.13	0.0011	0.0216	0.0216	10.14	0.0244			
Residual	5	44.18	8.84			17.85	3.57			0.0106	0.0021					
Lack of Fit	3	38.35	12.78	4.39	0.1912	0.6014	0.2005	0.0232	0.9938	0.0084	0.0028	2.44	0.3036			
Pure Error	2	5.83	2.91			17.25	8.62			0.0023	0.0011					
Cor Total	14	1273.82				875.21				0.3801						
			$R^2=0.9653$					$R^2=0.9796$					$R^2=0.9720$			
Fit Statistics			Adjusted $R^2=0.9029$					Adjusted $R^2=0.9447$					Adjusted $R^2=0.9216$			
			Predicted $R^2=0.5080$					Predicted $R^2=0.9429$					Predicted $R^2=0.6343$			
			Adeq Precision=12.4569					Adeq Precision=15.6404					Adeq Precision=16.6827			

The R^2 values for the content of total (poly)phenols, flavonoids, and anthocyanins in the extracts are 0.965, 0.980, and 0.975, respectively. This showed that the response variability was well explained in the generated model, as the models were able to explain 96.5% of the variation in the total (poly)phenol content, 98.0% of the variation in the flavonoid value, and 97.5% of the variation in the anthocyanin content in the extracts. The R^2 value for all three cases is close to 1, which reveals that there is a good correlation between the independent variables and the response. The adjusted R^2 is the corrected value for R^2 after eliminating terms in the model that do not have a significant effect on the responses. The values of the content of total (poly)phenols, flavonoids, and anthocyanins in the extracts are 0.903, 0.943, and 0.922, respectively. These values are very close to the R^2 values, which means that the proposed models can very easily explain the different variations even by eliminating members whose p -values are greater than 0.05.

Predicted R^2 is used to determine how well a regression model makes predictions. The values for predicted R^2 for the content of total (poly)phenols, flavonoids, and anthocyanins in the extracts are 0.508, 0.945, and 0.634, respectively. The predicted R^2 for total (poly)phenol content (0.508) and anthocyanin content (0.634) is not close to the adjusted R^2 (for total (poly)phenols it is 0.903 and 0.922 for anthocyanins) as expected; that is, the difference is greater than 0.2. This

may indicate that the model fits the original data, but the predictions are not accurate enough. This indicates that the model is complicated and begins to model noise in the data (a condition known as 'overfitting the model') [35]. The difference between adjusted R^2 (0.945) and predicted R^2 (0.943) for the content of flavonoids in the extract is extremely small, which means that the obtained model provides valid predictions for the new observations.

Adeq Precision represents the signal-to-noise ratio. Its values for the content of total (poly)phenols, flavonoids, and anthocyanins in extracts are 12.5, 15.6, and 16.7, respectively. The values for all three responses are over 4, which indicates that the signal is adequate.

Lack of fit can be used to confirm the validity of the model. By ANOVA analysis for lack of fit values of all responses, it was determined that the p -value is significantly higher than 0.05, which indicates that the models are adequately adapted to the experimental data.

Influence of process parameters on the value of total (poly) phenol content in the extract

Table 4 shows coded and uncoded coefficients of the regression equation and p -values for members in the proposed quadratic model for the content of total (poly)phenols in blueberry leaf extracts.

ANOVA analysis revealed that the content of total

Table 4. Regression coefficients and *p*-values for all Responses.

Variables	Total (poly) phenol content			Flavonoid content			Anthocyanin content		
	Coded Regression coefficients	Actual Regression coefficients	<i>p</i> -value	Coded Regression coefficients	Actual Regression coefficients	<i>p</i> -value	Coded Regression coefficients	Actual Regression coefficients	<i>p</i> -value
Constant	+50.25	-22.27383	<0.0001	+36.28	-14.51734	<0.0001	+0.3291	+0.008202	<0.0001
Temperature (A)	+5.45	+0.557594	0.0035	+8.02	+0.392937	<0.0001	+0.1463	-0.011751	0.0003
Solid-to-solvent ratio (B)	+9.38	+1.73910	0.0003	+0.1012	+1.04854	0.8854	+0.0893	-0.007663	0.0028
Ethanol concentration (C)	-2.77	+0.704903	0.0463	-4.04	+0.704938	0.0018	+0.0942	+0.011736	0.0022
AB	-4.42	-0.014725	0.0311	-0.8075	-0.002692	0.4317	+0.0756	+0.000252	0.0221
AC	-1.22	-0.002042	0.4473	-0.1075	-0.000179	0.9138	-0.0086	-0.000014	0.7254
BC	+0.7650	+0.001700	0.6287	+0.7350	+0.001633	0.4717	+0.0337	+0.000075	0.2043
AA	+1.24	+0.003101	0.4590	+0.4425	+0.001106	0.6715	+0.0550	+0.000137	0.0707
BB	-2.07	-0.009220	0.2376	-3.82	-0.016978	0.0116	-0.0083	-0.000037	0.7443
CC	-5.67	-0.006302	0.0145	-6.60	-0.007339	0.0011	-0.0765	-0.000085	0.0244

(poly)phenols in the extract is strongly influenced by the following parameters ($p < 0.05$): temperature (A), solid-to-solvent ratio (B), ethanol concentration in the solvent (C), the interaction of temperature and the solid-to-solvent ratio (AB) and the square of the ethanol concentration in the solvent (CC).

By discarding members that do not have a large impact, the regression equation for the content of total (poly)phenols in the extract has the following form:

$$Y = -22.27383 + 0.55759 \cdot A + 1.73910 \cdot B + 0.70490 \cdot C - 0.01473 \cdot AB - 0.0063 \cdot CC \quad (3)$$

To assess the influence of input parameters on the content of total (poly)phenols in the extract, surface plots were constructed, as shown in Figure 2.

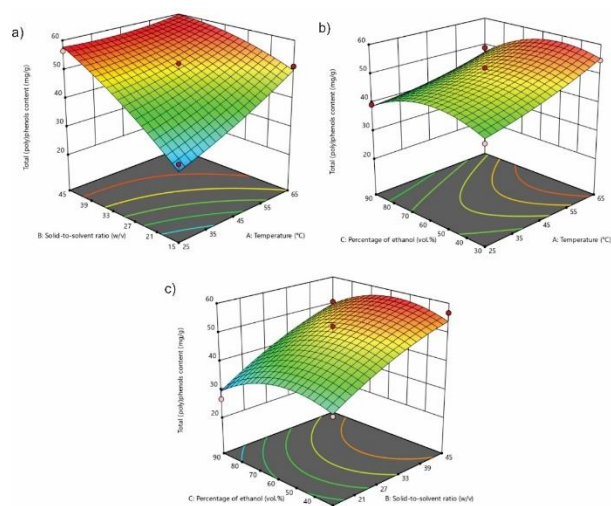


Figure 2. Surface plots for the content of total (poly)phenols in the extracts in the interaction of (a) solid-to-solvent ratio and temperature, (b) ethanol concentration in the solvent and temperature, and (c) ethanol concentration in the solvent and solid-to-solvent ratio.

Figure 2a shows the influence of the solid-to-solvent ratio (B) and temperature (A) on the value of the total (poly)phenols content in the extracts based on the mean level (0) of the ethanol concentration in the solvent (C). It was observed that the value of the

response increases linearly with the increase in the solid-to-solvent ratio (B) and temperature (A). The lowest value of the Response (<35 mg GAE/g) is achieved in the range of the solid-to-solvent ratio of 1:15–1:20 w/v and temperature of 25–35 °C, while the highest values of the Response (>55 mg GAE/g) are achieved in over the entire range of the solid-to-solvent ratio of 1:40–1:45 w/v independent of temperature. Bai *et al.* found that a higher solid-to-solvent ratio improved the extraction yield of phenolic compounds from plant materials using UAE [36]. Similar to our findings, they observed a linear increase in the extraction efficiency with an increase in the solid-to-solvent ratio. Chemat *et al.* highlighted that the solid-to-solvent ratio is a critical parameter in the UAE, influencing the mass transfer and solubility of phenolic compounds [37]. Their findings support our results, emphasizing the importance of optimizing this ratio to achieve maximum extraction efficiency.

Figure 2b shows the influence of the ethanol concentration in the solvent (C) and temperature (A) on the value of the total (poly)phenols content in the extracts at the mean value of the solid-to-solvent (B) ratio. It is observed that low and high ethanol concentration in the solvent leads to a slightly lower value of the Response, than when ethanol with medium values (45–65 vol.%) is used. Herrero *et al.* reported that both very low and very high ethanol concentrations can reduce extraction efficiency. Low ethanol content may not sufficiently disrupt cell walls, while high ethanol content can reduce solvent polarity, hindering the extraction of polar phenolic compounds [38]. This aligns with our results showing lower extraction efficiency at low (<35 vol.%) and high (80–90 vol.%) ethanol concentrations. Observing the interaction of parameters A and C, it is observed that Response values of 40–45 mg GAE/g are achieved at lower temperatures (25–40 °C) in the entire range of ethanol concentration in the solvent (C). By raising the temperature, there is an increase in the value of the Response (>55 mg GAE/g), where this increase is more pronounced at the ethanol concentration of

30–65 vol.% than at the ethanol concentration of 65–90 vol.%. Chemat *et al.* found that moderate temperatures (around 50–60°C) optimize UAE efficiency by increasing solvent penetration and compound solubility without degrading sensitive phenolic compounds [37]. This is consistent with our findings of optimal extraction at increased temperatures.

From Figure 2c, it can be seen that the high content of ethanol in the solvent (80–90 vol.%) and the low solid-to-solvent ratio (1:15–1:20 w/v) have an extremely unfavorable effect on the extraction of total (poly)phenols from blueberry leaves. Also, at the same solid-to-solvent ratio and ethanol concentration in solvent lower than 35 vol.%, the extraction of total (poly)phenols is unfavorable (<35 mg GAE/g). With an increase in the solid-to-solvent ratio, there is a linear increase in the value of the Response, whereby this increase is more pronounced with the use of ethanol concentration of 30–65 vol.%.

Influence of process parameters on the value of flavonoid content in the extract

ANOVA analysis for the content of flavonoids in blueberry leaf extracts (Table 4) revealed that the following parameters have a great influence ($p < 0.05$) on the extraction of flavonoids from blueberry leaves: linear terms - temperature (A) and ethanol concentration in the solvent (C), and quadratic terms - the solid-to-solvent ratio (BB) and ethanol concentration in solvent (CC). The abbreviated regression equation for the content of flavonoids in the extract has the following form:

$$Y = -14.51734 + 0.39293 \cdot A + 0.70493 \cdot C - 0.01697 \cdot BB - 0.00733 \cdot CC \quad (4)$$

Figure 3 shows Surface plots for flavonoid content in the extract.

Figure 3a shows the influence of the solid-to-solvent ratio (B) and temperature (A) on the value of the flavonoid content in the extracts based on the mean level (0) of the ethanol concentration in the solvent (C). At lower temperatures (25–30 °C), at very low solid-to-solvent ratios (1:15–1:20 w/v) on the one hand, and very high solid-to-solvent ratios (1:40–1:45 w/v) on the other hand, work unfavorably for the extraction of flavonoids, and under these conditions <25 mg CTH/g of flavonoids is extracted. This aligns with Bai *et al.*, who found that an optimal solid-to-solvent ratio is crucial for maximizing extraction efficiency due to its impact on mass transfer dynamics [36]. From the plot, it can be seen that the parameter of solid-to-solvent ratio (B) has no great influence on the Response, which

graphically confirmed the results of the ANOVA analysis; on the other hand, the plot shows a great influence of temperature, i.e. with the increase of that parameter there is a marked increase in the content of flavonoids in the extract. The highest content of flavonoids (>40 mg CTH/g) is achieved at temperatures higher than 55 °C, at any solid-to-solvent ratio. This observation is consistent with Chemat *et al.*, who reported enhanced extraction efficiency at higher temperatures (55–65°C), attributed to improved solvent penetration and enhanced solubility of flavonoids [37].

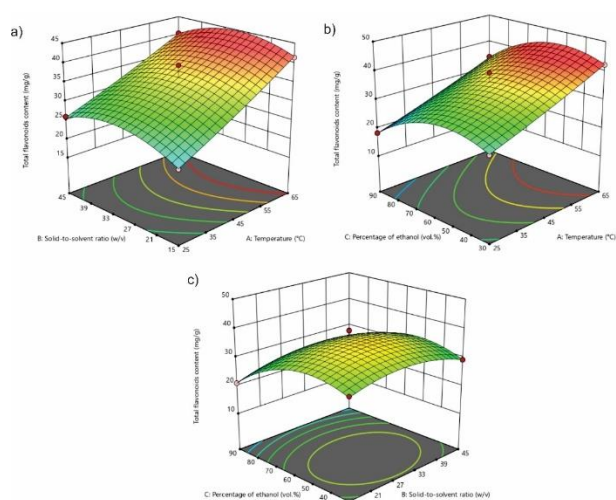


Figure 3. Surface plots for the content of flavonoids in the extracts with mutual interaction: (a) the solid-to-solvent ratio and temperature, (b) ethanol concentration in the solvent and temperature, and (c) ethanol concentration in the solvent and the solid-to-solvent ratio.

Figure 3b shows that both the ethanol concentration in the solvent (C) and the temperature (A) have a significant effect on the ultrasound-assisted extraction of flavonoids from blueberry leaves. The use of a solvent containing 80–90% ethanol is unfavorable for the extraction of flavonoids. This finding mirrors Herrero *et al.*, who noted reduced extraction efficiency at very high ethanol concentrations due to solvent polarity effects and inadequate disruption of cell walls [38]. This influence is particularly clear during extraction at lower temperatures (25–35 °C) because <20 mg CTH/g flavonoids are extracted. Contrary to those process conditions, with ethanol concentration in the solvent in the interval 30–60 vol.% and temperatures 55–65 °C, there is the most intensive extraction of flavonoids (>40 mg CTH/g).

Observing the influence of the ethanol concentration in the solvent (C) and the solid-to-solvent ratio (B), Figure 3c, it is noticed that a plateau is reached at certain values. The maximum value of flavonoids in the extract (>35 mg CTH/g) is achieved when the ethanol concentration in the solvent is in the

range of 35–65% and the solid-to-solvent ratio is in the range of 1:20–1:35 w/v. Moving away from that range, the flavonoid content in the extract decreases, which is particularly clear with an increase in the ethanol concentration up to 90%. This corroborates with findings by various authors emphasizing the critical role of balanced ethanol concentration and solid-to-solvent ratio for maximizing bioactive compound extraction efficiency [37].

Influence of process parameters on anthocyanin content value in the extract

ANOVA analysis (Table 4) revealed that the extraction of anthocyanins from blueberry leaves is influenced by the following factors: temperature (A), solid-to-solvent ratio (B), and ethanol concentration in the solvent (C), square of temperature (AA) and square of ethanol concentration in the solvent (CC). By eliminating factors that have no influence, the regression equation for anthocyanin content in the extract takes the form:

$$Y = 0.0082 - 0.01175 \cdot A - 0.00766 \cdot B + 0.01173 \cdot C + 0.00013 \cdot AA - 0.000085 \cdot CC \quad (5)$$

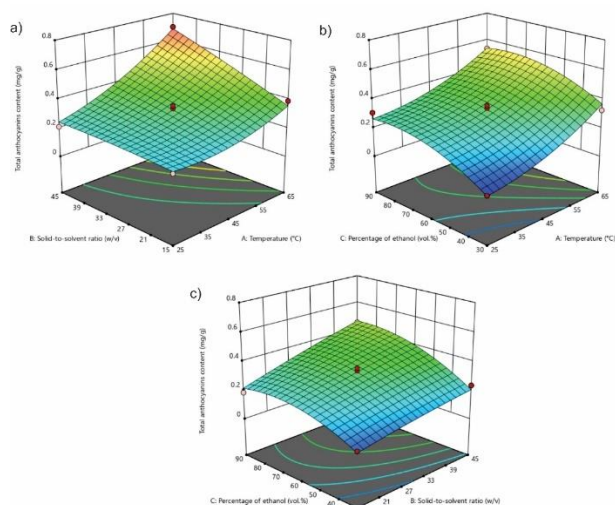


Figure 4. Surface plots for the content of anthocyanins in the extracts with mutual interaction: (a) solid-to-solvent ratio and temperature, (b) ethanol concentration in the solvent and temperature, and (c) ethanol concentration in the solvent and the solid-to-solvent ratio.

From Figure 4a (influence of the solid-to-solvent ratio (B) and temperature (A)), it can be seen that the extraction of anthocyanins is favored by an extremely narrow range of process parameter values. First of all, it is observed that only at high temperatures (60–65 °C) and high solid-to-solvent ratios (1:40–1:45 w/v) can the maximum yield of anthocyanins in the extract be achieved (>0.6 mg Cy3G/g). In contrast, by comparing Figure 4b and Figure 4c, it can be seen that the

extraction of anthocyanins is poorly efficient at the following process conditions: ethanol concentration in the solvent of 30–50 vol.%, temperature of 25–50 °C and the solid-to-solvent ratio of 1:15–1:25 w/v. High solid-to-solvent ratios and high temperatures significantly improve extraction efficiency, while moderate ethanol concentrations are less effective. These findings are consistent with established literature, underscoring the importance of precise parameter optimization for maximizing anthocyanin yields using UAE techniques [39,40].

Optimization

Figure 5 shows the optimization plot for the content of total (poly)phenols in the extract. The maximum content of (poly)phenol in the extract is taken as a target, which is why there is only one solution. The optimal process parameters are temperature 48.4 °C, solid-to-solvent ratio 1:43.8 w/v, and ethanol concentration in the solvent 51.3 vol.%, whereby the value of Response is 57.5 mg GAE/g. The composite desirability is equal to one, indicating that the setting provided the most favorable results.

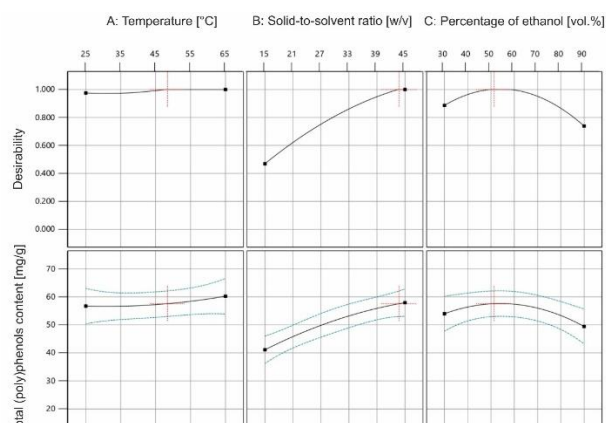


Figure 5. Optimization plot for total (poly)phenols content in the extract.

The optimization plot for the content of flavonoids in the extract is shown in Figure 6. Temperature 58.5 °C, solid-to-solvent ratio of 1:29.8 w/v, and ethanol concentration in the solvent 48.0 vol.% are the optimal process parameters for the extraction of the maximum content of flavonoids (44.38 mg CTH/g). As in the case of optimization of total (poly)phenols, the composite desirability is equal to unity.

Finally, optimization of process conditions for ultrasound-assisted extraction (UAE) of anthocyanins from blueberry leaves was carried out (Figure 7). As in the previous two optimizations, the aim is to maximize Response and composite desirability. The optimal process conditions are temperature 64.2 °C, solid-to-solvent ratio 1:44.7 w/v, and ethanol concentration in

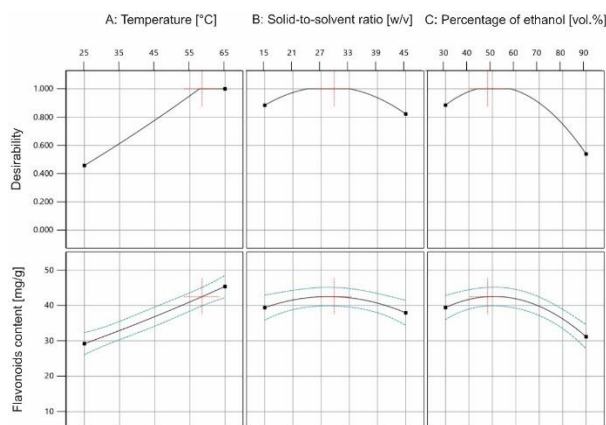


Figure 6. Optimization plot for flavonoid content in extract.

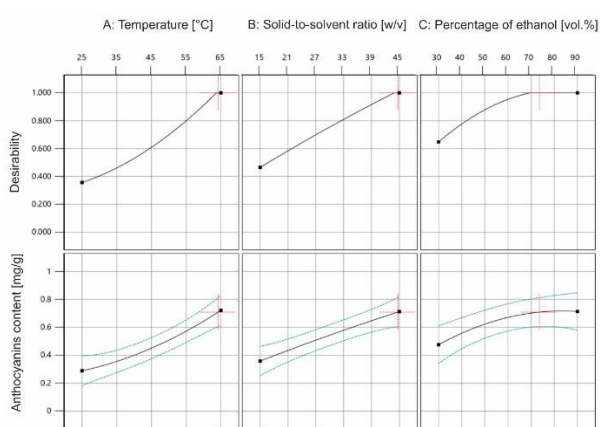


Figure 7. Optimization plot for anthocyanins content in extract.

the solvent 73.5 vol.%. Under these conditions, 0.71 mg Cy3G/g of anthocyanin is extracted.

When the temperature is considered as a process parameter, it is noticeable that temperatures lower than 45 °C are not favorable for extraction. First of all, the viscosity of the solvent at lower temperatures is higher, and the solubility of the dissolved substance and the diffusion coefficient are lower, which adversely affects the extraction process [41]. On the other hand, by analyzing the optimal time for all three Responses, it is noticeable that high temperatures do not have a favorable effect on the extraction of (poly)phenolic compounds. The reason for such a phenomenon lies in the fact that phenolic compounds are thermosensitive, i.e. their thermal decomposition occurs at high temperatures [41,42]. In this work, the optimal temperature for the extraction of total (poly)phenols is lower (48.4 °C) compared to the extraction of anthocyanins (64.2 °C), which means that anthocyanins from blueberry leaves are more resistant to higher temperatures than other phenolic compounds (phenolic acids, stilbenes, tannins, flavonoids, etc.).

When total (poly)phenols and anthocyanins are examined, it is evident that the highest degree of extraction is obtained at close to the highest solid-to-

solvent ratio (1:43.8–1:44.7 w/v). This could be due to the increased contact area between the sample and the solvent, allowing for more effective mass transfer of the (poly)phenolic compounds from the solid matrix to the liquid phase. A higher ratio may result in faster mass transfer, which may result in higher yields due to the amount of solvent available to dissolve the (poly)phenolic compound. Higher solvent content in an extraction system often improves extraction efficiency because more solid material is available for interaction with the solvent [43]. On the other hand, the maximum content of flavonoids is extracted at a solid-to-solvent ratio of 1:29.8 w/v. The most likely explanation for this phenomenon is that a very high solid-to-liquid ratio may cause contaminants to dissolve, reducing the solubility of flavonoids [44].

The extraction of total (poly)phenols and flavonoids has a positive effect on the medium values of the ethanol concentration in the solvent (51.3 vol.% and 48.0 vol.%, respectively), while for the extraction of anthocyanins, the optimal ethanol concentration in the solvent is higher and amounts to 73.5 vol.%. Lower concentrations of ethanol penetrate plant cells more easily, making phenolic extraction easier. Ethanol at greater concentrations can cause protein denaturation, impede phenolic breakdown from the matrix, and diminish the production of (poly)phenolic compounds [45]. The combination of water and ethanol allows efficient (poly)phenol extraction because water acts as a swelling agent and ethanol breaks down the bonds between the solutes and the floral matrix; therefore, high ethanol concentration in solvent yields a smaller yield of (poly)phenolic compounds [46].

In comparison with the full factorial design used in previous research [32], the BBD offers several significant advantages. The BBD is more efficient in investigating quadratic effects and interactions between factors, as it better covers the area of interest without the need for extreme values of the factors. This results in more robust models that can provide more precise estimates of optimal conditions for the processes being studied. Also, The BBD allows for more efficient experimental planning, reducing redundancy and potential errors in conducting experiments. In this way, the obtained results are more reliable and can be better applied in practice.

CONCLUSION

The experimental data fit well into the obtained models, as confirmed by the high degrees of correlation (R^2 and adjusted R^2). The model accurately predicts flavonoid content, but not total (poly)phenols and

anthocyanins. Extraction is adversely affected by low temperatures due to slow diffusion and high temperatures due to the thermosensitivity of phenolic compounds. Anthocyanins can be extracted at slightly higher temperatures owing to their greater heat resistance. Total (poly)phenols and anthocyanins are better extracted at higher solid-to-solvent ratios due to a larger concentration gradient. However, flavonoids are better extracted at lower ratios to avoid components that reduce their solubility. Medium ethanol concentrations are optimal for phenolic compound extraction, as ethanol penetrates plant material effectively, while higher concentrations denature proteins and hinder extraction. The optimization of process parameters using the BBD demonstrated that UAE effectively enhances the release of bioactive compounds, achieving maximum yields under specified conditions as follows: for (poly)phenols, 48.4 °C, 51.3 vol.% ethanol, and 1:43.8 w/v solid-to-solvent ratio; flavonoids, 58.5 °C, 48.0 vol.% ethanol, and 1:29.8 w/v ratio; and anthocyanins, 64.2 °C, 73.5 vol.% ethanol, and 1:44.7 w/v ratio. The bioactive components have potential applications in functional foods, nutraceuticals, pharmaceuticals, and cosmetics, and further research could expand their use.

REFERENCES

- [1] W. Chu, H. Gao, S. Cao, X. Fang, H. Chen, S. Xiao, *Food Chem.* 219 (2017) 436–442. <https://doi.org/10.1016/j.foodchem.2016.09.186>.
- [2] M. Morita, Y. Naito, E. Niki, T. Yoshikawa, J. *Berry Res.* 7 (2017) 1–9. <https://doi.org/10.1016/j.foodchem.2017.05.157>.
- [3] B.S. Luo, R.H. Gu, E. Kennelly, C.L. Long, *Curr. Med. Chem.* 25 (2017) 5168–5176. <https://doi.org/10.2174/0929867324666171003122502>.
- [4] M. Grace, J. Xiong, D. Esposito, M. Ehlenfeldt, M. Lila, *Food Chem.* 277 (2019) 336–346. <https://doi.org/10.1016/j.foodchem.2018.10.101>.
- [5] R. Eladwy, E. Mantawy, W. El-Bakly, M. Fares, L. Ramadan, S. Azab, *Phytomedicine* 51 (2018) 84–93. <https://doi.org/10.1016/j.phymed.2018.10.009>.
- [6] J. Paes, R. Dotta, G. Barbero, J. Martinez, J. *Supercrit. Fluids* 95 (2014) 8–14. <https://doi.org/10.1016/j.supflu.2014.07.025>.
- [7] D. Li, B. Li, Y. Ma, X. Sun, Y. Lin, X. Meng, J. *Food Compos. Anal.* 62 (2017) 84–93. <https://doi.org/10.1016/j.jfca.2017.03.006>.
- [8] N. Seeram, L. Adams, Y. Zhang, R. Lee, D. Sand, H. Scheuller, D. Heber, J. *Agric. Food Chem.* 54 (2006) 3929–3939. <https://doi.org/10.1021/jf061750g>.
- [9] H. Wang, G. Cao, R. Prior, J. *Agric. Food Chem.* 45 (1997) 304–309. <https://doi.org/10.1021/jf960421t>.
- [10] W. Kalt, C. Forney, A. Martin, R. Prior, J. *Agric. Food Chem.* 47 (1999) 4638–4644. <https://doi.org/10.1021/jf990266t>.
- [11] W. Yang, Y. Guo, M. Liu, X. Chen, X. Xiao, S. Wang, P. Gong, Y. Ma, F. Chen, J. *Funct. Foods* 88 (2022) 104864. <https://doi.org/10.1016/j.jff.2021.104864>.
- [12] Y. Li, B. Li, L. Geng, *Eur. Food Res. Technol.* 233 (2011) 897–903. <https://doi.org/10.1007/s00217-011-1572-z>.
- [13] K. Skupien, J. Oszmianski, D. Kostrzewa-Nowak, J. Tarasiuk, *Cancer Lett.* 236 (2006) 282–291. <https://doi.org/10.1016/j.canlet.2005.05.018>.
- [14] S. Nakama, C. Ishikawa, S. Nakachi, N. Mori, *Int. J. Oncol.* 38 (2011) 1163–1173. <https://doi.org/10.3892/ijo.2011.939>.
- [15] M. Ehlenfeldt, R. Prior, J. *Agric. Food Chem.*, 49 (2001) 2222–2227. <https://doi.org/10.1021/jf0013656>.
- [16] M. Gurjar, S. Ali, M. Akhtar, K. Singh, *Agric. Sci.* 3 (2012) 425–433. <https://doi.org/10.4236/as.2012.33050>.
- [17] C. Harris, A. Burt, A. Saleem, P. Mai Le, L. Martineau, P. Haddad, S. Bennet, J. *Arnason, PCA* 18 (2007) 161–169. <https://doi.org/10.1002/pca.970>.
- [18] Y. Matsuo, Y. Fujita, S. Ohnishi, T. Tanaka, H. Hirabaru, T. Kai, H. Sakaida, S. Nishizono, I. Kouno, *Food Chem.* 121 (2010) 1073–1079. <https://doi.org/10.1016/j.foodchem.2010.01.052>.
- [19] T. Wang, N. Guo, S. Wang, P. Kou, C. Zhao, Y. Fu, *Food Bioprod. Process.* 108 (2018) 69–80. <https://doi.org/10.1016/j.fbp.2018.01.003>.
- [20] J. Rocha, F. Procopio, A. Mendonca, L. Vieira, I. Perrone, F. Barros, P. Stringheta, *JFST* 38 (2018) 45–53. <https://doi.org/10.1590/1678-457X.36316>.
- [21] J. Xie, M. Chen, T. Ren, Q. Zheng, *Environ. Technol. Innov.* 31 (2023) 103147. <https://doi.org/10.1016/j.eti.2023.103147>.
- [22] X. Zhang, S. Wang, Q. Wu, Q. Wu, M. Battino, F. Giamperi, W. Bai, L. Tian, *Food Chem. X* 16 (2022) 100476. <https://doi.org/10.1016/j.fochx.2022.100476>.
- [23] M. Santos-Martin, J. Cubero-Cardoso, R. González-Domínguez, R. Cortés-Triviño, A. Sayago, J. Urbano, A. Fernández-Recamales, *Biomass Bioenergy* 175 (2023) 106882. <https://doi.org/10.1016/j.biombioe.2023.106882>.
- [24] T. Hu, Y. Guo, Q. Zhou, X. Zhong, L. Zhu, J. Piao, J. Chen, J. Jiang, J. *Food Sci.* 77 (2012) 975–982. <https://doi.org/10.1111/j.1750-3841.2012.02869.x>.
- [25] A. Andres, M. Petron, A. Lopez, M. Timon, *Foods* 9 (2020) 1398. <https://doi.org/10.3390/foods9101398>.
- [26] J. Salar, S. Purewal, M. Bhatti, *Resour.-Effic. Technol.* 2 (2016) 148–157. <https://doi.org/10.1016/j.refit.2016.08.002>.
- [27] M. Santos-Martin, J. Cubero-Cardoso, R. González-Domínguez, R. Cortés-Triviño, A. Sayago, J. Urbano, A. Fernández-Recamales, *Biomass Bioenergy* 175 (2023) 106882. <https://doi.org/10.1016/j.biombioe.2023.106882>.
- [28] O. Soufi, L. Medouni-Haroune, M. Bachirbey, S. Medouni-Adrar, F. Idir, T. Heddad, L. Ouldsaadi, C. Romero, K. Madani, L. Makhoulouf-Boulekbatche, *Sustain. Chem. Pharm.* 36 (2023) 101260. <https://doi.org/10.1016/j.scp.2023.101260>.
- [29] International Organization for Standardization, "ISO 14502-1:2005 Determination of substances characteristic of green, black tea – Part 1: Content of total polyphenols

- in tea – Colorimetric method using Folin-Ciocalteu reagent" 2005.
- [30] P. Smolinski-Savi, L. Dos Santos, A. Goncalves, S. Biesek, C. Lima, *Demetra* 12 (2017) 275–288. <https://doi.org/10.12957/demetra.2017.22391>.
- [31] M. Giusti, R. Wrolstad, in *Current Protocols in Food Analytical Chemistry*, John Wiley & Sons, New York (2001) F1.2.1-F1.2.13. <https://doi.org/10.1002/0471142913.faf0102s00>.
- [32] N. Vasiljević, V. Mičić, M. Perušić, M. Tomić, S. Panić, D. Kostić, *OUAC*, 35 (2024) 27–35. <https://doi.org/10.2478/auoc-2024-0004>.
- [33] L. Sedaghat Boroujeni, M. Ghavami, Z. Piravi Vanak, A. Ghasemi Pirbalouti, *Food Sci. Technol.* 40 (2020) 322–330. <https://doi.org/10.1590/fst.10919>.
- [34] W. Routray, V. Orsat, *Ind. Crops. Prod.* 58 (2014) 36–45. <https://doi.org/10.1016/j.indcrop.2014.03.038>.
- [35] X. Ying, *J. Phys. Conf. Ser.* 1168 (2019) 022022. <https://doi.org/10.1088/1742-6596/1168/2/022022>.
- [36] X. Bai, L. Zhou, S. Cang, Y. Liu, J. Liu, X. Feng, R. Fan, *Molecules* 28 (2023) 3610. <https://doi.org/10.3390/molecules28083610>.
- [37] F. Chemat, M. Abert-Vian, A. Fabiao-Tixier, J. Strube, L. Uhlenbrock, V. Gunjevic, G. Cravotto, *TrAC, Trends Anal. Chem.* 118 (2019) 248–263. <https://doi.org/10.1016/j.trac.2019.05.037>.
- [38] M. Herrero, M. Plaza, A. Cifuentes, E. Ibenez, *J. Chromatogr. A* 1217 (2010) 2512–2520. <https://doi.org/10.1016/j.chroma.2009.11.032>.
- [39] J. Yuan, H. Li, W. Tao, Q. Han, H. Dong, J. Zhang, Y. Jing, Y. Wang, Q. Xiong, T. Xu, *Ultrason. Sonochem.* 68 (2020) 105192. <https://doi.org/10.1016/j.ultsonch.2020.105192>.
- [40] X. Zheng, X. Xu, C. Liu, Y. Sun, Z. Lin, H. Liu, *Sep. Purif. Technol.* 104 (2013) 17–25. <https://doi.org/10.1016/j.seppur.2012.11.011>.
- [41] G. Spigno, L. Tramelli, D. De Faveri, *J. Food Eng.* 81 (2007) 200–208. <https://doi.org/10.1016/j.jfoodeng.2006.10.021>.
- [42] V. Biasi, E. Huber, P. Barreto, *Food Technol.* 57 (2022) 100789. <https://doi.org/10.1590/S1678-3921.pab2022.v57.02537>.
- [43] S. Sai-Ut, P. Kingwascharapong, M.R. Mazumder, *J. Agric. Food Res.* 14 (2023) 100888. <https://doi.org/10.1016/j.jafr.2023.100888>.
- [44] H. Liu, H. Wu, Y. Wang, F. Wang, X. Liu, J. Zhou, *Appl. Biol. Chem.* 64 (2021) 64–78. <https://doi.org/10.1186/s13765-021-00649-8>.
- [45] Y. Yang, J. Li, Y. Zu, Y. Fu, M. Luo, N. Wu, X. Liu, *Food Chem.* 122 (2010) 373–380. <https://doi.org/10.1016/j.foodchem.2010.02.061>.
- [46] K. Gunathilake, K. Ranaweera, H. Rupasinghe, *Food Sci. Nutr.* 7 (2019) 528–536. <https://doi.org/10.1002/fsn3.832>.

NEBOJŠA VASILJEVIĆ^{1,2}
VLADAN MIČIĆ¹
MITAR PERUŠIĆ¹
MARIJA MITROVIĆ¹
DUŠKO KOSTIĆ¹

¹Tehnološki fakultet,
Univerzitet u Istočnom Sarajevu,
Zvornik, Republika Srpska,
Bosna i Hercegovina

²Tehnološki fakultet,
Univerzitet u Novom Sadu, Novi
Sad, Srbija

NAUČNI RAD

OPTIMIZACIJA ULTRAZVUČNE EKSTRAKCIJE (POLI)FENOLNIH JEDINJENJA IZ LIŠĆA BOROVNICE (*Vaccinium myrtillus*)

Cilj rada je da utvrdi optimalne uslove za ultrazvučnu ekstrakciju (UAE) (poli)fenolnih jedinjenja iz lišća borovnice (Vaccinium myrtillus). UAE je izvedena pod sledećim procesnim uslovima: temperatura od 25–65 °C, koncentracija etanola u rastvaraču za ekstrakciju od 30–90 vol.%, i odnos čvrsta materija prema rastvaraču od 1:15–1:45 v/v. Statistička analiza je izvršena korišćenjem softvera Design-Expert, korišćenjem Boks-Benkenovog dizajna. Odgovori su bili sadržaj ukupnih (poli)fenola, flavonoida i antocijana u dobijenim ekstraktima. Rezultati su pokazali da su odgovarajući modeli površine odgovora visoko statistički značajni ($p < 0,0001$) i dovoljni da opišu i predvide sadržaj ukupnih (poli)fenola, sadržaj flavonoida i sadržaj antocijana sa R^2 od 0,965, 0,980 i 0,972, redom. Optimalni uslovi za ekstrakciju su za ukupne (poli)fenole 48,4 °C, 51,3 vol.% etanola i 1:43,8 v/v odnos čvrsta materija/rastvarač; za flavonoide 58,5 °C, 48,0 vol.% etanola i 1:29,8 v/v odnos čvrsta materija/rastvarač; i za antocijanine 64,2 °C, 73,5 vol.% etanola i 1:44,7 v/v odnos čvrsta materija/rastvarač. Upotreba UAE povećava prinose ekstrakcije povećanjem oslobađanja bioaktivnih jedinjenja, dok primena Boks-Benkenovog dizajna omogućava precizno određivanje optimalnih parametara ekstrakcije, čime se postižu maksimalni prinosi i efikasnost.

Ključne reči: antocijanini; borovnica; ekstrakcija; flavonoidi; optimizacija; (poli)fenoli.

PIYANUN RUANGURAI¹
NATTABUT
TANASANSURAPONG¹
SIRAKUPT PRASITSANHA¹
REWAT BUNCHAN¹
WIPUT TUVAYANOND³
THANA CHOTCHUANGCHUTC
HAVAL^{1,2}
CHAIYAPORN
SILAWATCHANANAI⁴

¹College of Industrial
Technology, King Mongkut's
University of Technology North
Bangkok, Bangkok, Thailand

²Center of Sustainable Energy
and Engineering Materials
(SEEM), King Mongkut's
University of Technology North
Bangkok, Bangkok, Thailand

³Industry Agricultural
Engineering, Rajamangala
University of Technology
Thanyaburi, Pathum Thani,
Thailand

⁴Department of Teacher
Training in Mechanical
Engineering, King Mongkut's
University of Technology North
Bangkok, Bangkok, Thailand

SCIENTIFIC PAPER

UDC 634:66.047:004

UTILIZING MACHINE VISION AND ARTIFICIAL NEURAL NETWORKS FOR DRIED GRAPE SORTING DURING PRODUCTION

Article Highlights

- The five significant characteristics of grapes observed by image processing during the drying process
- An ANN approach is developed to classify completely dried grapes and partially dried grapes
- The ANN model achieved a level of accuracy performance of 78%
- The entirety of the grapes trends into raisins; the dehydration machine will cease operation

Abstract

This study introduces a machine vision technique that utilizes an artificial neural network (ANN) to develop a predictive model for classifying dried grapes during the drying process. The primary objective of this model is to mitigate the burden placed on the operator and minimize the occurrence of over-dried items. The present study involves the development of a model that is constructed using the characteristics of grape color and shape. There exist two distinct categories of labels for grapes: fully desiccated grapes, commonly referred to as raisins, and grapes that have undergone partial drying. Image processing is utilized to collect and observe five significant characteristics of grapes during the drying process. The findings indicate a significant decrease in the levels of red, green, and blue colors (RGB) during the initial 15-hour drying period. The predictive model extracts properties such as RGB color, roundness, and shrinkage from the image while it undergoes the drying process. The artificial neural network (ANN) model achieved a level of accuracy performance of 78%. In this work, the dehydration apparatus will cease operation in an automated manner whenever the entirety of the grapes situated on the tray has been projected to transform raisins.

Keywords: machine vision; grape drying process; artificial neural network; embedded systems.

The contemporary lifestyle of individuals in the present period acknowledges the significant influence

of food consumption on human well-being. Fiber-rich foods are particularly recommended, especially for the senior population, as outlined in the dietary guidelines represented by the food pyramid [1]. Fruits and vegetables are rich sources of dietary fiber, essential vitamins, and minerals. Nevertheless, the availability of fruits is restricted to their respective natural seasons for harvesting. The utilization of preservation techniques aids in prolonging the durability of fruit-based products. Dehydration is a fundamental method employed in fruit preservation to decrease the moisture content of fruits.

Correspondence: C. Silawatchananai, Department of Teacher Training in Mechanical Engineering, King Mongkut's University of Technology North Bangkok, Bangkok, 10800, Thailand.

E-mail: chaiyaporn.s@fte.kmutnb.ac.th

Paper received: 3 October, 2023

Paper revised: 15 May, 2024

Paper accepted: 1 August, 2024

<https://doi.org/10.2298/CICEQ231003030R>

The primary advantage of dehydration is the extension of a product's shelf life. An additional aspect to consider is the convenience of portability and transportation. The dehydration technique is well recognized and utilized in both industrial and home environments. In recent years, there have been notable advancements in dehydration technology, resulting in enhancements in the quality, color, texture, and nutritional composition of dehydrated products. Hence, the utilization of dehydrated food effectively meets the requirements of consumers. Dehydrated items are commonly observed in several food categories such as breakfast cereals, bakeries, snacks, desserts, and convenience meals [2].

Enhancing the quality of dehydrated fruit has become a critical area of investigation. A multitude of scholarly investigations have been conducted to examine the control algorithms employed in dehydrator machines. To regulate the temperature within the chamber, the researchers employed a proportional-integral-derivative (PID) controller that was calibrated using fictitious reference iterative tuning (FRIT) based on Particle Swarm Optimization (PSO) [3]. Another investigation was conducted to regulate the ultimate moisture content (MC) level of the grain. The application of the genetically optimized fuzzy immune proportional integral derivative controller (GOFIP) was utilized to manage grain dryer machines [4].

Numerous research investigations have commenced by investigating the morphological changes that occur in fruit during the drying process under various environmental conditions. For example, in a study conducted by Karaaslan *et al.* (2017), microwave oven drying was employed to examine the impact of moisture ratio on grape drying by utilizing various power levels [5]. Carter *et al.* (2005) conducted a study to investigate the correlation between the moisture content (MC) of grapes and the power level of microwave hoover technology [6]. The research examples aimed to gain comprehension of the impact of power levels and moisture content of grapes, followed by the implementation of mathematical models. In their study, Ojediran *et al.* (2020) presented a novel approach utilizing an Artificial Neural Network (ANN) that incorporates the Takagi-Sugeno fuzzy inference system. This approach, known as the Adaptive Neuro-Fuzzy Inference System, was employed to accurately forecast the residual moisture content of yam slices under convective conditions. The input parameters comprised time, temperature, air velocity, and thickness [7].

Numerous researchers have endeavored to enhance the quality of dehydrated items by the integration of machine vision technology inside their systems. Machine vision is a commonly employed

technique for the surveillance and analysis of objects' chromatic properties, geometric characteristics, and surface qualities. One instance was the utilization of machine vision in a far-infrared drying system to monitor many attributes of ginger, including its properties, moisture ratio, drying rate, browning index, and color difference. The three-stage fuzzy logic control system received two parameters, specifically the browning index and the color difference, as its inputs. The required temperature of the chamber is indicated by the output [8]. Furthermore, the color difference, browning index, perimeter, area, intensity, and diameter of banana slices were observed and recorded throughout the hot air-drying procedure [9].

Over the past decade, ANN has been prominent in the field of dehydration systems. The researchers developed several models for determining the moisture content of grapes by employing ANN and machine vision techniques [10]. Furthermore, ANN was employed to forecast the drying kinetics of paddy, encompassing the moisture ratio and drying rate [11]. Another use of machine learning involves the utilization of categorization models for predictive purposes. The classification of freeze-dried apples with red flesh, such as 'Lex Red', 'Trinity', '314', and '602 Red', was conducted by analyzing image textures and color [12]. For example, the classification of two sultana genotypes, Kecimen and Bensni, was conducted using various textural parameters including area, perimeter, main axis length, minor axis length, eccentricity, convex area, and extent [13]. In their study, Krzysztof *et al.* (2020) employed acoustic signals, comprising frequency and sound level, in conjunction with the ANN Multi-Layer Perceptron, to effectively categorize the dried strawberry as either ripe or overripe [14]. In their study, Masumeh *et al.* (2021) utilized ANN to forecast the moisture content of banana slices and microwave power density throughout the microwave drying procedure [15].

The enhancement of the quality of dehydration products is of considerable importance to researchers, as indicated by much-existing literature. Consequently, numerous promising strategies have emerged in this field. Nevertheless, there are still some areas that require further enhancement, one of which includes the development of cost-effective automatic control systems. During small-scale production, grape dryness is typically assessed by specialists by the observation of color, shrinkage, and texture alterations. In contrast, in industrial settings, the drying process typically terminates once the moisture level of the grapes reaches 13% [16]. This study proposes the implementation of machine vision technology for monitoring the dryness of grapes, providing an

alternative to conventional approaches that rely on expert evaluation or measuring moisture content. Thus, the primary focus of this study is to develop an ANN model to classify fully dried grapes (commonly known as raisins) and grapes that have undergone partial dehydration. This classification task is achieved through the utilization of machine vision data. The proposed approach involves employing machine vision techniques to monitor and gather data on the visual characteristics of the material, including color and form. These data serve as input parameters for predicting the classification of grapes during the drying process. Additionally, the embedded code operates on a Raspberry Pi, a cost-efficient device that utilizes cost-effective technologies.

MATERIAL AND METHODS

Materials

Throughout, a domestic food dehydrator machine was modified to be used as a drying system. The Raspberry Pi connected to the Raspberry Pi Camera module was attached to the top of the chamber to capture images, as shown in Figure 1. The Open-source computer vision library (OpenCV) was integrated with Python to determine grapes' characteristics and classify grapes' labels.

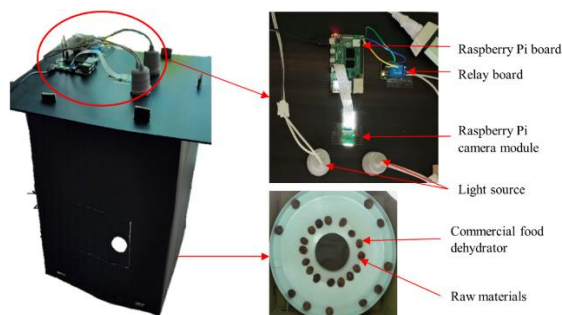


Figure 1. Drying chamber.

The utilization of a domestic food dehydrator machine was adapted to serve as a drying system. The Raspberry Pi, which was connected to the Raspberry Pi Camera module, was affixed to the upper portion of the chamber to take photographs, as depicted in Figure 1. The integration of the Open-source computer vision library (OpenCV) with Python was utilized to determine the features of grapes and classify the labels associated with them.

Preparation of grape samples

Before the drying process, it was necessary to prepare fresh grapes (Ralli Red Seedless) by cleaning and extracting grape seeds. Initially, grapes samples were sensed and cleansed with fresh water. Subsequently, immerse the samples in hot water for 30

seconds. Subsequently, proceed to rinse the washed grapes under a steady stream of cool water without delay. Subsequently, proceed to perforate minuscule apertures in the grapes and desiccate the unprocessed constituents by positioning them above a sanitary surface for approximately 10 minutes.

Drying protocol

Once the preparation of the raw materials was completed, proceed to position them onto a tray situated within the chamber. It was imperative to exercise control over the drying conditions in the experiment. It was crucial to position the grapes distinct from one another to extract the individual characteristics of each grape. The second need entails establishing the temperature at 56 °C. During the drying phase, several photos were recorded and transmitted to the Raspberry Pi controller. Moreover, an image-processing approach was utilized to analyze the characteristics of each grape, including color, roundness, and shrinkage. The ANN technique was employed to classify the properties of both fully dried grapes (raisins) and partially dried grapes drying at regular intervals of twenty minutes. The input in the ANN procedure consisted of the features of the grapes. Upon the completion of the drying process, Raspberry Pi issued a command to activate a relay mechanism, so terminating the power supply to the drying apparatus. Additionally, the system implemented a graphical user interface (GUI) on top of the MQTT protocol in a real-time system.

The drying system's procedure commences with the preparation of images. During this procedure, a grayscale image of the region of interest (ROI) was acquired without any distortion. In the second stage of the image processing procedure, the attributes of grapes, including color, shrinkage, and roundness, were extracted after the preprocessing of the image. The third procedure involved the ANN technique. At this juncture, the system categorized the grape data into two distinct labels: fully-dried grapes and partially-dried grapes. The dataset was divided into three distinct subsets, namely training, validation, and testing. During the training phase, the model for dried grapes was trained by establishing a mapping relationship between the model parameter and the desired output. Once the construction of the model was completed, the trained model was subsequently sent to the Raspberry Pi controller to conduct an analysis and classification of many attributes of dried grapes. In this instance, the image obtained from the camera within the chamber was categorized into two distinct labels. If the model's prediction indicates complete dehydration of all grapes, the relay circuit was responsible for deactivating the

heat source of the dehydrator machine. The comprehensive understanding of each component of the process was listed as follows.

Process1: Image preprocessing

The first protocol to categorize the quality of the dried grapes was performed via the image preprocessing method. The process commenced with the acquisition of RGB images. Subsequently, the undistort function, implemented by OpenCV, was employed to mitigate the distortion present in the image. To track any possible change during the drying process at a fast pace, the dimensions of the unaltered image were decreased from 1280 x 1024 pixels to 640 x 512 pixels. Subsequently, the RGB color image was inputted into a grayscale transformation. The binary mask was utilized to apply the ROI and selectively choose the pixels of interest while excluding undesired pixels. During this particular stage, the undesired pixels were substituted with an intensity value of 127. The sample outcome is depicted in Figure 2.

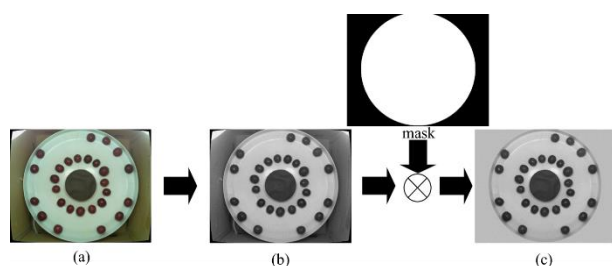


Figure 2. Sample result of preprocessing: (a) Result of undistorting and downscaling; (b) Result of converting RGB to grayscale; (c) Result of selecting ROI and changing intensity of background.

Process2: Image feature extraction

During this phase, the essential discernible characteristics of each grape, including RGB color, roundness, and shrinkage, were retrieved. The aforementioned attributes were utilized as input for training and making predictions. At this stage, the input consisted of the preprocessed image." Subsequently, median filters were implemented to diminish the presence of noise in the image. Afterward, adaptive thresholding was employed to distinguish foreground areas from the background, improving segmentation and significantly reducing glare effects compared to traditional thresholding techniques. In addition, a closing operator was utilized to examine each image for its geometric characteristics, specifically its shape, to enhance image segmentation. Consequently, the revised picture was applied to occupy any empty spaces. The morphological technique was successful in rectifying segmentation mistakes resulting from glare or shade. Additionally, the grapes were subjected to

filtration based on their constituent components, followed by the delineation of the contour of interest. Ultimately, the essential characteristics of each grape were thoroughly isolated. The general procedure is depicted in Figure 3. Furthermore, it was necessary to monitor the location of each grape during the various stages of processing, as the drying process introduced a degree of uncertainty regarding the position of each grape. The Euclidean distance formula was used to compute the displacement between the previous and present positions of each grape. If the calculated distance is minimal, it is assumed that the location remains unchanged for the same grape.

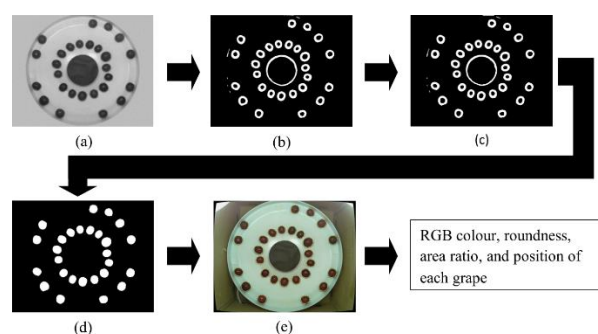


Figure 3. Sample result of feature extraction in the initial image from Figure 2c: (a) Result of filtering; (b) Result of applying adaptive thresholding; (c) Result of performing morphological process; (d) Result of filling holes; (e) Result of drawing grapes' contour.

The measurement of grape shrinkage during the drying process is based on the two-dimensional area ratio. This method is simpler and more practical than direct volume measurement, as outlined in Eq. (1) [10].

$$S(t) = \frac{A(t)}{A(0)} \quad (1)$$

where $S(t)$ is the shrinkage at instantaneous time t . $A(t)$ stands for the sample's surface area in pixels at a time t . $A(0)$ is the sample's surface area in pixels at the initial time.

In similia fashion, roundness was equated via Eq. (2):

$$R(t) = \frac{A(t)}{\pi(r(t))^2} \quad (2)$$

where $R(t)$ is the roundness and the instantaneous radius of the grape $r(t)$, measured in pixels, is defined as the radius of the smallest circle that completely encloses the grape.

Process3: ANN classification

The objective of the artificial neural network (ANN) was to distinguish between two classifications: slightly desiccated grapes and fully desiccated grapes. The experiment observed alterations in the hue,

circularity, and shrinkage of each grape as they underwent the process of dehydration at a temperature of 56 °C. The model was fed with inputs that encompassed the following characteristics: RGB color, roundness, and shrinkage, which were monitored during the drying process, as depicted in Figure 4.

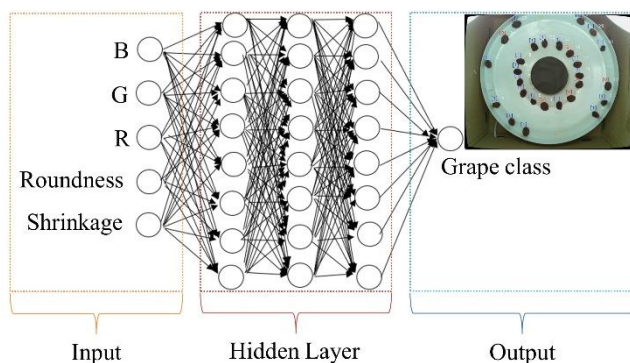


Figure 4. Architecture of the ANN.

The data was partitioned into three sets using a random allocation method. Specifically, 64% of the data was assigned for training purposes, while 18% was allocated for validation and another 18% for testing. During the training data phase, the model's predictions were based solely on the training and validation data. Additionally, early stopping was employed to mitigate the issue of overfitting. The ANN performs intricate computations to analyze intricate patterns, such as the correlation between the characteristics of grapes and the corresponding output label, to classify raisins. The Multi-Layer Perceptron, a feedforward neural network, is utilized in this study, consisting of three hidden layers. Each hidden layer was comprised of eight nodes. Here, the rectified linear unit (ReLU) function was utilized in the hidden layers to perform the transfer of the weighted sum between layers. Additionally, the Rectified Linear Unit (ReLU) activation function was employed as a means of mitigating the issue of vanishing gradients [8]. It was noted that the Rectified Linear Unit (ReLU) originated from a mathematical function that was commonly used in artificial neural networks as shown in Eq. (3):

$$f(z) = \max(0, z) = \begin{cases} 0 & \text{for } z \leq 0 \\ z & \text{for } z > 0 \end{cases} \quad (3)$$

where f is the function of ReLU and z is the weighted sum of a neuron.

The sigmoid function was commonly used as an activation function in two-class classification tasks. It was applied to the weighted sum of inputs to turn it into a probability score. The output of the sigmoid function was binary, with values of either 0 or 1. In this experiment, 0 and 1 stand for partially dried and fully

dried grapes respectively. Mathematically, the sigmoid function was formally defined via Eq. (4):

$$\sigma(z) = \frac{1}{(1 + e^{-z})} \quad (4)$$

where σ is the function of sigmoid and z is the weighted sum of a neuron.

Process4: AC source controlling

The final step involved regulating the AC power supply of the dehydration machine by the act of activating or deactivating it. The Raspberry Pi transmitted a command to a magnetic relay to regulate the power supply inside this system. The alternating current (AC) supply would be deactivated by the relay once the ANN model ascertained that all grapes had reached the desired level of dryness.

RESULTS AND DISCUSSION

To commence the experiment, an examination was conducted to study the drying characteristics of grapes at a temperature of 56 °C. The ANN model for classifying grapes into two distinct labels: partially dried grapes, and fully dried grapes utilizes five significant feature parameters: RGB color, roundness, and shrinkage. These parameters were employed as input during the training process of the model. The dataset was partitioned into three distinct sections. The training dataset consisted of 1,347 samples, which were utilized for training the model. Subsequently, a validation dataset including 380 samples was employed to assess the model's performance during the training process. The final set employed for testing purposes consisted of 370 instances, which were utilized to assess the performance of the model.

Drying protocol

The study focused on examining the physical phenomena of color and shape to evaluate the traits and properties of grapes during the drying process at a temperature of 56 °C.

Initially, an examination was conducted on 27 grapes to ascertain the average intensity change within each RGB color channel. The photographs were captured at intervals of 20 minutes. The average color characteristic is shown as follows Figure 5a. In accordance with the given prompt, the following response will address the academic nature of the user's text without adding any additional information: At the onset of the experiment, it was observed that the red color exhibited the highest intensity, followed by green and blue, respectively. Throughout the process of drying, it was evident that the red color exhibited the

greatest degree of variation, indicating a high level of sensitivity. Notably, there was a significant decline in the red color intensity for 15 hours, after which it reached a state of stability. The patterns for the intensity of green and blue colors were comparable. Initially, there was a minuscule increase. Subsequently, the intensity values underwent a rapid decrease and subsequently stabilized after 15 hours. In comparison to green and blue, it was worth noting that red exhibits the highest level of sensitivity.

The shape of the grapes, taking into account factors such as roundness and shrinkage, represented the second attribute that could be observed. The roundness and shrinkage behavior of grapes exhibited similar patterns, as depicted in Figure 5b and Figure 5c, respectively. The form had a rapid decline for approximately 12 hours and afterward reached a state of stability, remaining unaltered. The sample grapes undergoing dehydration at a temperature of 56 °C are shown in Figure 6.

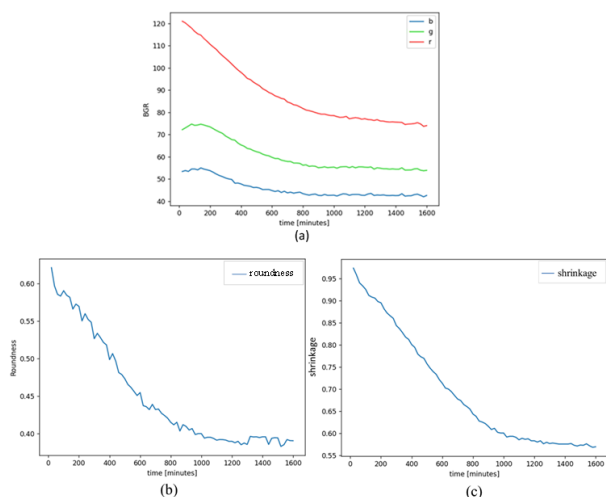


Figure 5. Grape characteristics during the drying process at 56 °C: (a) Result of RGB color; (b) Result of roundness; (c) Result of shrinkage.

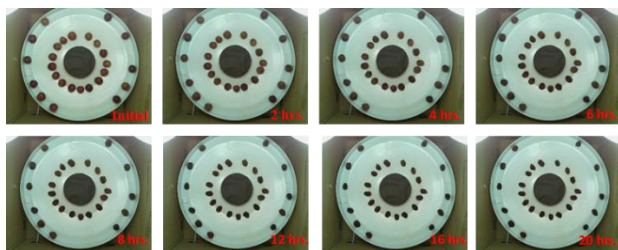


Figure 6. The grapes undergo dehydration at a temperature of 56 °C.

This experiment utilized a small sample size to demonstrate the effects of dehydration on grapes. The color and shape changes seen during the dehydration process remained similar across the entire bin. The grapes underwent dehydration, resulting in browning

and shrinkage. The only significant differences seen were in their initial color and form. This indicates that the data is sufficient to accurately depict the characteristics of grape dryness throughout the dehydration process.

Classification

The classification label was divided into two distinct categories: fully dried grapes and partially dried. The ANN algorithm was applied across five batches of experiments, involving a total of 135 grapes. As a result, the dataset encompassed a total of 2,097 cases. The loss and accuracy curves of the training and validation were determined by the size of the training data set. Figure 7 displays the graphical representation of the performance of the model in terms of loss and accuracy. The utilization of the early stopping function resulted in training and validation accuracies of 0.78 and 0.85, respectively. The performance of the training and validation loss functions was satisfactory, as indicated by the respective losses of 0.50 and 0.42.

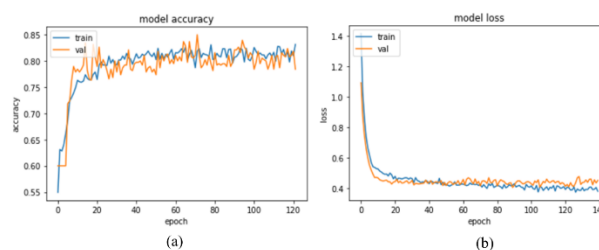


Figure 7. Train and validate learning curves of the ANN model: (a) Model loss; (b) Model accuracy.

Following the prediction of the ANN model, a total of 370 instances were utilized to test the proposed model. The classification outcome is presented in Table 1, wherein two distinct classes are identified: class 1 represents fully dried grapes, while class 0 represents partially dried grapes.

Table 1. Confusion matrix for raisin classification in ANN model.

		Actual	
		Class 1	Class 0
Predicted	Class 1 (fully dried)	95	63
	Class 0 (partially dried)	18	194

The section discussed the categorization of performance. Performance could be defined as the execution or accomplishment of a task, activity, or function, typically measured against predetermined criteria or standards. The precision of each class was quantified based on Eq. (5).

$$P_j = \frac{TP_j}{(TP_j + FP_j)} \tag{5}$$

where P is the precision for class j . TP stands for true-positive and FP stands for false-positive for class j .

Furthermore, the recall in each class (R_j) was defined as,

$$R_j = \frac{TP_j}{(TP_j + FN_j)} \quad (6)$$

where FN stands for false-negative for class j .

In addition, F1-score in each class (F_j) was defined as,

$$F_j = \frac{2 \times P_j \times R_j}{(P_j + R_j)} \quad (7)$$

The accuracy parameter A was defined as follows:

$$A = \frac{TP + TN}{(TP + TN + FP + FN)} \quad (8)$$

where FP stands for false-positive.

The findings indicate that the classification model achieved an accuracy of 78%, with a f1-score of 70%, and 83% for class 1 and class 0, respectively. Furthermore, the performance for class 1 and class 0 was determined to be Table 2.

Table 2. Overall classification performance measurement results.

Class	Precision	Recall	f1-score	Accuracy
Class 1 (fully dried)	60%	84%	70%	78%
Class 0 (partially dried)	92%	75%	83%	78%

The occurrence of inaccurate categorizations in grape drying processes predominantly arises when grapes were only partially dried, yet erroneously identified as fully dried grapes. The scenario of the minority instance arises when the grapes underwent complete dehydration, yet were erroneously classified as partially dried grapes.

Historically, the categorization of dehydrated grape grades has been conducted by specialists. This study presents an alternative approach that utilizes a machine vision-based Artificial Neural Network (ANN) algorithm. The primary advantage of an artificial neural network (ANN) based system is a significant reduction in the burden of specialists. Nevertheless, there is a limitation in evaluating the quality of raisins due to the absence of grape moisture content analysis in the current model, which is an essential aspect in

determining raisin quality. Subsequent improvements to the model will strive to address this constraint.

The process is completed by the machine automatically turning off when the system recognizes that all grapes have completely dried out and become raisins (100% dry). Nevertheless, this setpoint has a disadvantage: it has the potential to cause certain samples to become excessively dry. To alleviate this issue, the setpoint should be established by considering the grapes that have fully dried out in the majority. Therefore, additional tests are required to observe and determine the most favorable value for the ultimate dehydration time under real-life circumstances.

In addition, the primary objective of this experiment was to investigate the feasibility of employing a Raspberry Pi, a cost-effective microcontroller, for classification purposes, as opposed to the conventional utilization of personal computers (PCs) or laptops, which was prevalent in most research endeavors. The cost of a Raspberry Pi, when purchased with a camera module, was approximately \$100. Therefore, it was highly affordable to many small-scale manufacturing businesses. To compromise, the average accuracy of the model was 78%. At this juncture, the acceptability of the situation could be acknowledged; yet, when examining the precision of class 1, it is observed to be merely 60%. Therefore, it is imperative to enhance the accuracy by using more grape attributes, such as the $L^*a^*b^*$ color model. In addition, the inclusion of additional data significantly contributes to the model's ability to attain favorable outcomes. Another aspect to consider is the potential for enhancing accuracy through the utilization of more sophisticated artificial neural network (ANN) methods, such as the deep neural network (DNN) algorithm. Moreover, deep neural networks (DNNs) can yield more accurate outcomes; nonetheless, they still encounter a challenge while processing large volumes of data. In subsequent research endeavors, the proposed model will evaluate the algorithm's performance in real-world scenarios, specifically involving the placement of intact grapes within the tray. The ultimate objective of the future work is to achieve a fully automated system.

CONCLUSION

In this research, a machine vision system was employed to monitor dried grapes during the drying process. The ANN algorithm is applied to create the model for classifying grapes' class labels as completely dried and partially dried grapes. The model's input

parameters include color (RGB color) and shape (roundness and shrinkage). The model's performance in classification shows a satisfactory result with an accuracy of 78%. When the system determines that all grapes are raisins, the AC power of the dehydration machine will automatically turn off. Then, the proposed system is aimed at reducing over-dried products and the workload of the operator.

ACKNOWLEDGEMENTS

This research was funded by King Mongkut's University of Technology North Bangkok. Contract no. KMUTNB-65-BASIC-32.

REFERENCES

- [1] L.M. Donini, S. Claudia, C. Carlo, Arch. Gerontol. Geriatr. 49 (2009) 61–69. <https://doi.org/10.1016/j.archger.2009.09.013>.
- [2] R. Megias-Pérez, J. Gamboa-Santos, A.C. Soria, M. Villamiel, A. Montilla, Food Chem. 150 (2014) 41–48. <https://doi.org/10.1016/j.foodchem.2013.10.141>.
- [3] P. Ruangurai, C. Silawatchananai, S. Howimanporn, PSO based Fictitious Reference Iterative Tuning of air dryer for fruit drying process, in Proceeding of 2020 9th International Congress on Advanced Applied Informatics (IIAI-AAI), Kitakyushu, Japan (2020), p. 548. <https://doi.org/10.1109/IIAI-AAI50415.2020.00114>.
- [4] A. Dai, X. Zhou, X. Liu, IEEE Access 5 (2017) 14981–14990. <https://doi.org/10.1109/ACCESS.2017.2733760>.
- [5] S. Karaaslan, K. Ekinci, D. Akbolat, Infrastrukt. Ekolog. Terenów Wiejskich IV/1 (2017) 1317–1327. <https://doi.org/10.14597/infraeco.2017.4.1.101>.
- [6] C. Carter, W. Shaojin, E.P. Vincent, J. Food Sci. 70 (2005) E344–E349. <https://doi.org/10.1111/j.1365-2621.2005.tb09975.x>.
- [7] J.O. Ojediran, C.E. Okonkwo, A.J. Adeyi, O. Adeyi, A.F. Olaniran, N.E. George, A.T. Olayanju, Heliyon 6 (2020) E03555. <https://doi.org/10.1016/j.heliyon.2020.e03555>.
- [8] Y. Pei, Z. Li, C. Ling, L. Jiang, X. Wu, C. Song, J. Li, F. Song, W. Xu, Food Measure. Charact. 16 (2022) 3815–3831. <https://doi.org/10.1007/s11694-022-01453-8>.
- [9] P. Ruangurai, T. Nachan, R. Bunchan, C. Silawatchananai, Monitoring characteristics of dried banana slices using image processing, in Proceeding of 2021 18th International Conference on Electrical Engineering/Electronics, Computer, Telecommunications and Information Technology: Smart Electrical System and Technology, Chiang Mai, Thailand (2021), p. 148. <https://doi.org/10.1109/ECTI-CON51831.2021.9454907>.
- [10] N. Behroozi Khazaei, T. Tavakoli, H. Ghassemian, M.H. Khoshtaghaza, A. Banakar, Comput. Electron. Agric. 98 (2013) 205–213. <https://doi.org/10.1016/j.compag.2013.08.010>.
- [11] R. Subramanyam, M. Narayanan, Chem. Ind. Chem. Eng. Q. 29 (2023) 87–98. <https://doi.org/10.2298/CICEQ220106017S>.
- [12] E. Ropelewska, D.E. Kruczyńska, A.M. Rady, K.P. Rutkowski, D. Konopacka, K. Celejewska, M. Mieszczakowska-Fraç, Agriculture 13 (2023) 562. <https://doi.org/10.3390/agriculture13030562>.
- [13] I. Cinar, M. Koklu, S. Tasdemir, Gazi J. Eng. Sci. 6 (2020) 200–209. <https://doi.org/10.30855/gmbd.2020.03.03>.
- [14] K. Przybyl, A. Duda, K. Koszela, J. Stangierski, M. Polarczyk, L. Gierz, Sensors 20 (2020) 499. <https://doi.org/10.3390/s20020499>.
- [15] M. Sabzevari, N. Behroozi-Khazaei, H. Darvishi, J. Food Process Eng. 44 (2021) e13796. <https://doi.org/10.1111/jfpe.13796>.
- [16] A. Patidar, S. Vishwakarma, D. Meena, Food Front 2 (2021) 46–61. <https://doi.org/10.1002/fft2.64>.

PIYANUN RUANGURAI¹
NATTABUT
TANASANSURAPONG¹
SIRAKUPT PRASITSANHA¹
REWAT BUNCHAN¹
WIPUT TUVAYANOND³
THANA CHOTCHUANGCHUTC
HAVAL^{1,2}
CHAIYAPORN
SILAWATCHANANAI⁴

¹College of Industrial
Technology, King Mongkut's
University of Technology North
Bangkok, Bangkok, Thailand

²Center of Sustainable Energy
and Engineering Materials
(SEEM), King Mongkut's
University of Technology North
Bangkok, Bangkok, Thailand

³Industry Agricultural
Engineering, Rajamangala
University of Technology
Thanyaburi, Pathum Thani,
Thailand

⁴Department of Teacher
Training in Mechanical
Engineering, King Mongkut's
University of Technology North
Bangkok, Bangkok, Thailand

NAUČNI RAD

KORIŠĆENJE OBRADE SLIKE I VEŠTAČKIH NEURALNIH MREŽA ZA SORTIRANJE SUŠENOG GROŽĐA TOKOM PROIZVODNJE

Ovaj rad uvodi tehniku obrade slike koja koristi veštačku neuronsku mrežu (ANN) za razvoj prediktivnog modela za klasifikaciju suvog grožđa tokom procesa sušenja. Primarni cilj ovog modela je da se ublaži teret koji se stavlja na operatera i minimizira pojavu previše osušenih grozdova. Ova studija podrazumeva razvoj modela koji se konstruiše korišćenjem karakteristika boje i oblika grožđa. Postoje dve različite kategorije za grožđe: potpuno isušeno grožđe, koje se obično naziva suvo grožđe, i grožđe koje je podvrgnuto delimičnom sušenju. Obrada slike se koristi za prikupljanje i posmatranje pet značajnih karakteristika grožđa tokom procesa sušenja. Nalazi ukazuju na značajno smanjenje nivoa crvene, zelene i plave boje (RGB) tokom početnog perioda sušenja od 15 sati. Prediktivni model izdvaja svojstva, kao što su RGB boja, zaobljenost i skupljanje iz slike, dok se grožđe podvrgava procesu sušenja. Model veštačke neuronske mreže (ANN) postigao je nivo tačnosti od 78%. U ovom radu, aparat za dehidraciju će automatski prestati sa radom kad god se planira da celokupno grožđe na tacni preobrazi u suvo grožđe.

Ključne reči: obrada slike; proces sušenja grožđa; veštačka neuronska mreža; ugrađeni sistemi.

JUNHEE HAN¹
HYOJUNG KIM²
DOHYUNG LEE³

¹Department of Mechanical
Engineering, Hanyang
University, Seoul, Korea

²Ackerton Partners, 41,
Cheonggyecheon-ro, Jongno-gu,
Seoul, Korea

³Department of Mechanical
Engineering, Hanyang
University, Ansan, Gyeonggi-do,
Korea

SCIENTIFIC PAPER

UDC 66.094.941:54:66.017

SUPPRESSING PRE-HYDROLYSIS IN TiO₂ MANUFACTURING: DESIGN OPTIMIZATION OF AN INDIRECT HEATING HYDROLYSIS SYSTEM

Article Highlights

- An indirect heating system was developed for inhibiting TiO₂ pre-hydrolysis
- Multiphase heat transfer CFD simulation with the immersed solid method was conducted
- The optimized indirect heating system has been stably operated in the real field
- The uniformity of TiO₂ particles was confirmed by the Settling Value test and TEM analysis

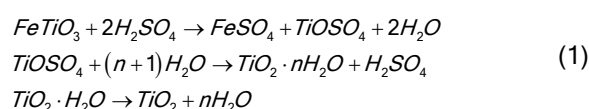
Abstract

The particle size of TiO₂ is critically influenced by the operation of the hydrolysis process. Failure to achieve uniform particle size during hydrolysis can have significant repercussions on subsequent processes, such as washing, reduction, and bleaching procedures, ultimately leading to the production of unusable final products. The primary goal of this study is to suppress pre-hydrolysis, which is a factor that impedes the formation of uniform particles during the hydrolysis procedure. To overcome this issue, the researchers designed an indirect heating system to mitigate the pre-hydrolysis phenomenon. For designing an indirect heating system, multiphase Computational Fluid Dynamics (CFD) simulations were performed. The proposed optimized design was then implemented and tested in the actual field. The success of the field test was evaluated through settling value tests conducted on the hydrolyzed solution, and the uniformity of particle size was analyzed using Transmission Electron Microscopy (TEM) images, Scanning Electron Microscope (SEM), and Microtrac. The findings of this study demonstrate the effective application of the developed multiphase CFD simulation in enhancing the hydrolysis process for the production of anatase titanium dioxide particles. This successful integration demonstrates the application of mechanical engineering techniques in the field of chemical engineering.

Keywords: multiphase; conjugate CFD simulation; precipitation; particle size distribution; TiO₂ manufacturing; indirect heating hydrolysis.

Titanium dioxide is a widely used white pigment in industries such as coatings, paints, paper, plastic, rubber, ceramics, and textiles. There are two main

structures of titanium dioxide particles: rutile and anatase, depending on the production method [1,2]. This paper will specifically focus on the sulfate process, which involves the decomposition of titanium-containing raw materials through sulfuric acid and subsequent hydrolysis of titanium sulfate [3]. The chemical reactions integral to the sulfate process are illustrated in Eq.(1) below.



Correspondence: D. Lee, Department of Mechanical Engineering, Hanyang University, Ansan, Gyeonggi-do, Korea.
E-mail: Dohyung@hanyang.ac.kr
Paper received: 31 July, 2023
Paper revised: 1 August, 2024
Paper accepted: 26 August, 2024

<https://doi.org/10.2298/CICEQ230731031H>

To achieve high-quality white pigment production, precise and stable control of the hydrolysis process is essential. Many TiO₂ manufacturing industries have undertaken efforts to optimize this process [4–8]. The typical hydrolysis procedure for TiO₂ manufacturing involves introducing high-temperature steam into a TiSO₄ solution using bottom-mounted steam nozzles. After reaching a specific temperature (96 °C), external seeds are added to initiate hydrolysis [9–11]. However, the initial heating phase can lead to temperatures exceeding 110 °C at the nozzle location, potentially causing pre-hydrolysis before seed introduction [12,13]. This pre-hydrolysis leads to the formation of particles smaller than 100 nm, which can clog filter cloth pores during washing. This phenomenon acts as a bottleneck that directly impacts the overall manufacturing capacity [14,15].

The most effective approach to prevent pre-hydrolysis is to perform the first heating step using a water-free heat source [16]. Subsequently, the second and third heating steps, where seeds are present, should utilize conventional steam direct heating appropriately. To achieve this, a preheating tank with an indirect heating system using a heating coil is proposed for the first heating procedure and it should be positioned prior to the existing hydrolysis tank.

The design of the indirect preheating tank requires multiphase CFD simulation to handle the two phases present: The TiSO₄ solution filled inside the tank and the steam flowed into the heating coil. The simulation will help in identifying the appropriate shape of the heating coil, which can uniformly heat the solution to 96 °C within 20 minutes.

However, conducting multiphase CFD simulations presents challenges in terms of computing power and time, especially when compared to single-phase simulations. This complexity arises from considering multiple working fluids and boundary interfaces. In cases involving rotating fluid machinery within multiphase CFD simulations, the mesh must be regenerated at each time step to account for the interface between the rotating and stationary regions. This re-meshing process demands a considerable amount of additional computing power

Therefore, many researchers have developed CFD methods to reduce computing time, such as the moving reference frame (MRF) [17,18], sliding mesh (SM) [19–21], overlapping grids [22,23], and so on. However, these methods often sacrifice accuracy for computational efficiency and are mainly used for steady-state simulations. In this study, since the time-dependent temperature distribution and heat transfer are crucial, we aim to explore the Immersed Solid Mesh

(ISM) technique along with these methods to reduce computational time while preserving accuracy [24–28]. In traditional applications, the Immersed Solid Method (ISM) has primarily been utilized for tracking the trajectories of solid particles within a Discrete Element Method (DEM), where considerations of mass transfer or heat transfer are not included.

However, this study aims to utilize the Immersed Solid Method (ISM) to conduct a multiphase simulation, which includes heat transfer between a fluid and gas through a heating coil solid body. By employing ISM, the computational domain can be extended to virtually model the solid structures surrounding the fluid, leading to enhanced accuracy in the analysis and reducing the necessity for frequent mesh generation and updates. By analyzing the heat distribution inside the tank and on the surface of the heating coil, this study aims to optimize the design of the heating coil for an indirect heating system.

MULTI-PHASE CFD SIMULATION

Governing equation

The Navier-Stokes equation serves as the principal governing equation for general single-phase Computational Fluid Dynamics (CFD) applications, represented as Eq.(2).

$$\rho g_x - \frac{\rho p}{\rho x} + \frac{\partial}{\partial x} \left(2\mu \frac{\partial u}{\partial x} - \frac{2}{3} \mu \nabla \cdot \vec{V} \right) + \frac{\partial}{\partial y} \left[\mu \left(\frac{\partial u}{\partial x} + \frac{\partial v}{\partial x} \right) \right] + \frac{\partial}{\partial z} \left[\mu \left(\frac{\partial w}{\partial x} + \frac{\partial u}{\partial z} \right) \right] = \rho \frac{\partial u}{\partial t} + \rho \left(\vec{V} \cdot \nabla \right) u \quad (2)$$

In a typical multiphase CFD solver, when two different phases of fluids come into contact, force and mass exchange occur, leading to the formulation of equations like Eq.(3) and Eq.(4).

$$\text{Continuity: } \frac{\partial (\alpha_q \rho_q)}{\partial t} + \nabla (\alpha_q \rho_q u_q) = \sum_{p=1}^n \dot{m}_{pq} \quad (3)$$

$$\text{Energy: } \frac{\partial (\rho U)}{\partial t} - \nabla (\rho U h_{tot}) = \nabla (\kappa \nabla T) + \nabla (U \nabla \tau) + S_M \quad (4)$$

The meaning of α_q is the Volume fraction of q^{th} phase, and the momentum equation of q^{th} phase can be written as the following Eq.(5)

$$\frac{\partial (\alpha_q \rho_q u_q)}{\partial t} + \nabla (\alpha_q \rho_q u_q) = -\alpha_q \nabla p + \alpha_q \rho_q g + \nabla \tau_q + \sum_{p=1}^n \left(R_{pq} + \dot{m}_{pq} u_q \right) + \alpha_q \rho_q (F_q + F_{lit,q} + F_{vm,q}) \quad (5)$$

where R_{pq} is interphase forces exchange, and $\dot{m}_{pq} u_q$ is

interphase mass exchange. However, in this study, the heating coil inhibits mass exchange between two different phases and only allows heat exchange between them. As a result, terms related to R_{pq} , $\dot{m}_{pq}u_q$ become zero during the calculation process, and only heat transfer through volume calculations of different phases is considered.

CFD PROCEDURE AND RESULTS

Geometry and mesh generation

The tank present on the site has dimensions of 3.35m x 3.45m and features a 5° downward slope at the base to facilitate liquid drainage. Inside the tank, there

are two-stage blades with a 45° pitch angle for smooth solution mixing, along with an indirect heating coil. The actual field geometry is illustrated in Fig. 1a and computational geometry is explained in Fig. 1b.

Two different methods can be used for mesh generation: the conventional method of General Grid Interfacing (GGI), and a simpler method utilizing the Immersed Solid Method (ISM). These two types of mesh generations are explained in Fig. 1c. When generating the mesh using the immersed solid mesh (ISM) method, the total number of mesh elements was reduced by over 20% compared to using the GGI (General Grid Interface) method, while keeping the same growth rate and mesh setup values.

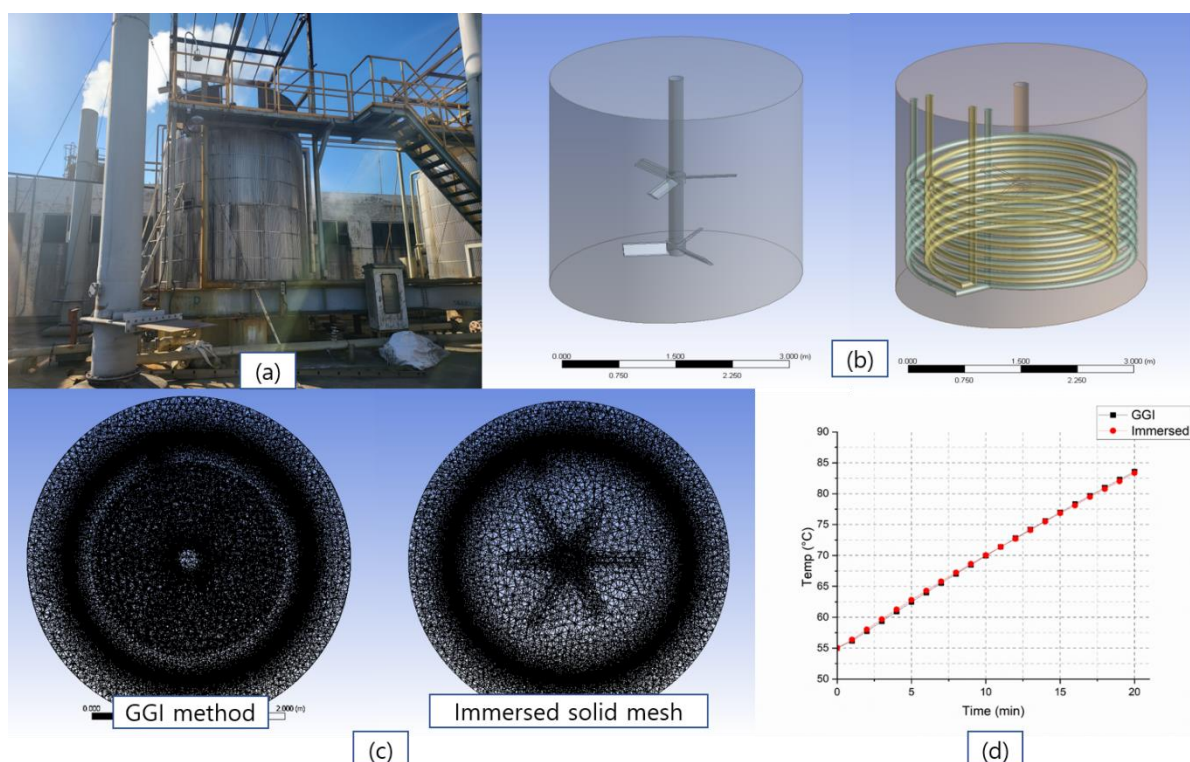


Figure 1. Geometry of indirect heating system.

Specifically, the GGI method resulted in approximately 8.8 million mesh elements, whereas the ISM approach yielded a mesh with 5.9 million elements. Comparing the Immersed Solid Method (ISM) with the GGI method, the ISM technique led to a remarkable 25% reduction in computation time for a total simulation timestep of 20 minutes. The GGI method required 72 hours, while the ISM method completed the simulation in 54 hours. Additionally, when assessing the average temperature of $TiOSO_4$ the solution, both methods exhibited a temperature deviation of less than 1 degree. Therefore, in this study, the Immersed Solid Method (ISM) approach was employed while maintaining the accuracy of CFD calculations. The temperature rise curves calculated using the GGI

method and the immersed solid mesh are shown in Figure 1d. The curves indicate that there is little difference in the temperature rise, with the GGI method requiring 59 hours of computing time for a 20 minute real-time step, while the immersed solid mesh required 41 hours. However, due to the mesh not being fine enough, the accurate capture of eddy movements near the blunt body was not achieved, resulting in slight differences in the temperature contour.

Therefore, the simulation using the immersed solid mesh is a suitable method for scenarios like optimization processes where high accuracy is not essential, and many cases need to be computed in a short amount of time, similar to the DOE (Design of

Experiments) method.

Boundary condition

The tank is filled with TiOSO₄ solution and high-pressure steam at 5 bar and 185 °C is supplied through the heating coil. The steam outlet is set as an opening condition because it is not subjected to any external pressure and is open to atmospheric pressure. Table 1 describes the properties of the working fluid.

Table 1. Property of TiOSO₄ and wet steam.

Identification	TiOSO ₄	Wet steam
<i>m</i> (Molar mass)	159.92 g/mol	18.01528 kg/kmol
ρ (Density)	1.5954 g/cm ³	2.669 kg/m ³
<i>c</i> (Specific heat capacity)	1070 J/kg.K	2.3289 kJ/kg.K
η (Dynamic viscosity)	0.001 kg/ms	0.000014 kg/ms
κ (Thermal conductivity)	0.6 W/m.K	0.003 W/m.K
Initial condition	1 atm, 55 °C	5 bar, 185 °C

The heat transfer process involves two distinct heat interfaces. The first interface encompasses the inner surface of the pipe through which steam is

introduced, coming into direct contact with the steel material. The second heat interface is formed at the contact surface between the steel material and the TiOSO₄ solution. This simulation specifically considers heat transfer exclusively across these interfaces. For the steel material, 10 mm thickness 100 A of 316 L stainless steel property was used for heat conductivity and thermal expansion coefficient. The Agitator, using the Immersed Solid Method, rotates clockwise at 35 rpm, while the wall is subjected to a no-slip boundary wall condition.

Simulation results

To initiate the seed injection process, The TiOSO₄ the solution in the indirect heating tank should be heated up to a target temperature of 96 °C for 20 minutes. Firstly, a performance evaluation of a single heating coil was carried out. The height of the coil was limited to 2000 mm from the bottom, taking into account the height of the liquid and the agitator blade. Figure 2 represents the temperature contour on the surface of the single heating coil and streamline at the side plane of the tank. It demonstrates that the temperature distribution on the heating coil surface varies according to the fluid flow.

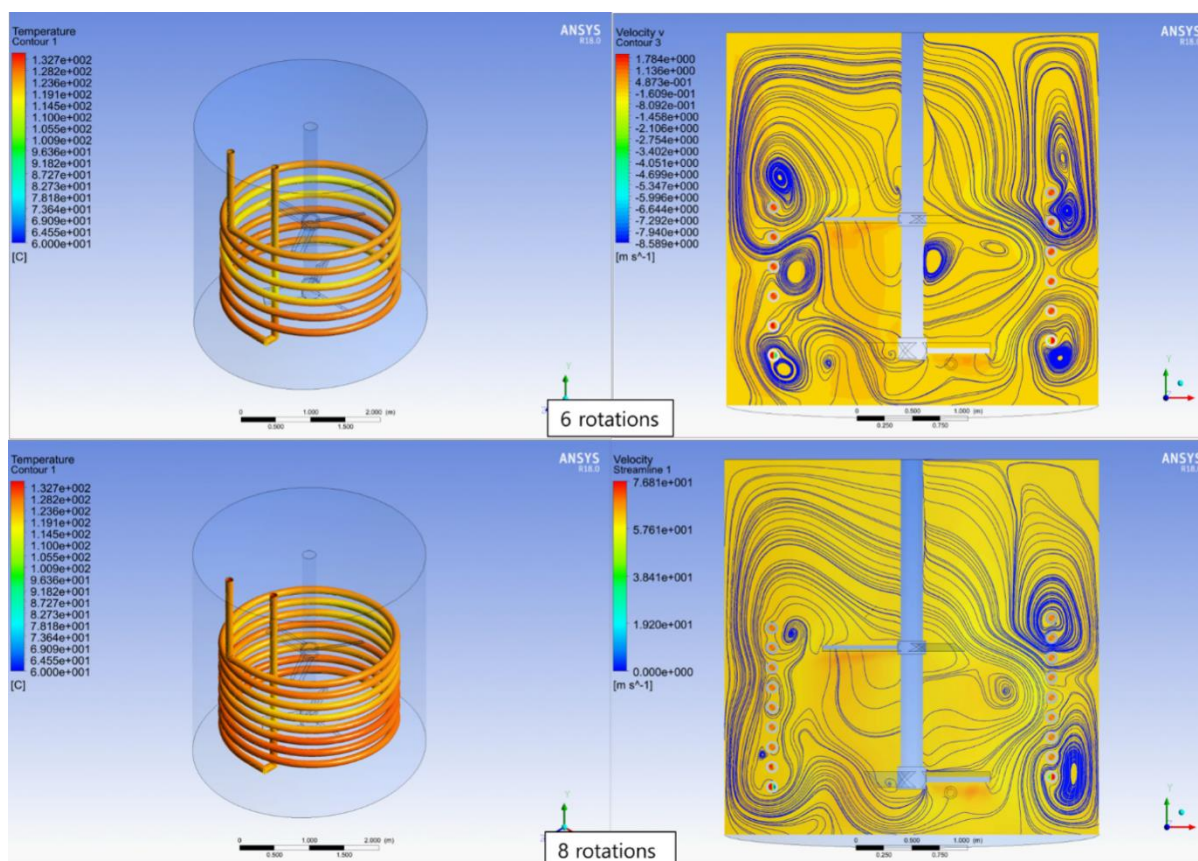


Figure 2. Temperature distribution on single heating coils surface.

This emphasizes the results of heat transfer between gas-solid-fluid, which fundamentally differs from conventional CFD simulations that involve setting a heat source on a typical wall surface. In addition, in the region where the agitator rotates, the fluid exhibits high turbulence kinetic energy, leading to vigorous heat exchange between the heating coil and the $TiOSO_4$ solution. As a result, the temperature on the surface of the heating coil facing the agitator appears to be lower compared to other areas.

Table 2. The average temperature of different single heating coils.

Coil rotation (times)	Temperature of $TiOSO_4$ after 20 min (°C)
6	77
7	80
8	83
9	84

As shown in Table 2, even though heat exchange was vigorous, it was not possible to reach the desired target temperature within the limited height and time using a single heating coil. When rotating the coil 10 times, the gap between the heating coils becomes less than 10cm. Based on the experience and CFD simulation, the possibility of scale formation between the coils becomes very high in such cases. Therefore, the simulations were conducted excluding the results after 10 rotations.

It is necessary to install the double heating coils

to increase heating efficiency. In the design range, the heating coil was installed from 6 to 9 rotations, the same as in a single stage, and the heat change was observed for up to 20 minutes.

Table 3. The average temperature of different double-heating coils.

Coil rotation (times)	Temperature of $TiOSO_4$ after 20 min (°C)
6	92.375
7	96.337
8	101.415
9	101.7

As can be seen from Table 3 and Fig. 3, it is evident that there is a significant increase in temperature from the 6th rotation to the 8th rotation. However, from the eighth rotation, there is no more temperature rise.

The inner heating coil surface facing the agitator exhibits a relatively lower heat distribution compared to other areas due to the presence of active heat transfer with the $TiOSO_4$ solution. On the other hand, the outer heating coil positioned facing the wall has limited heat transfer to the solution, resulting in a relatively higher surface temperature distribution. Furthermore, as the number of coil revolutions increases, it can be observed that the outer portion of the heating coil fails to transfer heat effectively and still maintains a very high surface temperature.

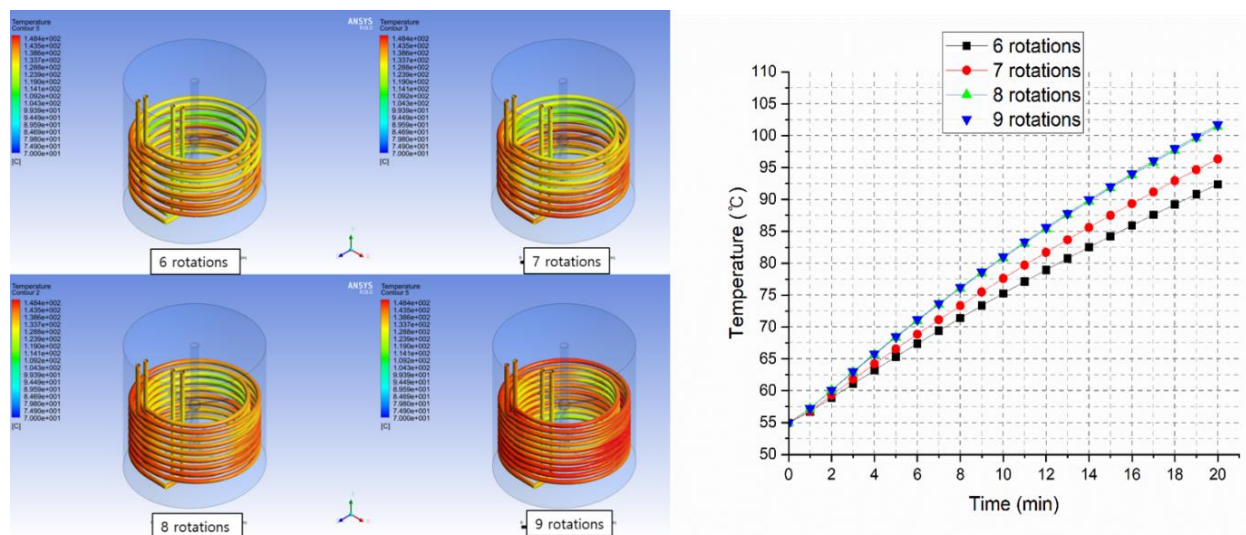


Figure 3. Temperature distribution on double heating coils surface and streamlining of $TiOSO_4$ solution.

Figure 4 illustrates the temperature distribution of the side plane, turbulence eddy dissipation, and the velocity in the v direction. In the case of 6-rotation, the $TiOSO_4$ the solution flows smoothly between the heating coils, allowing for sufficient heat transfer. On the contrary, in the case of 9-rotation, the narrow

spacing between the heating coils hinders the flow of the working fluid.

The simulation results of this study demonstrated that the heating of the $TiOSO_4$ the solution to 96 °C within the targeted 20 minutes is achieved by the utilization of an 8-rotation double heating coil.

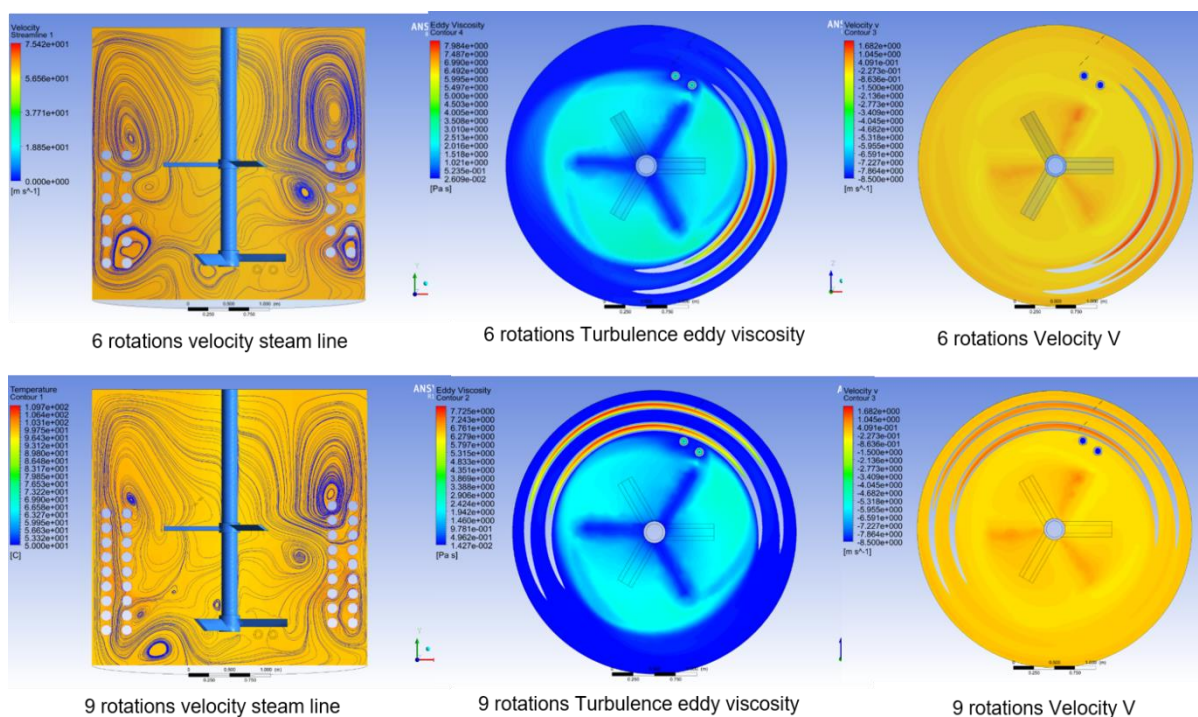


Figure 4. Indirect heating coil installation and TiOSO₄ solution.

Lab scale test and results

The results calculated by CFD were tested in a lab-scale pilot facility reduced to a 38:1 scale. The TiOSO₄ solution, heated without the addition of moisture, underwent hydrolysis, reduction, washing, calcination, and milling processes. The particle distribution was analyzed using SEM and microtrac techniques. Figure 5 shows the particle distribution as determined by SEM analysis and microtrac. Particles within the target specification of 300–400 nm account for 50.49% and 51.02% of the total, while particles within the nominal specification of 200–500 nm account for 84.88% and 85.25% of the total.

Comparatively, the direct heating system with moisture injection showed a distribution of less than 80% in the same experiment, indicating an improvement of over 5% with the indirect heating system. However, real field tests show a proportion exceeding 90%. The approximately 5% difference is attributed to the effects of boiling bubbles during heating, despite matching the Froude number to ensure experimental similarity. The presence of bubbles introduces various forces, such as virtual force, lift force, drag force, lubrication force, and turbulence dispersion force, which differ between a 5m diameter tank and a 20 cm tank.

This discrepancy highlights an area for future research. Nonetheless, the consistent trend in particle distribution observed in the experiments confirms the effectiveness of the indirect heating method and its

applicability to real field tests.

Actual field test and results

The 8-rotation double indirect heating coil with optimized agitator design, which demonstrated the most favorable heat diffusion based on the simulation results [8], was installed at the site. Subsequently, the settling value was examined to assess the outcomes.

A settling value test, widely employed for assessing particle size uniformity, was conducted to determine whether the indirect heating system inhibits pre-hydrolysis. The settling value test involves diluting 114 ml (190g/L TiO₂) of the hydrolyzed solution with 300ml of water. After cooling to 25 degrees, additional water is added to make up a 500 ml solution. After 30 minutes, the suspension length is measured. A high settling value indicates a broader accumulation of smaller particles in the gaps between larger particles, resulting in a longer suspension length. On the contrary, a low settling value demonstrates that larger than 400 nm TiO₂ particles are uniformly generated and there are significant presence of voids between particles. Figure 6 as shown below, presents the results of the settling value test, where the length of the clear portion in the supernatant is measured and recorded as the settling value.

To conduct the settling value test, a hydrolyzed solution is required. The solution used for the test is obtained by completing the hydrolysis process with indirect heating for the primary heating and steam direct

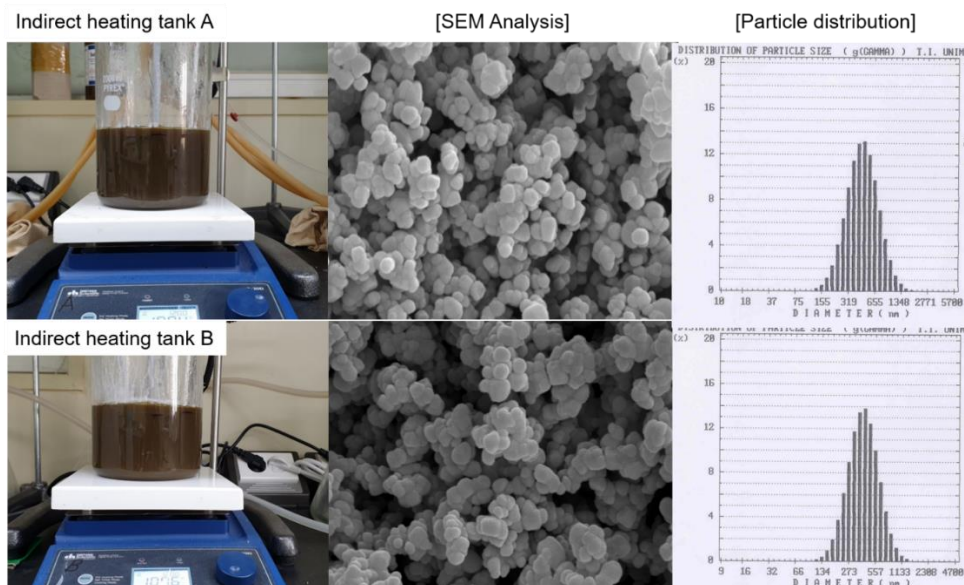


Figure 5. Comparison of settling values between direct heating and indirect heating.

heating for the secondary and tertiary heating stages. The hydrolyzed solution obtained without using an indirect heating system exhibited an average settling value of 65 mm/30 min. Moreover, there were instances where defective hydrolyzed solutions with a settling value of even 70 mm/30 min, rendering them unusable, were occasionally generated. On the other hand, with indirect heating, the settling values remained favorable, ranging from 55 mm/39 min to 45 mm/30 min.

Table 4. Settling values of indirect heating system.

Case	Settling value (mm/30 min)	Case	Settling value (mm/30 min)
1	51	4	48
2	55	5	45
3	52	6	49

The bottom side of Fig. 6 represents TEM (Transmission Electron Microscopy) images of the indirect heating process, zoomed in at 10000x magnifications. It can be observed that the particles in the size range of 0.1 micrometers significantly decreased compared to the single-blade agitator and direct heating methods. However, it is important to note that TEM images alone cannot provide a definitive judgment. TEM serves as supporting evidence, but for quantitative comparison and analysis, it is more appropriate to compare the settling values test.

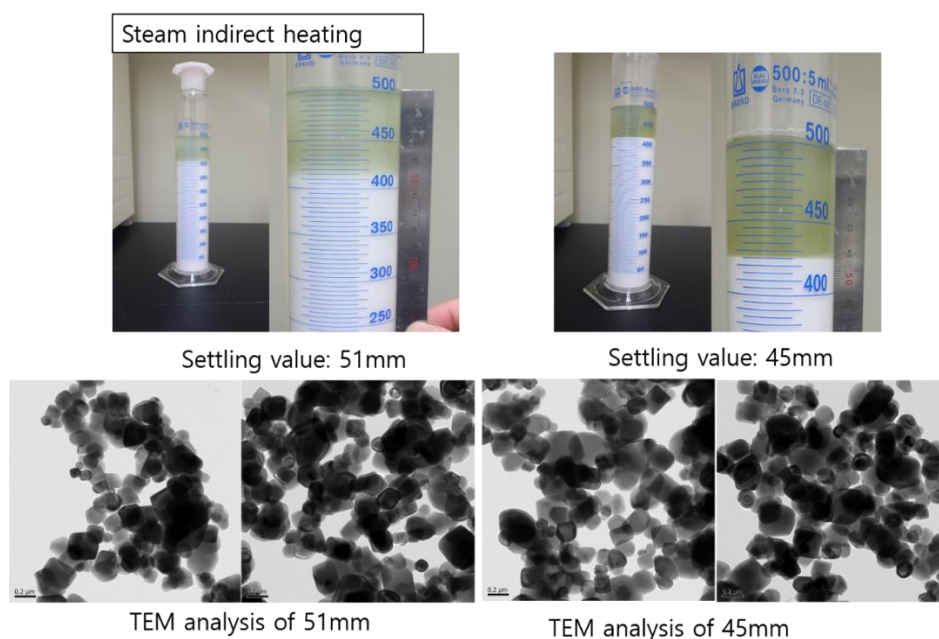


Figure 6. TEM analysis of indirect heating system.

CONCLUSION

In this study, an indirect heating system for the efficient hydrolysis of TiOSO₄ solution was designed and optimized using multiphase computational fluid dynamics (CFD) simulations. The developed CFD solver is capable of handling gas-solid-fluid heat transfer in a multi-phase environment. The optimized design of the indirect heating system was further validated through real field tests, demonstrating its ability to generate TiO₂ particles with a high level of uniformity.

The results indicate that the indirect heating system effectively prevents pre-hydrolysis, addressing one of the major challenges faced in the hydrolysis process. This achievement is supported by advanced characterization techniques such as settling value test and, Transmission Electron Microscopy (TEM), Scanning Electron Microscope (SEM), and Microtrac. These results provide insights into the particle size distribution and settling behavior of the hydrolysis products. The completed hydrolyzed from the first-stage heating procedure, achieved through the designed indirect heating system, successfully yields uniform particle sizes. Furthermore, this has enabled the overall stable operation of the hydrolysis process. Furthermore, the successful implementation of the immersed solid method in multiphase CFD has been demonstrated, particularly in the context of rotating machinery. This achievement highlights its broad potential applicability within various areas of the chemical engineering industry.

ACKNOWLEDGEMENTS

This research was supported by COSMO Chemical Co., Ltd.

REFERENCES

- [1] X. Xiong, Z. Wang, F. Wu, X. Li, H. Guo, *Adv. Powder Technol.* 24 (2013) 60–67. <https://doi.org/10.1016/j.apt.2012.02.002>.
- [2] K.H. Cheung, M.B. Pabbruwe, W.F. Chen, *Ceram. Int.* 47 (2021) 1609–1624. <https://doi.org/10.1016/j.ceramint.2020.08.277>.
- [3] B. Grzmil, D. Grela, B. Kic, *Pol. J. Chem. Technol.* 11 (2009) 15–21. <https://doi.org/10.2478/v10026-009-0030-1>.
- [4] K.D. Kim, S.H. Kim, H. Taik, *Colloids Surf., A* 254 (2005) 99–105. <https://doi.org/10.1016/j.colsurfa.2004.11.033>.
- [5] E.A. Moskalenko, A.A. Sadovnikov, A.E. Baranchikov, A.E. Goldt, V.V. Kozik, V.K. Ivanov, *Curr. Microwave Chem.* 1 (2014) 81–86. <https://doi.org/10.2174/2213335601666140404163607>.
- [6] M. Danish, S. Ambreen, A. Chauhan, A. Pandey, J. Saudi Chem. Soc. 19 (2015) 557–562. <https://doi.org/10.1016/j.jscs.2015.05.010>.
- [7] Y. Bessekhouad, D. Robert, J.V. Weber, *J. Photochem. Photobiol., A* 157 (2003) 47–53. [https://doi.org/10.1016/S1010-6030\(03\)00077-7](https://doi.org/10.1016/S1010-6030(03)00077-7).
- [8] J.H. Han, H.J. Kim, D.H. Lee, *J. Enhanced Heat Transfer* 30 (2023) 1–20. <http://doi.org/10.1615/JEnhHeatTransf.2023047657>.
- [9] E.A. Barringer, H.K. Bowen, *Am. Chem. Soc.* 1 (1985) 420–428. <https://doi.org/10.1021/la00064a005>.
- [10] S. Mahshid, M. Askari, M.S. Ghamsari, *J. Mater. Process. Technol.* 189 (2007) 296–300. <https://doi.org/10.1016/j.jmatprotec.2007.01.040>.
- [11] Q. Zhang, L. Gao, J. Guo, *J. Eur. Ceram. Soc.* 20 (2000) 2153–2158. [https://doi.org/10.1016/S0955-2219\(00\)00085-6](https://doi.org/10.1016/S0955-2219(00)00085-6).
- [12] N. Shijie, L. Debao, L. Yunshi, Y. Ping, *J. Nanosci. Nanotechnol.* 17 (2017) 3430–3434. <https://doi.org/10.1166/jnn.2017.12808>.
- [13] D.C.M. Dutoit, M. Schneider, R. Hutter, A. Baiker, *J. Catal.* 161 (1996) 651–658. <https://doi.org/10.1006/jcat.1996.0227>.
- [14] U. Gesenhues, *Chem. Eng. Technol.* 26 (2003) 25–33. <https://doi.org/10.1002/ceat.200390001>.
- [15] J. Olabarrieta, O. Monzon, Y. Belaustegui, J. Inaki, S. Zorita, *Sci. Total Environ.* 618 (2018) 551–560. <https://doi.org/10.1016/j.scitotenv.2017.11.003>.
- [16] I. Plazl, S. Leskovsek, T. Koloini, *Chem. Eng J.* 59 (1995) 253–257. [https://doi.org/10.1016/0923-0467\(94\)02953-9](https://doi.org/10.1016/0923-0467(94)02953-9).
- [17] J.B. Joshi, N.K. Nere, C.V. Rane, B.N. Murthy, C.S. Mathpati, A.W. Patwardhan, V.V. Ranade, *Can. J. Chem. Eng.* 89 (2011) 754–816. <https://doi.org/10.1002/cjce.20446>.
- [18] H. Patil, A.K. Patel, H.J. Pant, A.V. Vinod, *Hydraul. Eng.* 27 (2021) 200–209. <https://doi.org/10.1080/09715010.2018.1535921>.
- [19] F. Chen, W. Zhong, D. Wan, *Ocean. Eng.* 257 (2022) 1–13. <https://doi.org/10.1016/j.oceaneng.2022.111525>.
- [20] R. Steijl, G. Barakos, *Int. J. Numer. Methods Fluids* 58 (2008) 527–549. <https://doi.org/10.1002/flid.1757>.
- [21] J. Mcnaughton, I. Afgan, D.D. Apsley, *Int. J. Numer. Methods Fluids* 74 (2013) 250–269. <https://doi.org/10.1002/flid.3849>.
- [22] G. Desquesnes, M. Terracol, E. Manoha, P. Sagaut, *J. Comput. Phys.* 220 (2006) 355–382. <https://doi.org/10.1016/j.jcp.2006.05.019>.
- [23] H. Orihara, H. Miyata, *J. Mar. Sci.* 8 (2003) 47–60. <https://doi.org/10.1007/s00773-003-0163-5>.
- [24] Y. Guo, C.Y. Wu, C. Thornton, *AIChE J.* 59 (2013) 1059–1087. <https://doi.org/10.1002/aic.13900>.
- [25] P. Zhao, J. Xu, X. Liu, W. Ge, J. Wang, *Phys. Fluids* 32 (2020) 1–12. <https://doi.org/10.1063/5.0023423>.
- [26] S.H. Saraei, B. Peters, *Powder Technol.* 426 (2023) 118–125. <https://doi.org/10.1016/j.powtec.2023.118603>.
- [27] J. Wang, H. Liu, D. Xu, Z. Chen, K. Ma, *Build. Sci.* 160 (2019) 106–122. <https://doi.org/10.1016/j.buildenv.2019.106208>.

- [28] R. Mitkov, M. Pantusheva, V. Naserentin, P. Hristov, A. Logg, IFAC Proc. Ser. 55 (2022) 179–184.
<https://doi.org/10.1016/j.ifacol.2022.08.069>.

JUNHEE HAN¹
HYOJUNG KIM²
DOHYUNG LEE³

¹Department of Mechanical
engineering, Hanyang University,
Seoul, Korea

²Ackerton Partners, 41,
Cheonggyecheon-ro, Jongno-gu,
Seoul, Korea

³Department of Mechanical
Engineering, Hanyang
University, Ansan, Gyeonggi-do,
Korea

NAUČNI RAD

SUZBIJANJE PRE-HIDROLIZE U PROIZVODNJI TiO₂: OPTIMIZACIJA SISTEMA ZA INDIREKTNO ZAGREVANJE HIDROLIZATA

Na veličinu čestica TiO₂ kritično utiče vođenje procesa hidrolize. Neuspeh da se postigne ujednačena veličina čestica tokom hidrolize može imati značajne reperkusije na naknadne procese, kao što su postupci pranja, redukcije i beljenja, što na kraju dovodi do proizvodnje neupotrebljivih finalnih proizvoda. Primarni cilj ovog rada je suzbijanje pre-hidrolize, koja je faktor koji otežava formiranje uniformnih čestica tokom postupka hidrolize. Da bi prevazišli ovaj problem, istraživači su dizajnirali sistem indirektnog grejanja kako bi ublažili fenomen pre-hidrolize. Za projektovanje sistema indirektnog grejanja urađene su višefazne CFD simulacije. Predloženi optimizovani dizajn je zatim implementiran i testiran na stvarnom procesu. Uspeh procesnog testa je procenjen kroz testove vrednosti taloženja sprovedenih na hidrolizovanom rastvoru, a ujednačenost veličine čestica je analizirana korišćenjem slika transmisione elektronske mikroskopije, skenirajućeg elektronskog mikroskopa i Microtrac-a. Rezultati ovog rada pokazuju efikasnu primenu razvijene višefazne CFD simulacije u poboljšanju procesa hidrolize za proizvodnju čestica anataz titanijum dioksida. Ova uspešna integracija pokazuje primenu tehnika mašinstva u oblasti hemijskog inženjerstva.

Ključne reči: multifazni, konjugatna CFD simulacija; precipitacija; raspodela veličine čestica; proizvodnja TiO₂; hidroliza indirektnog zagrevanja.

DARIO BALABAN^{1,2}
JELENA LUBURA¹
PREDRAG KOJIĆ¹

¹University of Novi Sad,
Faculty of Technology Novi Sad,
Novi Sad, Serbia

²University of East Sarajevo,
Faculty of Technology Zvornik,
Zvornik, Republic of Srpska,
Bosnia and Herzegovina

SCIENTIFIC PAPER

UDC 662:544.4:004

INTEGRATED NEURAL NETWORK AND ASPEN PLUS MODEL FOR ENTRAINED FLOW GASIFICATION KINETICS INVESTIGATION

Article Highlights

- Sensitivity analysis of gasification kinetics of different feedstocks was performed in Aspen Plus
- Process parameters and feedstock impact on efficiency and syngas composition are analyzed
- Obtained results are used for ANN development and modeling with high accuracy
- Process parameters optimization studies regarding syngas content are performed

Abstract

Entrained flow gasification is a well-established technology, however, the main obstacle in process design is the complex gasification mechanism, since numerous phenomena at extreme process conditions take place simultaneously. This study is focused on integrated thermodynamic and artificial neural network approach (ANN) for entrained flow gasification kinetics investigation. Data on 102 feedstock materials composition was used in the AspenPlus gasification simulation, where sensitivity analysis was performed for different equivalence ratios (0.1–0.7) and gasification temperature (1200–1500°C) values. For analyzed materials, an optimal equivalence ratio range exists (usually 0.3–0.4), maximizing gasification efficiency. The obtained results were used in ANN development for each output variable (syngas composition, efficiency, heating value, and carbon conversion). Matlab algorithm was used for the determination of the optimal number of neurons (1–20 range) in each ANN. High R^2 values (>0.99) for all models suggested good agreement between simulated and predicted values. Genetic algorithm-based optimization studies for maximization of hydrogen content and cold gas efficiency result in mean ER values of 0.35 and 0.41, respectively, at a temperature of 1200 °C. Yoon interpretation method was used for quantifying the relative impacts of each input variable on syngas content and gasification efficiency. The proposed approach represents a powerful tool that can facilitate the investigation of the entrained flow gasification and process design.

Keywords: syngas; optimization; simulation; machine learning.

Global energy production, despite an increase in renewable energy sources consumption, is still

dominated by fossil fuels. Approximately one-third of global electricity production in 2022 came from renewable energy sources, while their share in total energy consumption is even lower, approaching 20% [1,2]. Taking into account the non-renewable nature of fossil fuels and intensive greenhouse gas and pollutant emissions, the energy industry is expected to shift towards cleaner energy sources (solar, wind, hydro, geothermal, biomass, etc.) [3], which is recognized and controlled by global policies [4,5]. Thus, a serious effort is made to develop new and improve the existing energy conversion technologies.

Correspondence: D. Balaban, University of Novi Sad, Faculty of Technology Novi Sad, Bulevar cara Lazara 1, 21000 Novi Sad, Serbia.

E-mail: dario.balaban@uns.ac.rs

Paper received: 30 April, 2024

Paper revised: 27 August, 2024

Paper accepted: 18 September, 2024

<https://doi.org/10.2298/CICEQ240430032B>

Thermochemical conversion technologies consist of the conversion of carbonaceous feedstocks into liquid, solid, or gaseous products for further production of electricity, heat, chemicals, or fuels. Among the conventional thermochemical conversion technologies (combustion, gasification, and pyrolysis) [6], gasification offers benefits in terms of high conversion efficiency [7], achievable carbon capture and cleanup of produced gas (syngas) [8], as well as polygenerative potential due to specific syngas composition [9]. The process consists of partial oxidation of carbon in the fuel in the presence of a gasifying agent, such as oxygen, air, air-oxygen mixture, steam, steam-oxygen mixture, or carbon dioxide. Produced syngas consist mainly of carbon monoxide, hydrogen, methane, carbon dioxide, and water. The solid residue consists of ash and an unconverted organic fraction of the fuel [10,11]. Overall reacting system is endothermic, where necessary energy can be provided by partial oxidation (auto-thermal gasification) or by external supply of energy (allo-thermal gasification). Considering the auto-thermal system, gasification can be seen as a sequence of three stages: drying, decomposition (devolatilization), and gasification. Overall process output depends on several factors, including operating conditions (temperature and pressure), amount and type of gasifying agent, feedstock composition, and gasification technology [11,12].

Several gasification technologies have been developed in recent years, which differ in operating conditions, feedstock material state, capacity, efficiency, and scale-up potential. Within the currently available gasification technologies, such as fixed bed and fluidized bed, entrained flow gasifiers constitute an interesting option owing to their commercial large-scale availability (technological readiness index of around 7–8), lower emissions, and their high efficiency for the production of syngas [13,14]. Complex construction and operation, problems with construction materials at high temperatures, as well as fuel specificity in terms of particle size, are compensated by high conversion efficiency, high capacity, good gas-solid contact and mixing, moderate heating value syngas, and great scale-up potential. Typical entrained flow gasification (EFG) temperature is above ash melting point, typically in the range of 1200–1500 °C, while gasification pressure is usually above 25 bar [13,15,16].

To develop and design gasification processes, a detailed investigation of process kinetics must be done, which helps determine the impact of operating conditions and feedstock material composition on outlet parameters, i.e., carbon conversion, syngas yield, and syngas composition. Thus, several different gasification models have been developed, which can be divided into kinetic rate models, thermodynamic

equilibrium models, and neural network models [15]. Kinetic models provide essential information on kinetic mechanisms to describe the conversion during biomass gasification. Several studies that include kinetic models have been made, taking into account gasification reactions, heat and mass transfer, and fluid dynamics in EFG [17–24]. Thermodynamic equilibrium models are independent of gasifier design and may be more suitable for process studies on the influence of the most important process parameters. Additionally, this model requires fewer details of the system in hand. Thus, stoichiometric and non-stoichiometric equilibrium models have extensively been used for gasification purposes [25–29], especially in the domain of EFG, since the system approaches thermodynamic equilibrium at higher temperatures [15,30]. Furthermore, this approach is often implemented in Aspen Plus simulation software, which has become a standard procedure for the simulation and investigation of the gasification process. The software enables equilibrium calculations through Gibbs free energy minimization [30]. Artificial neural networks (ANN) have recently been successfully used in various areas of chemical engineering research. The concept of ANN allows for black-box modeling of large amounts of data, which can be useful in phenomenologically complex processes, such as EFG and gasification in general. Therefore, several types of research using ANN have been conducted to evaluate the performance of various gasification systems [31], optimize a given gasification process for hydrogen production [32], model biomass gasification in fluidized bed gasifiers [33] and fixed bed downdraft gasifiers [34], predict biomass gasification process parameters [35] and develop a comprehensive gasification model, taking into account wide range of inlet and outlet parameters [36]. Also, some studies have developed an integrated thermodynamic equilibrium and ANN approach, which uses equilibrium calculation results as ANN input data, while a single output variable is considered, mainly syngas heating value [37] and net energy output [38].

By using simulation software like Aspen Plus, a thermodynamic equilibrium approach can be applied for the gasification of different feedstock materials at different operating conditions. Thus, obtained data on syngas composition can be used for the development of ANN, which will take into account feedstock composition, gasifying agent type, and flowrate, as well as operating conditions, and provide outputs in the form of syngas composition, gasification efficiency, etc. This approach can be beneficial on multiple levels, since only obtained ANN models are necessary for the evaluation of gasification performance, thus providing a tool for engineers for preliminary assessment of potential plant efficiency, gasification operation

feasibility, and necessary operating conditions. Also, gasification kinetics for a given material can be assessed without the use of a process simulator, while a comparative analysis of the behavior of different feedstock materials can be performed.

It is worth mentioning that there is ongoing research and development in the field of gasification, and new and innovative technologies are emerging that could potentially surpass EFG in terms of efficiency and cost-effectiveness [39–41]. Nonetheless, EFG remains one of the most promising and widely used gasification technologies at present. Therefore, the goal of this research is to investigate in detail the kinetics of the EFG process via an integrated ANN and thermodynamic equilibrium approach. To obtain representative data on EFG, numerous different feedstock materials have been investigated, whose composition is taken from the literature and used as an input in Aspen Plus gasification simulation. Typical oxyfuel gasification process flowsheet configuration was used, while sensitivity analysis was performed for all samples, with equivalence ratio and gasification temperature as parameters to be varied. Obtained results are used as input data for ANN development using a Matlab algorithm for network topology optimization. Obtained models for the prediction of output variables (syngas composition, cold gas efficiency, carbon conversion, and syngas LHV) are further used for developing the objective function for optimization via the genetic algorithm method. The objective function uses equivalence ratio and temperature as decision variables and parameters of interest as target variables, thus allowing for quick determination of optimal process parameters for a given feedstock material.

MATERIALS AND METHODS

Feedstock material data

To develop a comprehensive gasification model, a wide range of input parameters is necessary. Since gasification is suitable for a relatively broad spectrum of raw materials, data on various feedstock material types' composition is obtained from the literature. The general idea is to obtain data on proximate and ultimate analysis for materials of different origins and heating values, providing the necessary range of individual component composition. Data on proximate and ultimate analysis is obtained for 40 municipal solid waste (MSW) and refuse-derived fuel (RDF) samples, 39 biomass samples, 10 coal samples, and 13 biomass briquettes samples. Complete input data is given in Supplementary material, Table S1. Since further calculations require the data on materials' lower heating value (*LHV*), for instances where only a higher

heating value (*HHV*) is given, necessary conversion is made according to Eq. (1) [42]:

$$LHV = HHV - (9 \cdot H + Moisture) \cdot 2.44 \left[\frac{MJ}{kg} \right] \quad (1)$$

where *H* and *Moisture* stand for hydrogen and moisture content, respectively

Process simulation and sensitivity analysis

Gasification process simulation is performed in Aspen Plus software. Raw material composition data is used in the definition of nonconventional components, with HCOALGEN and DCOALIGT models being used for enthalpy and density calculations. Peng-Robinson equation of state was used as a thermodynamic model. Defined components consist of nonconventional components (raw material and ash), decomposition products (C, H₂, N₂, H₂O, S, Cl₂, O₂), and possible syngas components (CH₄, CO, CO₂, NO, NH₃, HCl, H₂S, C₂H₆). A typical gasification process flowsheet (Figure 1) is developed, where feedstock material (FEEDSTOCK) first enters the decomposition (DECOMP - R_{yield}) reactor, where drying and devolatilization processes take place at 500 °C and gasification pressure of 25 bar. Then, the mixture enters the gasification reactor (GASIFIER - RGibbs), along with pure oxygen (O₂-GASIF), which enters the reactor at 200 °C and 25 bar. In the gasifier, restricted chemical equilibrium calculations take place at the selected gasification temperature, while the heat required for decomposition (*Q*) is provided from this reactor. Obtained products are sent to a separator block (SEPARATOR), where unconverted carbon and ash are removed (SLAG), thus simulating the formation of slag in the gasifier.

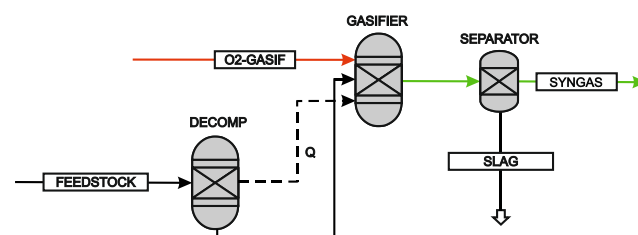


Figure 1. Aspen Plus gasification process flowsheet.

For the determination of the necessary oxygen flow rate for each simulation, equivalence ratio (ER) was used, while all calculations were performed in a Calculator block. The equivalence ratio for oxyfuel gasification is defined as:

$$ER = \frac{(O/F)}{(O/F)_{st}} \quad (2)$$

where O/F stands for the actual ratio of oxygen to fuel,

while $(O/F)_{st}$ stands for the stoichiometric ratio. Sensitivity analysis was performed for every raw material, with ER and gasification temperature being the parameters to be varied. Temperature was varied in the range of 1200 °C to 1500 °C, with 15 °C increments, while ER was varied in the range of 0.1 to 0.7, with 0.03 increments. A defined flowsheet configuration is set for the autothermal gasification regime; if the gasification reactor provides insufficient heat for decomposition (for example, when ER is too low, or when the material has a low heating value), the error is reported, and these results were not taken into consideration. Simulation results include the content of main syngas components (CO, H₂, CO₂, CH₄, and H₂O), while obtained data is used for the calculation of syngas LHV , carbon conversion, and cold gas efficiency (CGE). Carbon conversion and CGE are calculated from the following equations:

$$CONV = \frac{m_{c,in} - m_{c,out}}{m_{c,in}} \cdot 100(\%) \quad (3)$$

$$CGE = \frac{m_{syngas} \cdot LHV_{syngas}}{m_f \cdot LHV_f} \cdot 100(\%) \quad (4)$$

where $m_{c,in}$ and $m_{c,out}$ stand for carbon flow rate at gasifier inlet and outlet, m_{syngas} and m_f stand for syngas and feedstock mass flowrate, and LHV_{syngas} and LHV_f stand for syngas and feedstock LHV, respectively.

Artificial neural network modeling and optimization

Sensitivity analysis results are used as input data for the development of ANN for prediction of output parameters. MatLab's Neural Network Toolbox was used for the design of the neural network structure. A standard structure with one hidden layer was used, with a linear transfer function at the output layer and a tangent sigmoid function at the hidden layer. An algorithm was developed for the determination of the most suitable number of neurons in a hidden layer. The number of hidden neurons varied from 1 to 20, and the training process of each network was run 10 times with random initial values of weights and biases. The best topology was determined according to the coefficient of determination (R^2), Mean squared error (MSE), and mean absolute percentage error ($MAPE$) values. Bayesian regularization backpropagation algorithm was used for network training, where 60% of the data was used as training data, 20% as validation data, and 20% as test data. Each network consists of multiple inputs (ultimate analysis of feedstock material, moisture content, ER, and temperature) and singular output (syngas content of a selected component (CH₄, CO₂, CO, H₂, H₂O), syngas LHV , CGE or carbon conversion). Hence, 8 independent ANNs were

developed.

Obtained functions are later used for process optimization for a given condition using a genetic algorithm function. As a result of the optimization procedure for a given feedstock material composition, the algorithm returns values for ER and gasification temperature. Therefore, the algorithm can be used for various problems, for example, in the maximization or minimization of specific component content in syngas, in adjusting of components ratio in syngas, in maximization of CGE , syngas heating value, or carbon conversion.

RESULTS AND DISCUSSION

Characteristics of investigated feedstock materials

As stated previously, materials of different origins were used in this study, to cover a wide range of elemental components compositions. It should be mentioned that some of the materials were completely unsuitable for the gasification process since the simulation reported errors for every combination of ER and temperature in sensitivity analysis. This is mainly due to high moisture content and low LHV value, which is typical for some MSW and biomass samples. The general characteristics of feedstock material which were suitable for gasification simulation are shown in Figure 2. It should be noted that the box plot for the chlorine content was not displayed due to its low content in all materials. Also, outliers in LHV , carbon, and sulfur content data correspond to coal samples used in this study.

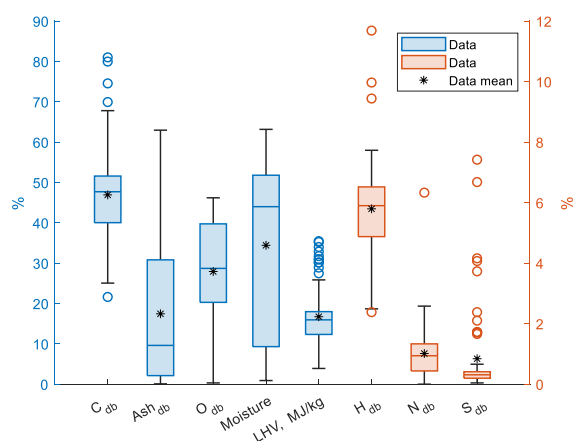


Figure 2. Box-plot representation of feedstock materials composition and LHV taken from literature; db stands for dry-basis composition.

Impact of operating conditions on entrained flow gasification

To analyze and discuss the relative impact of main operating conditions, ER, and temperature on the

oxyfuel EFG process, the results of a sensitivity study on a randomly selected feedstock material will be displayed. Surface plots for selected output parameters, mainly syngas composition and overall gasification parameters, are displayed in Figures 3 and

4. According to plots displayed in Figure 3, a nonlinear correlation between syngas composition and operating conditions can be observed. A crucial observation is that there is a distinctive range of operating parameter values for which H₂ and CO content are at maximum.

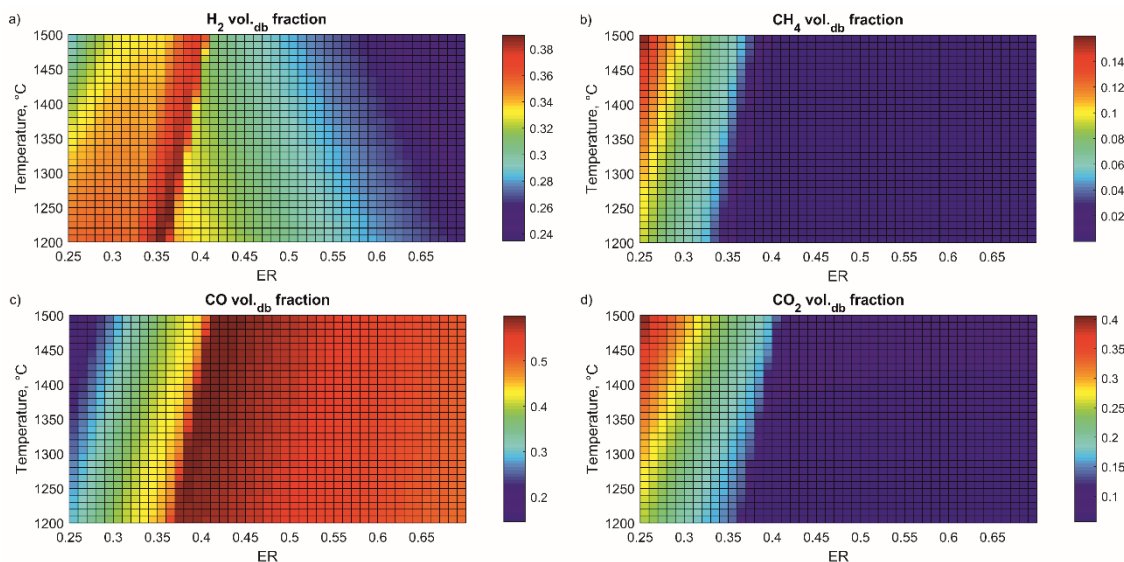


Figure 3. Dry-basis: (a) H₂ content, (b) CH₄ content, (c) CO content, (d) CO₂ content in syngas as a function of ER and gasification temperature.

Hydrogen content reaches maximum values in the ER range of 0.33–0.4 (Figure 3a), while lower temperatures favor hydrogen content increase. Maximum CO content is obtained in a similar ER range (Figure 3c), while a further increase of ER value slightly decreases CO content, with similar conclusions about temperature influence to be made. It can be assumed that the dominant reactions in the selected operating conditions range are partial oxidation and water-gas reactions. Methane content is significant at lower ER values (Figure 3b), where methanation and hydrogasification reactions are dominant. Methane and CO₂ content decrease with an increase of ER (Figures 3b and 3d), with a sharp decrease being in line with the area of maximum H₂/CO values.

Overall gasification efficiency is strongly dependent on the content of main syngas components, H₂ and CO, due to their high heating values. Cold gas efficiency increases with an increase in ER, with maximum CGE values being in the ER range of 0.33–0.4 and lower temperature area (Figure 4b). Complete carbon conversion is obtained after the 0.35 ER threshold, for all temperatures (Figure 4c). In general, higher gasification temperatures lower the conversion and CGE, due to the increase of necessary mixture sensible heat. It could be noted that the optimal operating conditions ensure complete carbon conversion with minimal consumption of gasifying agents. Syngas LHV follows a similar pattern, with the main difference being a significant decrease in high ER

area (Figure 4a). However, higher ER results in higher overall gas yield, which explains the slight decrease in CGE values (Eq. (4) and Figure 4b).

Gasification kinetics in general is complex since the process takes place via a series of elementary reactions. However, it is stated in the literature that few global reactions, including only key components and interproducts, can be used for modeling purposes. Those reactions are given in Table 1 [43].

Table 1. Main gasification reactions.

Stoichiometry	Name
Char combustion	
$C + 1/2O_2 \rightarrow CO$	Partial combustion
$C + O_2 \rightarrow CO_2$	Complete combustion
Char gasification	
$C + CO_2 \rightarrow 2CO$	Boudouard reaction
$C + H_2O \rightarrow CO + H_2$	Steam gasification
$C + 2H_2 \rightarrow CH_4$	H ₂ gasification
Homogenous	
$CO + 1/2O_2 \rightarrow CO_2$	CO oxidation
$H_2 + 1/2O_2 \rightarrow H_2O$	H ₂ oxidation
$CH_4 + 2O_2 \rightarrow CO_2 + 2H_2O$	CH ₄ oxidation
$CO + H_2O \rightarrow CO_2 + H_2$	Water-gas shift

Simulation results indicate that high hydrogen content corresponds to low water content in syngas, which can be attributed to the water-gas shift reaction, as well as the steam gasification reaction, where carbon is gasified with water vapor. At the area of complete carbon conversion, carbon gasification and oxidation no longer take place, which also causes hydrogen not to form via steam gasification reaction.

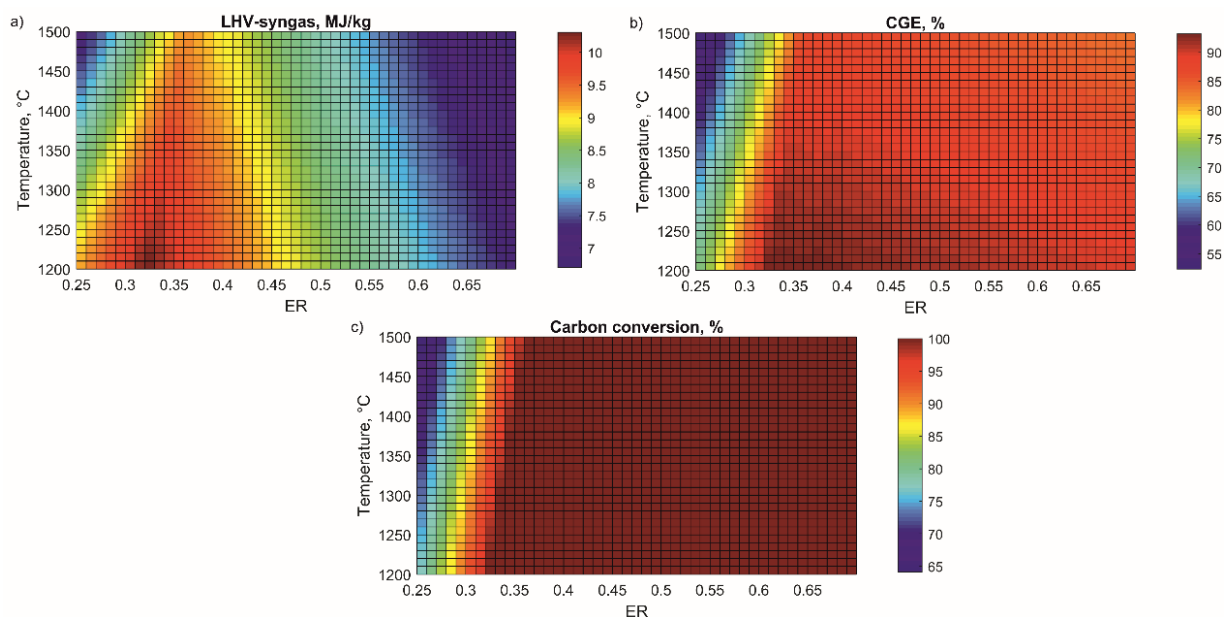


Figure 4. Overall gasification parameters, (a) syngas LHV, (b) CGE, (c) carbon conversion as a function of ER and gasification temperature.

Boudouard reaction is one of the most important reactions in the entire gasification mechanism, where carbon reacts with CO_2 while forming CO . This explains the decrease of CO content in the area of higher ER. At complete carbon conversion, the system stabilizes and no significant composition changes take place. Only homogenous reactions take place, primarily water-gas shift, while temperature and approximately equilibrium composition prohibit further reaction advancement. Also, it is important to highlight that methane and other hydrocarbons decompose at higher temperatures [13], which is why the obtained methane content is low.

Artificial neural networks

One neural network was developed for each output variable via the algorithm described in Materials and Methods. It should be noted that after initial runs, the number of input parameters decreases since chlorine and nitrogen contents in feedstock materials are very low and their impact on output variables should be negligible (due to the small quantity and inert nature of their gasification products). Likewise, ash is inert in the gasification process, thus, its impact is also neglected, resulting in 7 input parameters (carbon, hydrogen, oxygen, sulfur, and moisture contents, and ER and gasification temperature) for each output parameter. ANN performance and topology are shown in Table 2, while parity plots of some predicted and simulated values are shown in Figure 5. The remaining parity plots are given in Supplementary material, Figure S1.

The number of hidden neurons increases the prediction accuracy since the optimal number of neurons was close to 20, while coefficients of

determination values were above 0.99 for all instances. The impact of hidden neurons' number on the coefficient of determination for each neural network is given in Supplementary material, Figures S2 and S3. High accuracy is also confirmed by low MSE and MAPE values. It should be noted that simulated values of certain values are close to zero for a wide range of operating parameters, thus resulting in a relatively high MAPE value, even though overall prediction accuracy is high.

Table 2. Artificial neural network structure and prediction accuracy.

Each output neuron	Hidden neurons	R^2	MAPE %	MSE
H_2	19	0.9938	4.3858	$4.7553 \cdot 10^{-5}$
CO	19	0.9988	13.6318	$4.4521 \cdot 10^{-5}$
CH_4	19	0.9987	60.3509	$2.74339 \cdot 10^{-6}$
CO_2	20	0.9968	16.8125	$2.9776 \cdot 10^{-5}$
H_2O	20	0.9984	7.0330	$6.6187 \cdot 10^{-5}$
Syngas LHV	20	0.9997	0.4967	0.0035
CGE	20	0.9989	1.3559	0.6355
Carbon conversion	20	0.9994	0.2970	0.1951

To quantify the impact of input variables on syngas composition and overall gasification parameters, Yoon's interpretation method was used [44]. Obtained results are displayed in Table 3. It can be noted that the equivalence ratio has a higher general impact on syngas composition and overall gasification efficiency than temperature, while carbon and moisture content impact the syngas composition the most. Results on the relative importance of ER and gasification temperature are in line with sensitivity analysis results displayed previously.

Since developed neural network models show

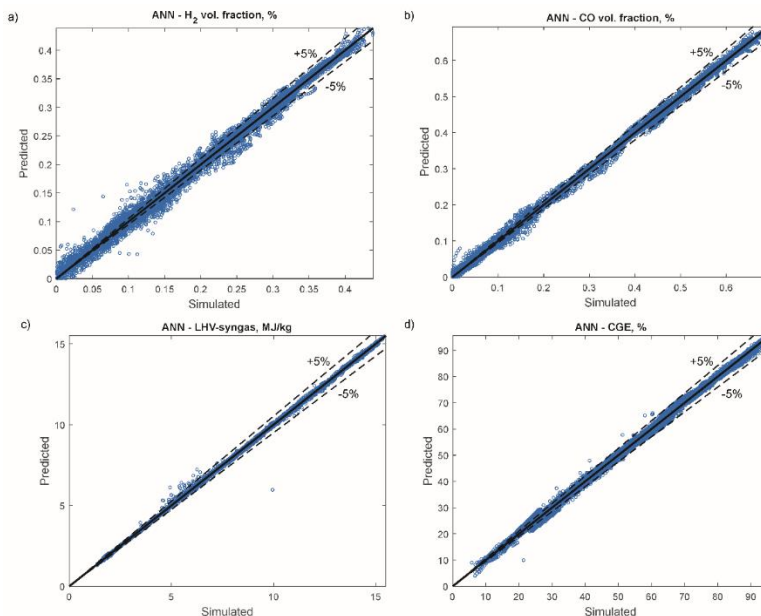


Figure 5. Simulated and predicted data on (a) H_2 content, (b) CO content, (c) syngas LHV, and (d) CGE, according to the developed ANN model.

Table 3. The relative impact of input parameters on output parameters in the EFG process.

	ER	T, °C	C	H	O	Moisture
H_2	38.0 ± 12.5	-4.3 ± 0.5	13.6 ± 2.8	1.6 ± 6.4	6.3 ± 9.1	-17.4 ± 4.5
CO	38.7 ± 7.2	-3.8 ± 0.6	11.5 ± 4.2	3.0 ± 7.8	4.0 ± 3.8	-15.3 ± 8.5
CH_4	-49.9 ± 6.2	4.3 ± 0.5	-12.4 ± 1.6	5.7 ± 2.7	-1.6 ± 2.5	10.1 ± 5.6
CO_2	-21.2 ± 6.7	3.8 ± 1.0	-7.5 ± 7.8	-9.7 ± 5.0	2.1 ± 7.2	12.0 ± 8.6
H_2O	-36.1 ± 8.4	4.1 ± 0.6	-16.3 ± 4.3	-2.8 ± 4.9	-2.0 ± 4.4	23.3 ± 3.1
Syngas LHV, MJ/kg	7.7 ± 11.3	-3.6 ± 0.9	4.5 ± 4.4	20.0 ± 5.0	-2.7 ± 4.9	-14.3 ± 6.6
CGE, %	4.2 ± 5.3	-0.6 ± 0.8	9.4 ± 5.5	-9.7 ± 17.3	-3.9 ± 11.8	-7.1 ± 6.6
Carbon conversion, %	39.7 ± 7.4	-1.7 ± 0.6	-1.3 ± 2.9	7.5 ± 4.1	9.5 ± 3.7	9.3 ± 5.3

good agreement between simulated and predicted data, they could be further used for optimization purposes. Two optimization problems were tested; obtaining the maximum hydrogen fraction in syngas and obtaining of maximum CGE for a given feedstock material. A genetic algorithm was used for optimization

on each feedstock material, with ER and gasification temperature as output parameters. Parity plots on simulated (based on sensitivity analysis results) and predicted (optimization) hydrogen fraction and CGE are shown in Figure 6.

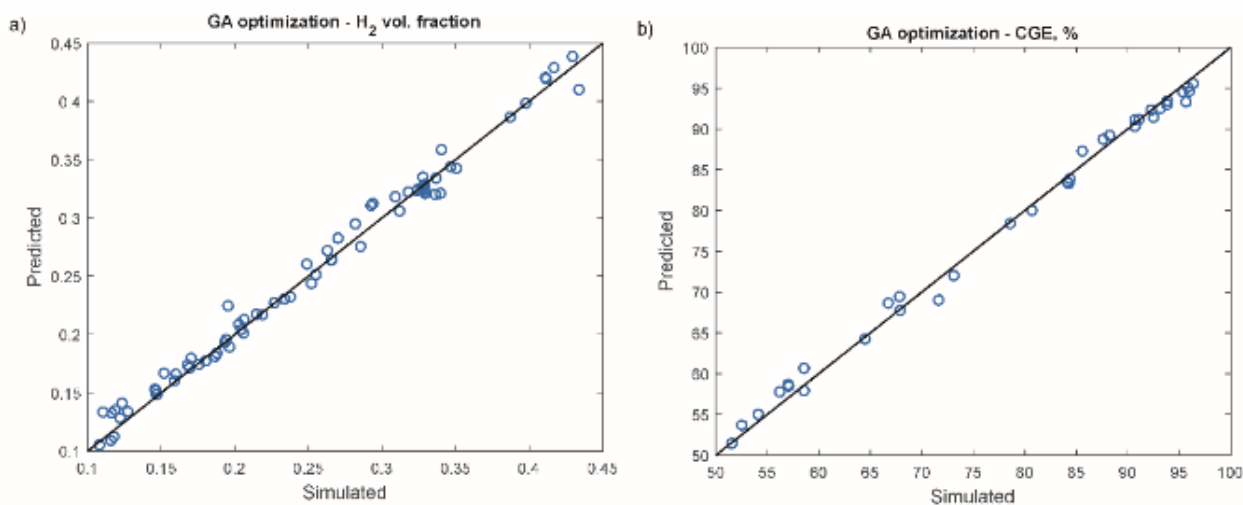


Figure 6. Predicted and simulated; (a) H_2 content and (b) CGE according to optimization procedure.

The obtained optimization results are in accordance with sensitivity analysis results. It should be noted that ER and temperature are in this case continuous variables, contrary to sensitivity analysis, which could lead to slight deviation of results. Temperatures corresponding to optimal operating conditions are close to the minimal gasification temperature of 1200 °C, while mean ER values are 0.35 for hydrogen optimization and 0.41 for CGE optimization.

In general, this approach contributes to a better understanding of EFG process kinetics, while developed ANN models can be used for quick prediction of gasification output parameters for a given feedstock. Obtained syngas composition can be further used to facilitate gasification-based process simulation since complex three-phase calculations are bypassed. Also, models can be used for process optimization i.e. obtaining the optimal operating conditions for a specified goal.

CONCLUSION

An integrated ANN and Aspen Plus gasification model was used for the investigation of entrained flow gasification kinetics. Various feedstock materials, mainly waste, RDF, coal, and biomass were used to obtain a wide range of input material elemental compositions. For each feedstock material, sensitivity analysis on EFG in Aspen Plus was performed, for different equivalence ratios and temperatures, and obtained results were used in ANN development. Single layer ANNs with an adjustable number of neurons were developed for every output variable (syngas components fractions, cold gas efficiency, syngas lower heating value, and carbon conversion), with high prediction accuracy ($R^2 > 0.99$). All models consist of a high number of hidden neurons (19–20). Also, the general impact of ER and temperature, as well as feedstock material composition on output parameters was determined and discussed. The highest gasification efficiencies are obtained at lower temperatures, just above ash melting temperatures, and in a narrow range of ER, typically 0.35–0.45, depending on feedstock material composition. In this ER range, the highest H₂ content and moderate CO content are obtained, resulting in the highest syngas heating value. Further increase of ER does not have a significant effect on syngas composition. Obtained models can be used for optimization problems, where two desired goals were successfully tested; determination of optimal combination of ER and temperature for maximization of syngas hydrogen content and cold gas efficiency. For investigated materials, mean optimal parameters are temperature of

1200 °C and ER of 0.41 and 0.35 for cold gas efficiency and hydrogen content, respectively. This combined ANN and simulation approach allows for quick and accurate prediction of EFG efficiency and syngas composition, thus providing essential information for the design and development of gasification processes.

ACKNOWLEDGEMENTS

The authors would like to thank the Ministry of Education, Science and Technological Development of the Republic of Serbia, Project No. 451-03-65/2024-03/200134.

REFERENCES

- [1] H. Ritchie, P. Rosado, M. Roser, Energy Production and Consumption, <https://ourworldindata.org/energy-production-consumption>, [accessed 7 May 2024].
- [2] IEA, World Energy Outlook 2022, <https://www.iea.org/reports/world-energy-outlook-2022>, [accessed 7 May 2024].
- [3] M.N. Dudin, E.E. Frolova, O.V. Protopopova, O. Mamedov, S.V. Odintsov, 6 (2019) 1704. [https://doi.org/10.9770/jesi.2019.6.4\(11\)](https://doi.org/10.9770/jesi.2019.6.4(11)).
- [4] C.-F. Schleussner, J. Rogelj, M. Schaeffer, T. Lissner, R. Licker, E.M. Fischer, R. Knutti, A. Levermann, K. Frieler, W. Hare, Nat Clim Chang 6 (2016) 827–835. <https://doi.org/10.1038/nclimate3096>.
- [5] L. Mundaca, L. Neij, A. Markandya, P. Hennicke, J. Yan, Appl Energy 179 (2016) 1283–1292. <https://doi.org/10.1016/j.apenergy.2016.08.086>.
- [6] H.B. Goyal, D. Seal, R.C. Saxena, 12 (2008) 504–517. <https://doi.org/10.1016/j.rser.2006.07.014>.
- [7] V. Kirubakaran, V. Sivaramakrishnan, R. Nalini, T. Sekar, M. Premalatha, P. Subramanian, 13 (2009) 179–186. <https://doi.org/10.1016/j.rser.2007.07.001>.
- [8] V. Tola, A. Pettinau, Appl Energy 113 (2014) 1461–1474. <https://doi.org/10.1016/j.apenergy.2013.09.007>.
- [9] J. Parraga, K.R. Khalilpour, A. Vassallo, 92 (2018) 219–234. <https://doi.org/10.1016/j.rser.2018.04.055>.
- [10] R. Rauch, J. Hrbek, H. Hofbauer, Wiley Interdiscip Rev Energy Environ 3 (2014) 343–362. <https://doi.org/10.1002/9781118957844.ch7>.
- [11] A. Molino, S. Chianese, D. Musmarra, 25 (2016) 10–25. <https://doi.org/10.1016/j.jechem.2015.11.005>.
- [12] M. Lapuerta, J.J. Hernández, A. Pazo, J. López, 89 (2008) 828–837. <https://doi.org/10.1016/j.fuproc.2008.02.001>.
- [13] U. Arena, 32 (2012) 625–639. <https://doi.org/10.1016/j.wasman.2011.09.025>.
- [14] J.J. Hernández, G. Aranda-Almansa, A. Bula, 91 (2010) 681–692. <https://doi.org/10.1016/j.fuproc.2010.01.018>.
- [15] M. Puig-Arnabat, J.C. Bruno, A. Coronas, 14 (2010) 2841–2851. <https://doi.org/10.1016/j.rser.2010.07.030>.
- [16] E. Henrich, F. Weirich, Environ Eng Sci 21 (2004) 53–64. <https://doi.org/10.1089/109287504322746758>.
- [17] T. Xu, Y. Wu, S. Bhattacharya, Int J Min Sci Technol 31

- (2021) 473–481.
<https://doi.org/10.1016/j.ijmst.2021.03.001>.
- [18] F. Qian, X. Kong, H. Cheng, W. Du, W. Zhong, *Ind Eng Chem Res* 52 (2013) 1819–1828.
<https://doi.org/10.1021/ie301630x>.
- [19] M. Vascellari, R. Arora, C. Hasse, 118 (2014) 369–384.
<https://doi.org/10.1016/j.fuel.2013.11.004>.
- [20] G.-S. Liu, H.R. Rezaei, J.A. Lucas, D.J. Harris, T.F. Wall, 79 (2000) 1767–1779. [https://doi.org/10.1016/S0016-2361\(00\)00037-5](https://doi.org/10.1016/S0016-2361(00)00037-5).
- [21] A. Tremel, H. Spliethoff, 107 (2013) 170–182.
<https://doi.org/10.1016/j.fuel.2013.01.062>.
- [22] M. Vascellari, D.G. Roberts, D.J. Harris, C. Hasse, 152 (2015) 58–73. <https://doi.org/10.1016/j.fuel.2015.01.038>.
- [23] I. Adeyemi, I. Janajreh, *Renew Energy* 82 (2015) 77–84.
<https://doi.org/10.1016/j.renene.2014.10.073>.
- [24] M.A. Kibria, P. Sripada, S. Bhattacharya, 196 (2020) 117073. <https://doi.org/10.1016/j.energy.2020.117073>.
- [25] M. Al-Zareer, I. Dincer, M.A. Rosen, 115 (2016) 1–18.
<https://doi.org/10.1016/j.cherd.2016.09.009>.
- [26] M. Pérez-Fortes, A.D. Bojarski, E. Velo, J.M. Nogués, L. Puigjaner, 34 (2009) 1721–1732.
<https://doi.org/10.1016/j.energy.2009.05.012>.
- [27] Y. Lu, Z. Li, M. Zhang, C. Huang, Z. Chen, *Energy Convers Manag* 245 (2021) 114627.
<https://doi.org/10.1016/j.enconman.2021.114627>.
- [28] Z. Dai, X. Gong, X. Guo, H. Liu, F. Wang, Z. Yu, 87 (2008) 2304–2313. <https://doi.org/10.1016/j.fuel.2007.12.005>.
- [29] D. Barba, M. Prisciandaro, A. Salladini, G.M. Di Celso, 90 (2011) 1402–1407.
<https://doi.org/10.1016/j.fuel.2010.12.022>.
- [30] Ö.Ç. Mutlu, T. Zeng, *Chem Eng Technol* 43 (2020) 1674–1689. <https://doi.org/10.1002/ceat.202000068>.
- [31] M. Ozonoh, B.O. Oboirien, A. Higginson, M.O. Daramola, *Renew Energy* 145 (2020) 2253–2270.
<https://doi.org/10.1016/j.renene.2019.07.136>.
- [32] H.O. Kargbo, J. Zhang, A.N. Phan, *Appl Energy* 302 (2021) 117567.
<https://doi.org/10.1016/j.apenergy.2021.117567>.
- [33] M. Puig-Arnavat, J.A. Hernández, J.C. Bruno, A. Coronas, *Biomass Bioenergy* 49 (2013) 279–289.
<https://doi.org/10.1016/j.biombioe.2012.12.012>.
- [34] D. Baruah, D.C. Baruah, M.K. Hazarika, *Biomass Bioenergy* 98 (2017) 264–271.
<https://doi.org/10.1016/j.biombioe.2017.01.029>.
- [35] R. Mikulandrić, D. Lončar, D. Böhning, R. Böhme, M. Beckmann, *Energy Convers Manag* 87 (2014) 1210–1223. <https://doi.org/10.1016/j.enconman.2014.03.036>.
- [36] S. Ascher, W. Sloan, I. Watson, S. You, *Appl Energy* 320 (2022) 119289.
<https://doi.org/10.1016/j.apenergy.2022.119289>.
- [37] F. Kartal, U. Özveren, 209 (2020) 118457.
<https://doi.org/10.1016/j.energy.2020.118457>.
- [38] S. Safarian, S.M.E. Saryazdi, R. Unnthorsson, C. Richter, 213 (2020) 118800.
<https://doi.org/10.1016/j.energy.2020.118800>.
- [39] J. Chen, J. Liang, Z. Xu, E. Jiaqiang, *Energy Convers Manag* 226 (2020) 113497.
<https://doi.org/10.1016/j.enconman.2020.113497>.
- [40] H. Shahbeik, W. Peng, H.K.S. Panahi, M. Dehghani, G.J. Guillemain, A. Fallahi, H. Amiri, M. Rehan, D. Raikwar, H. Latine, 167 (2022) 112833.
<https://doi.org/10.1016/j.rser.2022.112833>.
- [41] M. Shahbaz, T. Al-Ansari, M. Inayat, S.A. Sulaiman, P. Parthasarathy, G. McKay, 134 (2020) 110382.
<https://doi.org/10.1016/j.rser.2020.110382>.
- [42] A. Ozyuguran, A. Akturk, S. Yaman, 214 (2018) 640–646.
<https://doi.org/10.1016/j.fuel.2017.10.082>.
- [43] A. Gómez-Barea, P. Ollero, B. Leckner, 103 (2013) 42–52. <https://doi.org/10.1016/j.fuel.2011.04.042>.
- [44] Y. Yoon, G. Swales Jr, T.M. Margavio, 44 (1993) 51–60.
<https://doi.org/10.1057/jors.1993.6>.

DARIO BALABAN^{1,2}
JELENA LUBURA¹
PREDRAG KOJIĆ¹

¹Univerzitet u Novom Sadu,
Tehnološki fakultet Novi Sad,
Novi Sad, Srbija

²Univerzitet u Istočnom
Sarajevu, Tehnološki fakultet
Zvornik, Zvornik, Republika
Srpska, Bosna i Hercegovina

INTEGRISANI MODEL ZASNOVAN NA NEURONSKIM MREŽAMA I ASPENPLUS SOFTVERU ZA ISPITIVANJE KINETIKE GASIFIKACIJE U ZAHVAĆENOM TOKU ČESTICA

Gasifikacija u zahvaćenom toku čestica predstavlja razvijenu tehnologiju, međutim, glavna prepreka u projektovanju procesa je složen mehanizam gasifikacije, s obzirom da se više fenomena na ekstremnim procesnim uslovima odvija istovremeno. Ova studija je fokusirana na integrisani pristup pomoću termodinamike i veštačkih neuronskih mreža (ANN) za ispitivanje kinetike gasifikacije u zahvaćenom toku čestica. Podaci o 102 sastava sirovina su korišteni za simulaciju gasifikacije u AspenPlus softveru, gde je analiza osetljivosti izvršena za različite ekvivalentne odnose (0.1–0.7) i gasifikacione temperature (1200–1500 °C). Za analizirane sirovine postoji optimalni opseg ekvivalentnog odnosa (obično 0.3–0.4), čime se maksimizuje efikasnost gasifikacije. Dobijeni rezultati su korišteni za razvoj ANN za svaku izlaznu promenljivu (sastav singasa, efikasnost, toplotna moć i konverzija ugljenika). Matlab algoritam je korišten za određivanje optimalnog broja neurona (u opsegu od 1–20) za svaku ANN. Visoka vrednost R^2 (>0.99) za sve modele ukazuje na dobro poklapanje između simuliranih i predviđenih vrednosti. Optimizacione studije bazirane na genetičkom algoritmu za maksimizaciju sadržaja vodonika i hladne efikasnosti gasa rezultuju srednjim ER vrednostima od 0.35 i 0.41, respektivno, na temperaturi od 1200 °C. Yoon-ova metoda interpretacije je korištena za kvantifikaciju relativnih uticaja svake ulazne promenljive na sadržaj singasa i efikasnost gasifikacije. Predloženi pristup predstavlja moćan alat koji može da ubrza istraživanje procesa gasifikacije u zahvaćenom toku čestica i projektovanje procesa.

Ključne reči: singas; optimizacija; simulacija; mašinsko učenje.

NAUČNI RAD